SPATIALLY AND TEMPORALLY RESOLVING RADIO-FREQUENCY CHANGES IN EFFECTIVE CELL MEMBRANE CAPACITANCE

by

Sameera Dharia

A dissertation submitted to the faculty of
The University of Utah
In partial fulfillment of the requirements for the degree of

Doctor of Philosophy

Department of Bioengineering

The University of Utah

May 2011

Copyright © Sameera Dharia 2011

All Rights Reserved

The University of Utah Graduate School

STATEMENT OF DISSERTATION APPROVAL

The dissertation of **Sameera Dharia**

has been approved by the following supervisory committee members:

Richard Rabbitt, Chair **01/11/2011**
Date Approved

John White, Member **01/11/2011**
Date Approved

Bruce Gale, Member **01/12/2011**
Date Approved

Michael Sanguinetti, Member **01/20/2011**
Date Approved

Vladimir Hlady, Member **01/12/2011**
Date Approved

and by **Patrick Tresco**, Chair of
the Department of **Bioengineering**

and by Charles A. Wight, Dean of The Graduate School.

ABSTRACT

Subcellularly resolved, excitable changes (i.e., those induced by electrical or chemical stimuli) in membrane capacitance, influenced by factors including integral-membrane protein activity, lipid densities and membrane-bound water content, may be used to elucidate nonconductive ion-channel conformational state changes, lipid-raft locations and drug–membrane binding processes. However, membrane capacitance has proven difficult to measure, partially because of bandwidth limitations associated with glass/quartz pipettes used during conventional electrophysiology. To address these challenges, techniques introduced in this thesis integrate the principles of extracellular radio frequency (RF) recording with conventional two-electrode voltage clamp (TEVC) to 1) spatially resolve effective membrane capacitance and 2) monitor excitable changes in effective membrane capacitance. Furthermore, this thesis also introduces a new multielectrode method to approximate electrode–electrolyte interfacial impedance, which might prove useful in electric impedance spectroscopic or electric impedance tomographic applications. Specific contributions include the following:

1) A method that simultaneously estimates double-layer and interelectrode (chamber) impedances, in the linear regime of electrode voltage–current sensitivity, during extracellular electrode-based measurements. This method estimates impedance parameters by applying a nonlinear least-squares regression to measurements between various groups or pairs of a three-electrode system

and, unlike previous double-layer approximation methods, can be done without the use of multiple calibration solutions or moveable electrode configurations.

2) A platform capable of visualizing the spatial distribution of membrane capacitance, using extracellular RF electrode recordings, around a single cell. The proof-of-concept for this technique is demonstrated with dielectric maps around polarized *Xenopus* oocyte membranes.
3) Development and characterization of a platform to enable RF impedance-based measurements around voltage-clamped *Shaker*B-IR-expressing *Xenopus* oocytes. Data indicated that the platform was most sensitive to effective changes in oocyte dielectric at 300 kHz and 500 kHz.
4) Temporal characterization of changes in voltage-sensitive RF membrane capacitance associated with *Shaker*B-IR activation (expressed in *Xenopus* oocytes) and *Shaker*B-IR–Cu^{2+} interactions.

Results indicate that extracellular RF-impedance-based measurements can temporally and spatially elucidate changes in excitable cell-membrane capacitance and could supplement conventional electrophysiological techniques to provide a broader understanding of cellular biophysics.

In memory of my mom

TABLE OF CONTENTS

ACKNOWLEDGEMENTS

First and foremost, I would like to thank my advisor, Richard Rabbitt, for his help and guidance over the past several years. The resources and time he has committed to my project have proved invaluable, and my discussions with him have provided numerous insights into all phases of my research.

I would also like to thank my committee members, Frederick Sachs, Michael Sanguinetti, Bruce Gale, Vladimir Hlady and John White, for their support and excellent mentorship. I would particularly like to thank Michael Sanguinetti for introducing me to new biological techniques, allowing me to use his laboratory facilities and providing technical expertise regarding ion-channel data interpretation.

My fellow laboratory members and colleagues have also been amazing resources during my time in graduate school. I worked more closely with Gregory Dittami than any other student in our laboratory, and he provided a great source of support and ideas throughout my years at Utah. I would also like to thank John Braithwaite for his help with Comsol simulations, Jennifer Abbruzzesse for her guidance in DNA transcription and protein transformation, Matthew Perry for his help in sequencing plasmids, Scott Brown and Brian Baker for introducing me to the microfabrication facilities, Curtis King and Ted Ayliffe for assisting in device fabrication and platform machining, Ben Christensen for introducing me to histology, Patrick Tresco for allowing me to use his upright microscopes and Andras Pungor for help with circuit design. Katie Breneman, Suhrud Rajguru,

Marytheresa Ifediba, Jeff Wyrick, Tina Jovic, Micah Frerck and Jeff Wolchok also positively contributed to my time as a bioengineering graduate student.

Finally, I would like to thank my friends, boyfriend and family for all of their unconditional support and guidance. They made the hard times manageable and the good times great. I would particularly like to thank my brother, Ajay, my late mom, Rani, and my dad, Susheel, for their unconditional love and encouragement.

CHAPTER 1

INTRODUCTION

1.1 Motivation

Ion-channel pathologies, attributed to anomalies in protein structure, protein density and/or protein movement on the membrane, have been implicated in diseases including LongQT syndrome, cystic fibrosis, night blindness, epileptic episodes and migraines (Epstein *et al.*, 1997; Lehmann-Horn & Jurkat-Rott, 1999; Hille, 2001; Hubner & Jentsch, 2002). These findings, typically characterized using conventional pipette-based electrophysiological techniques, have resulted in treatments like gene-therapy and targeted protein-delivery that highlight the clinical relevance of basic biophysical research. However, the effective dielectric behavior of the cell membrane and associated membrane-bound protein structures at frequencies above 10 kHz is largely unknown because of bandwidth limitations associated with conventional electrophysiological techniques. The present work was motivated by the hypothesis that radio-frequency-based impedance measurements around a cell will reflect excitable changes in membrane–protein charge arrangement or membrane–protein complex mobility.

New techniques presented in this thesis integrate the principles of extracellular radio frequency (RF) interrogation with conventional two-electrode whole-cell voltage clamp (TEVC) to 1) spatially resolve effective membrane capacitance and 2) monitor excitable changes in effective membrane capacitance. Also, we introduce a new technique that provides an alternative strategy for extracellular electrode–electrolyte interfacial impedance estimation in a linear regime of electrode voltage–current sensitivity. Experimental results illustrate the potential of these new techniques to elucidate 1) changes in integral-membrane protein conformational state, 2) lipid-raft regional distribution, 3) change in size:charge:mobility ratio of membrane-bound protein-ion complexes (associated with specific protein types) during whole-cell voltage clamp, 4) exocytotic activity, 5) phospholipid headgroup rotations, 6) charge distribution around a polarized cell-type and 7) membrane–drug binding processes. Thus, the new methods presented in this thesis can supplement conventional pipette-based electrophysiological techniques to provide a more complete description of membrane biophysics.

1.2 Outline

This introduction is divided into five major sections. The first section presents a general background to electric impedance spectroscopy (EIS), which provides a foundation for the extracellular RF measurements performed as part of this dissertation. The three subsequent sections introduce work represented by chapters in the thesis. Sections include 1) 'Three Current-Passing Electrode Method (TCPE): A New Method to Estimate Electrical Double-Layer Impedance (Chapter 2)', 2) 'Spatially Resolving Dielectric Properties Around a *Xenopus* Oocyte (Chapter 3, (Dharia *et al.*, 2009))', and 3) 'Monitoring Membrane-Potential-Dependent RF-Impedance Changes of *Shaker*B-IR Proteins Expressed in *Xenopus* Oocytes (Chapters 4 (Dharia & Rabbitt, 2010) and 5 (Dharia & Rabbitt, Submitted))'. Each of these introductory sections contains pertinent

‘Background and Motivation’ and ‘Goals and Methodology’ subsections. Specific ideas and tangibles contributed by this dissertation are summarized in the last introductory section, ‘Contributions and Summary.’

1.3 EIS

In electric impedance spectroscopy, alternating currents/voltages are applied to a given material through a group/pair of electrodes, and the corresponding voltage/current change between the electrodes can be used to characterize the electrical properties of the material in question. This technique is well established, and has many applications in biology including cell counting (Hoffman & Britt, 1979; Coulter & Rodriguez, 1988; Gawad *et al.*, 2001; Holmes & Morgan, 2003), cell/protein characterization (Coulter & Rodriguez, 1988; Gritsch *et al.*, 1998; Ayliffe *et al.*, 1999; Gawad *et al.*, 2001; Treo *et al.*, 2004; Cheung *et al.*, 2005; Han & Frazier, 2006; Han *et al.*, 2006), cell separation (Han *et al.*, 2006) and tissue-culture monitoring (Keese & Giaever, 1994; Lo *et al.*, 1995; Ehret *et al.*, 1997; Pearce *et al.*, 2005; Rahman *et al.*, 2006; Rahman *et al.*, 2008).

Advances in microelectromechanical systems (MEMS) fabrication techniques provide a controllable approach to build systems on the micron scale, thereby enabling the application of EIS to single, excitable, living cells. EIS has been used to visualize outer ear hair cell resonance (Rabbitt *et al.*, 2005), quantify DNA content in fixed myeloma cells (Sohn *et al.*, 2000a), track cardiac myocyte contraction (Werdich *et al.*, 2004) and monitor pharmaceutical responses of bovine chromaffin cells (Gritsch *et al.*, 1998). Generally, MEMS-based EIS devices consist of a series of (exposed) planar electrodes in a photo-patterned polymer-based recording channel. A cell is positioned on top of the electrodes in the recording channel, and the cell's response to drug application and/or extracellularly applied electric fields across the channel is recorded. The planar nature of MEMS-based technologies generally results in an enclosed recording channel (to enable fluidic control), and this limits conventional electrophysiological pipette-access to the cell during EIS recording.

Here we introduce techniques that integrate both MEMS- and rapid-prototyping-based technologies to enable simultaneous two-microelectrode whole-cell voltage-clamp and EIS measurements around isolated, living cells. These techniques, as described in Chapters 3, 4 and 5, were used to 1) spatially resolve differences in membrane dielectric and 2) monitor excitable RF-impedance change associated with protein activity. A new method to simultaneously estimate double-layer and interelectrode impedances, in a linear regime of electrode voltage–current sensitivity, is also included as part of this dissertation (Chapter 2). Preliminary simulations indicate that this method could potentially facilitate both electric impedance spectroscopic and electric impedance tomographic recordings.

1.4 The Three Current-Passing Electrode Method: A New Method to Estimate Electrical Double-Layer Impedance

1.4.1 Motivation and Background

Ion accumulation at the electrode–electrolyte interface, partially an effect of solution-based electrostatic interactions with a charged electrode, results in the well-documented electrode–electrolyte interfacial impedance (double-layer impedance) (Bard & Faulkner, 2001). This interfacial impedance is significant over a wide range of recording frequencies, and parallel resistor-capacitor (RC) circuits are generally used to model double-layer impedances at low frequencies (as they can be used to explain the passage of direct current), while series RC circuit-models are typically used for higher frequency recordings (Geddes, 1997). However, double-layer impedance has proven difficult to model for an arbitrary system, as double-layer effects have been shown to nonlinearly vary with current density, frequency, material-type, electrolytic solution and duration of electrode use (Schwan, 1968; Geddes, 1972; Boer & Oosterom, 1978; Simpson *et al.*, 1980; Onoral & Schwan, 1982; Ilic *et al.*, 2000; Cui & Martin, 2003; Franks *et al.*, 2005; Mirtaheri *et al.*, 2005).

Two methods to experimentally estimate double-layer impedances for a given recording chamber require measurements made 1) over multiple (a minimum of two) calibration solutions or 2) using multiple (a minimum of two) interelectrode distances. Every impedance measurement consists of a series addition of electrode double-layer impedances and an associated interelectrode solution resistance. Double-layer impedance is assumed to be constant during these measurements, and subtracting measured impedances 1) between different calibration solutions or 2) at different interelectrode distances corresponds to a change in interelectrode resistance only (double-layer impedances subtract out of measurement). This differential impedance value, in conjunction with a model for solution resistance like that shown in Eq. 1.1

$$R = \frac{\rho L}{A} \tag{1.1}$$

(ρ - solution resistivity, L – distance between electrodes, A – the current-density dependent, effective cross-sectional area of recording chamber), and a method to estimate solution resistivity like that shown in Eq. 1.2

$$j = |Z|F[C]\mu E = \sigma \frac{dV}{dx} \tag{1.2}$$

(simplified version of the Nernst-Plank equation (i.e. Ohm's Law) for uniform (in space and time) calibration solution concentrations; j - current density, Z - valence of the charge carrier, C - the concentration of the charge carrier, μ - the mobility of the ionic species, σ(1/ρ) - solution conductivity, E - the electric field) can be used to calculate the effective cross-sectional area of the recording chamber, and subsequently, individual solution resistances and combined double-layer impedance values (Weiss, 1996).

There are, however, several potential problems that arise from these double-layer impedance estimation strategies. For example, if the solution resistance is much lower than the double-layer impedances, noise might prevent accurate solution impedance measurement that would then affect the accuracy of double-layer estimation (Schwan, 1968). Furthermore, double-layer is also known to significantly change based on interelectrode material, and introducing a cell or protein into the interelectrode space can significantly affect double-layer impedance estimates made using calibration solutions. Lastly, these double-layer estimation methods are usually performed before or after recording across an analyte of interest, and cannot be used to determine the temporal dependencies of double-layer impedance while recording from the analyte.

As such, alternative methods have been implemented to completely bypass the double-layer estimation challenge. One such method uses difference-based impedance measurements, where a change in impedance is calculated by subtracting a control EIS measurement from the measurement of interest (Schwan, 1968). One caveat of this approach is that it cannot be used to calculate absolute interelectrode (chamber) impedance values; instead, this subtraction-based method only allows for relative comparisons (compared to the control) of chamber impedances. This subtraction-based method is used in Chapters 3-5 of this dissertation, where relative changes in membrane impedance were of interest.

The four-electrode method is the most common method to bypass the double-layer impedance estimation challenge (Schwan, 1968). In the four-electrode method, two recording-only electrodes are placed between two current-passing electrodes, and the electrodes are distributed such that the electrode–electrolyte interface on the stimulating sites does not interfere with the recording sites. The recording electrodes have infinite (theoretically) input-impedances, preventing current flow and double-layer formation at their electrode–electrolyte interface (Schwan, 1968; Kalinowski & Figaszewski, 1995). As such, the voltage drop measured between the two recording sites reflects the voltage drop in the recording channel (interelectrode impedance). However, in many MEMS-based applications, implementing the four-electrode method is not convenient due to the size of the system (electrode-spacing cannot be achieved) and the multiple materials required to obtain the different electrode types. Furthermore, achieving a high (current-stopping) recording electrode input-impedance can prove difficult in any system. To address these challenges, we have designed a new method, the three current-passing electrode method (TCPE), that simultaneously estimates chamber (interelectrode) and double-layer impedances.

1.4.2 Goals and Methodology

In TCPE, the double-layer impedance and localized chamber impedances associated with three current-passing electrodes (3 double-layer impedances and 3 chamber impedances) are simultaneously estimated in a linear voltage–current electrode regime. Six different pairs and groups of the three electrodes are selected for unique impedance measurements. A lumped electrical parameter model is created for each electrode recording configuration using symbolic double-layer and chamber impedance elements. The Levenburg-Marquadt algorithm, a nonlinear least-squares algorithm that uses components of both the Newton-Raphson root-finding method and the steepest ascent minimization approach, is then used to minimize error between simulated noisy measurements and the symbolic lumped-parameter-based representation of every electrode measurement configuration (Chapra & Canale, 2002). The set of parameter values that correspond to the minimized error level should constitute the desired chamber and double-layer impedance estimates. The accuracy of TCPE estimation is characterized for different ratios of average chamber to double-layer impedance values, after adding variable amounts of noise in the simulated measurements and error to the least-squares parameter guesses. The results, shown in Chapter 2, indicate that TCPE could potentially be a viable method for simultaneous double-layer and chamber impedance estimation in a linear voltage–current electrode regime.

1.5 Spatially Resolving Dielectric Properties Around a *Xenopus* Oocyte

1.5.1 Motivation and Background

Polarized cell-types, including mammalian spermatozoon, renal epithelial cell types, retinal rod cells and more classically, neurons, are organized into functionally important protein- and lipid- domains (Singer & Nicolson, 1972; Piepenhagen & Nelson, 1998; Hille, 2001; Malinska *et al.*, 2003). Regulation of the ratio of cholesterol to phospholipids in the acrosomal region of spermatozoon cells, for example, strongly affects spermatozoon fusion with an egg cell, while retinal rod cells contain high amounts of the protein-portion of the pigment rhodopsin in their retinal disk membranes to achieve adequate light sensitivity (Corless *et al.*, 1982; Ladha, 1998). Furthermore, localized liquid-ordered lipid domains (‘lipid rafts’ and/or ‘caveolea’, 25 nm – 700 nm diameters) have been targeted as ‘hot spots’ for signal transduction (McLaughlin & Aderem, 1995; Brown & London, 1998; Munro, 2003); in fact, caveolae have been implicated in the regulation of endothelial nitric oxide synthase activity, an enzyme essential to processes including angiogenesis, vasorelaxation and vessel permeability (Li *et al.*, 2005). However, spatially localized dielectric measurements around isolated whole cells that rapidly enable the detection of compositionally distinct membrane localities have been difficult to achieve.

Localized membrane-based measurements using pipette-based electrophysiological techniques require the arduous task of patching regularized, small domains of the cell membrane while simultaneously minimizing cellular leak currents. Furthermore, dielectric measurements are difficult to make using pipette-based techniques because the parasitic capacitance of pipettes limits recordings to relatively low frequencies (< 1 kHz)

(Cahalan & Neher, 1992a; 1997; Stuhmer, 1998). Vibrating probe-based methods have been used to spatially resolve membrane currents in gamete-like cells (Jaffe & Nuccitelli, 1974; Robinson, 1979). However, the frequency of probe vibration in these methods is limited by viscous effects on probe mass, and measurements require high integration times (~10 seconds). Preliminary data collected around outer hair cells (1 kHz – 100 kHz) indicate that electric impedance spectroscopy could successfully be used to visualize differences in membrane dielectric (Rabbitt *et al.*, 2005). Chapter 3 introduces a new method, 'sce-Topo', to accomplish this goal.

1.5.2 Goals and Methodology

Sce-Topo uses localized RF impedance measurements around a single cell to visualize spatially resolved membrane dielectric properties. *Xenopus* oocytes are used as a model cell in preliminary sce-Topo experiments because of their polarized structure; *Xenopus* oocytes (~1.2 mm diameter) consist of two visually identifiable 'animal' (brown/black) and 'vegetal' (white/yellow) hemispheres, and the polarization of *Xenopus* oocytes has been associated with hemispherical differences in protein expression, sub-granular melanin content and asymmetries in intracellular distribution of the nucleus, yolk platelets and RNA production mechanisms (Robinson, 1979; Dascal, 1987; Gomez-Hernandez *et al.*, 1997; Chang *et al.*, 1999; Weber, 1999). As such, it is hypothesized that either hemisphere of an oocyte will have a difference in membrane dielectric, and that these differences will be discernable using sce-Topo.

The device and algorithm introduced in Chapter 3 are scalable, and a long-term goal for this technology is to visualize localized dielectric properties around micron-sized cells. Spatial resolution increases with electrode number, and utilizing techniques like electron-beam lithography could facilitate the fabrication of nanometer-sized electrode-widths to potentially enable detection of the signaling-intensive liquid-ordered lipid domains. As such, sce-Topo could eventually be used in conjunction with scanning electrochemical microscopy, surface-plasmon resonance and fluorescence-based methods to facilitate detection of electrochemical and molecular events on the membrane by prescreening localized lipid bilayer areas for membrane activity (Shan *et al.*; Yu *et al.*, 1996; Wightman, 2006).

1.6 Monitoring RF-Impedance Changes of *Shaker*B-IR Proteins Expressed in *Xenopus* Oocytes

1.6.1 Motivation and Background

Membrane-delineated charge displacement currents, generally associated with excitatory membrane–protein charge rearrangements, cannot be measured using conventional pipette-based electrophysiological techniques due to stray capacitances associated with the glass/quartz pipette interface. Cut-open vaseline-gap (COVG), a specialized voltage-clamp technique, addresses this challenge by carefully compensating for the capacitance associated with a single glass/quartz microelectrode to enable voltage-clamp rise times as low as 25 μs during whole-cell *Xenopus* oocyte recording (Stefani & Bezanilla, 1998). *Xenopus* oocytes are model cells for COVG because they express exogenous proteins in their membrane with densities up to 10 times that of their endogenous protein levels, and as such, can amplify specific exogenous protein response (Stuhmer, 1998). Furthermore, the COVG platform allows for ion-channel blocker application to the electrically isolated, permeabilized, bottom-half of a *Xenopus* oocyte, thereby eliminating signals associated with ion-channel conduction. These technically difficult recordings, made using a measurement bandwidth of 5 kHz, have successfully been used to detect excitatory changes in ion-channel voltage-sensitive domain (voltage sensor) movement that generally precedes ionic conduction (Stefani & Bezanilla, 1998). However, even this technique is not sensitive enough to visualize other nonconductive changes in ion-channel conformational state or resolve changes in voltage-sensor movement at timescales less than 20 μs.

Instead, other methods have been used to indirectly monitor smaller, rapid changes in membrane charge arrangement (Hille, 2001). One method, the fast patch-clamp method, extends the capabilities of COVG by integrating a larger recording pipette size (10-20 microns diameter tips) to further minimize voltage-clamp rise-time to a ~10 μs timescale (Sigg *et al.*, 2003b). Noise fluctuation analysis, applied on several data sets collected using the fast patch-clamp technique, has successfully been used to recognize quantized charge movement associated with voltage-sensor activity on both sodium and potassium ion channels (Cole, 1968; Armstrong & Bezanilla, 1974, 1977a; Bezanilla & Armstrong, 1977; Conti & Stuhmer, 1989; Sigg *et al.*, 1994; Loots & Isacoff, 1998; Bezanilla, 2000a; Hille, 2001; Bezanilla, 2005; Tombola *et al.*, 2005). These time-intensive fast patch-clamp recordings have also been used in conjunction with kinetic models based on single ion-channel recordings to identify multitudes of channel-dependent open, inactive and closed conformational states. In this way, these challenging techniques have significantly contributed to a better understanding of ion-channel biophysics.

Here we propose a new technique that may simplify displacement-current recording strategies by using extracellularly applied RF signals to vibrate excitable membrane-bound charges. While the RF response of a protein in a living cell membrane is unknown, it is hypothesized that impedance changes associated with membrane-associated RF vibration during whole-cell depolarization will reflect changes in membrane–protein charge arrangement or protein–membrane complex mobility. This might elucidate properties associated with protein–membrane domain size, charge and mobility. Eventually, it is hoped that this technology complements other electrophysiological methods to further elucidate membrane biophysics.

1.6.2 Goals and Methodology

The new technique discussed above, which monitors RF changes associated with protein–membrane vibration during whole-cell voltage clamp, is calibrated in Chapter 4 and implemented in Chapter 5. The potential of the technique is explored by monitoring changes in RF vibration associated with a well-studied K^+ ion channel, *Shaker*B-IR, expressed in *Xenopus* oocytes. The N-terminus of the wild-type *Shaker* channel, implicated in fast-inactivation, has been removed from the *Shaker*B-IR channel. As such, the ionic conduction currents associated with the *Shaker*B-IR channel, predominately noticeable above the channel's half activation potential of ~-27 mV, should remain fairly constant after ion-channel activation (Hoshi *et al.*, 1990; Islas & Sigworth, 1999), and excitable changes in measured membrane RF impedance will predominately reflect differences in a closed vs. open ion-channel conformational state. Specific biophysical phenomena that may cause a measurable change in RF vibration include 1) *Shaker* voltage-sensor displacement (1-2 ms after cellular excitation), 2) ion–pore interactions and 3) activity-dependent charge distribution associated with the outer vestibule of the *Shaker*B-IR (associated with both channel activation and slow-inactivation (~100 ms time scale)) (Liu *et al.*, 1996; Hille, 2001).

In a subset of experiments, Cu^{2+} will be applied to *Shaker*B-IR expressing oocytes, and changes in RF vibration associated with membrane–Cu^{2+} interactions will be temporally resolved. There are several mechanisms by which a charged ion-channel inhibitor might alter ion-channel conduction; it might bind to 1) residues that line the ion-channel, 2) the lipid bilayer around the ion channel, 3) the lipid-bilayer–protein interface or 4) the lipid-bilayer–solution interface (Kaczorowski *et al.*, 2008). Cu^{2+}, a known potassium ion-channel inhibitor, has been shown to bind specifically to the S2-S3 domains of BK channels, in locations that are known to affect movement of the voltage-sensitive domain (Ma *et al.*, 2008). It is likely that copper binds in a similar location in *Shaker* channels (due to structural homologies between BK channels and *Shaker* channels (Ma *et al.*, 2008)), and as such, it is hypothesized that the RF impedance associated with the mobility:size:effective charge ratio of these *Shaker*B-IR domains will change after Cu^{2+} application. While the measured RF change may be membrane-potential dependent, data collected by Ma *et al.* indicate that Cu^{2+} may preferentially bind to the resting state of BK channels. As such, it is possible that the RF signals associated with the *Shaker*B-IR–Cu^{2+} complex will experience noticeable differences in measured RF impedance at potentials below those associated with ion-channel activation. Results will be used to estimate the capabilities of this technique to elucidate excitable changes in charged ion/molecule–protein interactions relevant to membrane biophysics and pharmacology.

1.7 Contributions and Organization

Here we introduce two new platforms, both based in EIS, which apply RF signals to extracellular electrodes to 1) spatially resolve the dielectric properties around a single cell membrane and 2) monitor changes in membrane dielectric associated with whole-cell voltage-clamp. While designing these platforms, we also developed a new method (TCPE, Chapter 2) that could potentially be used to simultaneously estimate electrode–electrolyte interfacial impedances and chamber (interelectrode) impedances in a linear electrode voltage–current regime (explicated in part via U.S. Patent Application No. 12/249,643). TCPE should be simpler to implement than the other conventional double-layer estimation strategies that require either multiple calibration solutions or moveable electrode architectures. TCPE may even facilitate chamber impedance measurements on size-limited platforms, where application of the four-electrode method can be difficult. As such, TCPE presents a potential contribution to any field where electrodes are used to record impedances in electrolytic solutions, including the other techniques introduced in this dissertation.

One such technique, sce-Topo (Chapter 4), used extracellular pairs of adjacent electrodes, which are part of a radially distributed multielectrode array, to measure localized RF impedances around a polarized *Xenopus* oocyte. The corresponding localized impedance measurements were used to spatially map the effective dielectric properties of the isolated oocyte membrane. Our findings were published as a journal article in Lab on a Chip (reprinted in Chapter 4 with permission) (Dharia *et al.*, 2009). The techniques mentioned in this paper are scalable, and could be applied to visualize micron-sized cell impedances after platform miniaturization. The ultimate aims for this technology would be to 1) characterize the dielectric properties of functionally polarized cell membranes and 2) detect localized clusters of lipid-rafts (liquid ordered lipid domains) on the membrane, known to be signaling hotspots.

A second platform, characterized using both mathematical simulations and preliminary recordings on *Xenopus* oocytes, was used to show that extracellularly applied RF signals are sensitive to excitable changes in membrane capacitance in a narrow frequency band. This platform, disseminated via a peer-reviewed conference proceeding (reprinted with permission in Chapter 5, (Dharia & Rabbitt, 2010)), shows that excitable changes in membrane impedance are the largest when measured at 300 kHz and 500 kHz. As such, the 500 kHz frequency was used to monitor RF impedance changes associated with *Shaker*B-IR (expressed in *Xenopus* oocytes) ion-channel activity and associated copper-ion—channel response at several membrane-potential levels (Chapter 6, (Dharia & Rabbitt, Submitted)). Preliminary results seem promising, and this technique might be used to monitor ion-channel conformational state changes and temporally resolve charged-molecule/drug–membrane binding processes to elucidate biophysically and pharmacologically relevant processes.

Contributions of this dissertation to the fields of engineering and science include 1) a method that could simultaneously estimate double-layer impedances and chamber impedances in a linear range of electrode voltage–current sensitivity, 2) development and implementation of a method to spatially resolve and visualize differences in dielectric properties around a single cell and 3) development and implementation of a method to temporally monitor RF impedance changes associated with protein activity and protein–charged biomolecule interactions.

CHAPTER 2

A THREE-ELECTRODE METHOD TO SIMULTANEOUSLY ESTIMATE ELECTRODE–ELECTROLYTE INTERFACIAL IMPEDANCES AND INTERELECTRODE IMPEDANCES

Technique introduced in Patent: "Systems and Methods for Measuring the Electrical Properties of a Microparticle." U.S. Patent Application No. 12/249,643 (Filed 10/2008, Rabbitt and Dharia).

2.1 Abstract

Here we introduce a new method, the three current-passing electrode method (TCPE), which can simultaneously estimate electrode–electrolyte interfacial impedance values and interelectrode (chamber) impedance values in a voltage-limited regime where electrode impedance is current-density independent. This method could simplify conventional double-layer estimation strategies that involve the use of multiple calibration solutions or moveable electrode architectures. During TCPE simulations, individual impedance values were assigned to 1) the interface of three independently addressable, current passing, electrodes and 2) localized areas within the recording chamber, between each pair of electrodes. Impedance measurements between 1) pairs of

electrodes (3 measurements) and 2) a shorted pair of electrodes and the remaining electrode (3 measurements) were simulated by numerically solving lumped electrical parameter models for each electrode configuration. Noise was added to the simulated measurements, and a nonlinear least-squares algorithm minimized error between the noisy simulations and the associated symbolic lumped parameter models. This least-squares error minimization provided impedance estimates for each of the interfacial and interelectrode parameters. Results indicated that impedance estimation was sensitive to measurement noise, error in the initial least-squares parameter guess and the average ratio of chamber to double-layer impedance. However, multiple averaged applications of TCPE, simulated using reasonable amounts of measurement noise (up to +/- 10%) and error in the initial least-squares parameter guess (up to +/-100%), produced parameter estimates that were within a conventionally acceptable range (within 10%) of their actual values. This indicates that TCPE, in a voltage-limited regime when electrode–electrolyte interfacial impedances are constant, might provide a useful alternative to conventional double-layer impedance estimation strategies.

2.2 Introduction

Electrode-based measurements in electrolytic solutions are commonly performed during electric impedance spectroscopy (Ayliffe *et al.*, 1999; Werdich *et al.*, 2004; Barnes, 2006; Dittami *et al.*, 2008; Rahman *et al.*, 2008; Dharia *et al.*, 2009), impedance-based flow cytometry and electric impedance tomography (Webster, 1990a; Brown, 2003b; Bayford, 2006). These emerging technologies have been used to sort/count different cell types and monitor gastrointestinal tract emptying, neonatal pulmonary response and breast tissue impedances (Brown, 2003b; Bayford, 2006). A challenge during these measurements, however, has been isolating the effect of the electrode–electrolyte interfacial impedances (double-layer impedances) from the interelectrode impedance (chamber impedance). Methods to experimentally characterize the electrode double-layer typically involve 1) multiple calibration solutions and a stationary pair of electrodes or 2) a moveable electrode configuration and a single calibration solution. However, double-layer impedances vary, often times nonlinearly, with frequency of stimulation, current density, material properties (both of the electrode and the solution between the electrodes) and time (Schwan, 1968; Geddes, 1972; Boer & Oosterom, 1978; Simpson *et al.*, 1980; Onoral & Schwan, 1982; Ilic *et al.*, 2000; Cui & Martin, 2003; Franks *et al.*, 2005; Mirtaheri *et al.*, 2005). As such, the experimental methods mentioned above might not accurately a) represent the impedance of the electrode interface when a biological solution/material is in the chamber (rather than the calibration solution) or b) account for time-varying changes in double-layer impedance during sample-of-interest recordings.

In response to these challenges, a four-electrode method has been developed to enable chamber impedance estimates without double-layer impedance estimation (Schwan, 1968; Kalinowski & Figaszewski, 1995). During four-electrode measurement, two high input-impedance recording-only electrodes are placed between two current-passing electrodes. The corresponding chamber impedance measured between the two recording electrode sites excludes double-layer effects, as the high-input impedance of these electrodes prevents ion-accumulation at the electrode interface (Schwan, 1968). However, even this method has inherent challenges. Four-electrode recordings are not always convenient in microsized systems, where diversity in metallization layers increases fabrication complexity. Additionally, there are channel-size limitations during four-electrode recording, and the two current-passing electrodes must be placed far enough away from the recording electrodes so that ions do not accumulate at the recording electrode–electrolyte interface. Lastly, input-impedances large enough to completely prevent current flow can be difficult to achieve, and nonideal recording electrodes can affect accuracy of four-electrode recordings.

Here we introduce a new method, the three current-passing electrode method (TCPE), that allows for simultaneous estimation of chamber and double-layer impedance elements using three current-passing electrodes in a magnitude-limited voltage regime, where double-layer electrode impedance values are independent of current density. The exact value of maximal voltage application during TCPE is material-dependent, although maximal voltage values have already been identified for several electrode material types (Schwan, 1968; Geddes, 1972; Simpson *et al.*, 1980; Mirtaheri *et al.*, 2005). During TCPE simulations, individual impedance values were assigned to 1) the interface of three independently addressable, current-passing, electrodes and 2) localized areas within the recording chamber, between each pair of electrodes (Fig. 2.1A). Impedance measurements were simulated for each electrode configuration using the electrical lumped parameter models shown in Fig. 2.1B, and noise was then added to these simulated measurements. Error was minimized between the noisy simulated measurements and the corresponding lumped parameter models to estimate chamber (Z_{c1}, Z_{c2}, Z_{c3}) and double-layer impedance parameters (Z_{d1}, Z_{d2}, Z_{d3}). Results indicated that parameter (impedance) estimates are sensitive to measurement noise, the value of the averaged chamber to double-layer impedance and error in the initial least-squares parameter guess values. However, multiple applications of TCPE, made assuming reasonable amounts of measurement noise (up to +/- 10%) and error in the initial parameter guess (up to +/- 100%), resulted in average parameter estimates that converged to within 10% of each actual parameter value. These preliminary estimates suggest that TCPE could enable simultaneous double-layer and chamber impedance parameter estimates in the linear regime of electrode voltage–current-density response.

2.3 Methods

Three electrodes were selected for recordings, and Fig. 2.1A shows the corresponding double-layer impedance elements (Z_{d1}, Z_{d2}, Z_{d3}) and chamber impedance elements (Z_{c1}, Z_{c2}, Z_{c3}) for the given recording chamber. Lumped parameter models were used to represent 1) pairwise electrode measurements (Fig. 2.1B, 1-3) and 2) measurements between a shorted pair of electrodes and the remaining electrode (Fig. 2.1B, 4-6), resulting in six lumped parameter models with six complex-valued unknowns (parameters). The equivalent impedances of the first three circuits (Fig. 2.1B, 1-3 -- Z_1, Z_2 and Z_3), shown here, were calculated using simple combinations of series and parallel impedance elements.

$$Z_1 = Z_{d1} + (1/Z_{c1} + 1/(Z_{c2} + Z_{c3}))^{-1} + Z_{d3} \tag{2.1}$$

$$Z_2 = Z_{d2} + (1/Z_{c2} + 1/(Z_{c3} + Z_{c1}))^{-1} + Z_{d1} \tag{2.2}$$

$$Z_3 = Z_{d3} + (1/Z_{c3} + 1/(Z_{c1} + Z_{c2}))^{-1} + Z_{d2} \tag{2.3}$$

The remaining equivalent impedances (Z_4, Z_5 and Z_6) were solved in Mathematica by applying Kirchoff's current laws to the circuits shown in Fig. 2.1B (4-6) (Mathematica Wolfram Research, Champaign, IL). The equivalent impedances for the circuit models representing Z_4, Z_5 and Z_6 have been broken into two parts for simplicity.

$$\begin{aligned} A = {} & (Z_{c3} Z_{d1} Z_{d2} + Z_{c2} Z_{d1} (Z_{c3} + Z_{d2}) + Z_{c3} (Z_{d1} + Z_{d2}) Z_{d3} + Z_{c2} (Z_{c3} + Z_{d1} + Z_{d2}) Z_{d3} \\ & + Z_{c1} (Z_{d1} Z_{d2} + Z_{c3} (Z_{d1} + Z_{d2}) + (Z_{d1} + Z_{d2}) Z_{d3} + Z_{c2} (Z_{c3} + Z_{d2} + Z_{d3}))) \end{aligned} \tag{2.4}$$

$$Z_4 = \frac{A}{((Z_{c2} + Z_{c3}) (Z_{d1} + Z_{d3}) + Z_{c1} (Z_{c2} + Z_{c3} + Z_{d1} + Z_{d3}))} \tag{2.5}$$

$$Z_5 = \frac{A}{(Z_{c3} (Z_{d1} + Z_{d2}) + Z_{c1} (Z_{c2} + Z_{d1} + Z_{d2}) + Z_{c2} (Z_{c3} + Z_{d1} + Z_{d2}))} \tag{2.6}$$

$$Z_6 = \frac{A}{(Z_{c3} (Z_{d2} + Z_{d3}) + Z_{c1} (Z_{c3} + Z_{d2} + Z_{d3}) + Z_{c2} (Z_{c3} + Z_{d2} + Z_{d3}))} \tag{2.7}$$

2.3.1 Population-based Distribution of Estimated Impedance Values

Each equivalent impedance was numerically solved for several ratios (.5, 1, 2, 3,4,5,10) of the average real and imaginary chamber-impedance value to its respective double-layer impedance value ($Z_{c\_real}/Z_{d\_real} = Z_{c\_imag}/Z_{d\_imag}$ (x-axis Fig. 2.2-2.4)); these numerical solutions assumed equal chamber impedance values of (2000 Ω - 2000 Ω * i) and ratio-dependent (Z_{c_real}/Z_{d_real}), equal-valued, double-layer impedances ($Z_{d1} = Z_{d2} = Z_{d3}$). A Levenburg-Marquardt nonlinear least-squares algorithm (built-in function, IGOR Pro 6.02A, WaveMetrics, Portland, OR) was used to estimate parameter values by minimizing error between the symbolic equivalent impedance equations and their corresponding calculated measurement values under the following conditions: noisy measurements (M_{noise}, Fig. 2.2), error in the initial least-squares parameter guesses (initial guess, G_0, Fig. 2.3) and a mixture of both of these conditions (Fig. 2.4). Measurement noise and error in the initial guess were randomly selected from a uniform distribution of values within a stated percentage ('level', (+/- 0, 10%, 20%, 30%, 40%, 60%, 80%, 90%, 100%)) of the actual measurement and/or parameter value (y-axis on Fig. 2.2-2.4).

Mean parameter estimates and the associated standard deviation of Z_{c1}, Z_{c2}, Z_{c3}, Z_{d1}, Z_{d2} and Z_{d3} were calculated for every noise and initial guess error level at every ratio of Z_{c_real}/Z_{d_real} and Z_{c_imag}/Z_{d_imag} after 50 simulations. Coefficients of variation (CoV, σ/μ) were calculated using mean parameter estimates and standard deviations for the averaged 1) real chamber impedance estimates, 2) imaginary chamber impedance estimates, 3) real double-layer impedance estimates and 4) imaginary double-layer impedance estimates. CoV contour plots (Fig. 2.2-2.4) were used to graphically depict the effects of measurement noise and/or initial guess error, as a function of Z_{c_real}/Z_{d_real}, on parameter estimation (Fig. 2.2-2.4).

2.3.2 Individual Parameter Values and TCPE Estimation

The effects of measurement noise (Fig. 2.5) and error in the initial guess (Fig. 2.6) were then monitored on individual parameter estimates Z_{c1}, Z_{c2}, Z_{c3}, Z_{d1}, Z_{d2} and Z_{d3}. Numerical solutions to each of the equivalent impedances shown in Fig. 2.1B were calculated assuming that each impedance component had both real and imaginary-values that were a given percent (0%, 10%, 20%, 30%, 40%) (see x-axis of Fig. 2.5 and Fig. 2.6) less than (Z_{c1_real}, Z_{d1_real}, Z_{c1_imag}, Z_{d1_imag}) or greater than (Z_{c3_real}, Z_{d3_real}, Z_{c3_imag},

Z_{d3_imag}) the respective values of Z_{c2} (2000 Ω, 2000 Ω) and Z_{d2} (500 Ω, 500 Ω). This percent variation between parameters was referred to as 'parameter spacing' (x-axis, Fig. 2.5, Fig. 2.6). TCPE was applied after 1) adding exactly 10% (solid lines Fig. 2.5) or 20% (dotted lines Fig. 2.5) measurement noise to each equivalent impedance Z_1-Z_6 (Fig. 2.5 – no error in the initial guess) or 2) adding exactly +50% (solid lines Fig. 2.6) or -50% (dotted lines, Fig. 2.6) error to each initial parameter guess (Fig. 2.6 – no measurement noise). All results were normalized to their actual impedance values (y-axis, Fig. 2.5 and Fig. 2.6), and the slope for impedance estimation accuracy versus parameter spacing was calculated for every parameter in both the noisy measurement and initial guess error conditions. Double-layer parameter estimates are shown in Fig. 2.5A and Fig. 2.6A, while chamber impedance estimates are shown in Fig. 2.5B and Fig. 2.6B. Estimated normalized parameter values for (Z_{c1_real}, Z_{d1_real}), (Z_{c2_real}, Z_{d2_real}) and (Z_{c3_real}, Z_{d3_real}) were shown in blue, orange and red, respectively.

2.3.3 Trial-averages of TCPE and Parameter Estimation Accuracy

Finally, individual parameter estimate convergence for Z_{c1}, Z_{c2}, Z_{c3}, Z_{d1}, Z_{d2} and Z_{d3} was monitored after averaging the results of multiple TCPE trials (3, 5, 10, 15, 20, 25, 30, 35, 40, 45, 50, 55, 60, 65 and 70 trials) together. This trial-averaged sensitivity of TCPE was monitored (real and imaginary impedance components separately) 1) for different average ratios of chamber to double layer impedance (Fig. 2.7) and 2) when individual parameters were spaced -20% (Z_{c1} and Z_{d1}) or +20% (Z_{c3} and Z_{d3}) away from a center parameter value (Z_{c2} and Z_{d2}) (Fig. 2.8). For the first purpose, equivalent impedance values (Z_1-Z_6) were calculated using actual complex-impedance values of Z_{c1},

Z_{c2} and Z_{c3} of (2000 Ω, -2000 Ω) at ratios of Z_{c_real}/Z_{d_real} and $Z_{c\_imag}/Z_{d\_imag} = 8$ (Panel A), Z_{c_real}/Z_{d_real} and $Z_{c\_imag}/Z_{d\_imag} = 4$ (Panel B) and Z_{c_real}/Z_{d_real} and $Z_{c\_imag}/Z_{d\_imag} = 1$ (Panel C). Double-layer impedance values were equal to each other ($Z_{d1}=Z_{d2}=Z_{d3}$), and the rectified values of the real and imaginary double-layer impedance components were also equal ($|Z_{d\_real}|=|Z_{d\_imag}|$). Towards the second purpose, lumped parameter equivalent impedances (Z_1-Z_6) were solved using the following values -- Z_{c1}=(1600 Ω,-1600 Ω), Z_{c2}=(2000 Ω, -2000 Ω), Z_{c3}=(2400 Ω, -2400 Ω), Z_{d1}=(400 Ω,-400 Ω), Z_{d2}=(500 Ω,-500 Ω) and Z_{d3}=(600 Ω,-600 Ω) (Fig. 2.8) -- such that average values of $Z_{c\_real}/Z_{d\_real} = 4$ and $Z_{c\_imag}/Z_{d\_imag} = 4$. TCPE simulations for both purposes were performed after adding up to +/- 10% measurement noise to each equivalent impedance calculation and up to +/- 100% error in the least-squares initial parameter value. As done previously, measurement noise and initial guess error was randomly selected from a uniform interval that spanned the stated percentage of each respective actual measurement and parameter value.

Fig. 2.7 shows the averaged real impedance estimates (left y-axis, solid lines, filled markers) and standard error of the means (SEM, right y-axis, dotted lines, outlined markers) for each parameter after normalization to their actual parameter value. Fig. 2.8 shows the nonnormalized trial-averaged impedance estimates, and error bars denote +/- 1 standard error of the mean. Significant difference between pairs of the estimated real-valued chamber impedances ($Z_{c\_real1} - Z_{c\_real2}$, $Z_{c\_real2} - Z_{c\_real3}$, $Z_{c\_real1} - Z_{c\_real3}$) and double-layer impedances ($Z_{d\_real1} - Z_{d\_real2}$, $Z_{d\_real2} - Z_{d\_real3}$, $Z_{d\_real1} – Z_{d\_real3}$) in Fig. 2.8 were tested using a two-tailed unpaired t-test after 70 trial-averaged simulations.

2.3.4 Real vs. Imaginary Impedance Component Estimation

It should be noted that both the real- and imaginary-valued impedance response was analyzed in all these experiments. In every case, the real- and imaginary-valued components of each individual chamber and double-layer impedance were assigned the same value. As such, the properties of real and imaginary impedance estimation for all of the simulations were identical and could be represented by either the real or imaginary data set. Only real-valued data were shown here.

2.4 Results

TCPE simulations, not shown here, indicated that parameter estimates were perfect with noiseless measurements and no errors in the initial parameter guess (as expected). Here we explore the ability of the TCPE method to accurately estimate impedance parameters after the addition of 1) measurement noise (M_{noise}) and 2) error in the initial least-square parameter guesses (G_0). The real and imaginary component for each individual impedance element in every simulation was equal, and as such, estimations of real impedance data were equivalent to imaginary impedance data (estimates of Z_{c_real} and Z_{d_real} are identical to the respective estimates of Z_{c_imag} and Z_{d_imag}, see Methods). As such, only the real values of TCPE impedance estimation are shown in the figures here.

2.4.1 Population-based Distribution of Estimated Impedance Values

Fig. 2.2 compared the effects of measurement noise (y-axis, Fig. 2.2) on TCPE-computed estimates of averaged real double-layer (Fig. 2.2A) and chamber (Fig. 2.2B) parameter values for several ratios of Z_{c_real}/Z_{d_real} (x-axis, Fig. 2.2, see Methods). The CoV (σ/μ) was used to represent spread in the estimated data and was computed using 50 TCPE applications at every ratio of Z_{c_real}/Z_{d_real} and for every measurement noise level (see Methods 2.3.1). Fig. 2.2 showed that the ratio of Z_{c_real}/Z_{d_real} dramatically affected the CoV for estimated chamber and double-layer impedance parameters: the CoV associated with Z_{c_real} exponentially increased at small values of Z_{c_real}/Z_{d_real} (Z_{c_real}/Z_{d_real} <1) and high amounts of measurement noise, while the CoV associated with Z_{d_real} increased approximately linearly as Z_{c_real}/Z_{d_real} increased. The initial parameter guesses that corresponded to Z_{c1}, Z_{c2}, Z_{c3} and Z_{d1}, Z_{d2}, Z_{d3} for this simulation were perfect (the assigned values, see Methods), and a CoV > 0 indicated decreasing precision in parameter estimation caused by noisy measurements. As such, data indicated that estimations of the complex-valued components of Z_{c_real}, Z_{c_imag}, Z_{d_real} and Z_{d_imag} are sensitive to measurement noise.

The effect of error in the least-squares parameter guesses on TCPE parameter estimation was then evaluated for averaged real double-layer impedance estimates (Fig. 2.3A) and averaged real chamber impedance estimates (Fig. 2.3B). These simulations were done without measurement noise (M_{noise}=0) at several ratios of Z_{c_real}/Z_{d_real}, and CoV was again used as an indicator of precision during parameter estimation. Results indicated that initial guess errors produced lower CoVs than comparable values of measurement noise (compare Fig. 2.2 and Fig. 2.3), but were not 0. As measurements were noiseless in these simulations, a CoV > 0 indicated that the least squares method was converging to a localized minima at parameter values other than the minima of interest, and that parameter estimation depended on the initial guess value to the least-squares minimization problem. Fig. 2.4 shows a more realistic interpretation of how small amounts of noise in the measurement (up to +/- 10%, see Methods) will affect the CoV of parameter estimation for varying amounts of error in the initial guess (y-axis) at several ratios of Z_{c_real}/Z_{d_real} (x-axis). Trends in this case are similar to those shown in Fig. 2.3, but with slightly higher CoVs.

2.4.2 Individual Parameter Values and TCPE Estimation

Next, we evaluated the effects of measurement noise and error in the initial guess on individual chamber and double-layer impedance parameter estimates. In both the noisy measurement and initial guess error conditions (Fig. 2.5 and 2.6, respectively), actual values of Z_{c2_real} and Z_{d2_real} were held constant at 2000 Ω and 500 Ω, respectively ('middle values'), Z_{c1_real} and Z_{d1_real} were a given percent ('parameter spacing', see x-axis of Fig. 2.5 and Fig. 2.6) less than these middle values, and Z_{c3_real} and Z_{d3_real} were a given percent ('parameter spacing', see x-axis of Fig. 2.5 and Fig. 2.6) greater than these middle values (see Methods). Estimated parameter values were normalized to their actual values (y-axis, Fig. 2.5 and Fig. 2.6), and parameter estimates are increasingly accurate as their normalized values approach 1.

Fig. 2.5 illustrates the effects of adding exactly 10% (solid lines) and 20% (dotted lines) measurement noise (no error in G_0) to every equivalent impedance, Z_1-Z_6 (Fig. 2.1B) before least-squares parameter estimation (single TCPE application, Fig. 2.5A - double-layer impedance estimates, Fig. 2.5B - chamber impedance estimates). Data indicated that measurement noise equally contributed to the final parameter estimates for equal-valued chamber, and separately, double-layer impedances (a parameter spacing value of 0). For nonequal chamber and double-layer impedance parameter values (parameter spacing > 0), however, the noise added to each equivalent impedance before TCPE simulation resulted in chamber and double-layer impedance estimates of varying accuracy (Fig. 2.5A and 2.5B). Parameter accuracy increased for some parameters and decreased for others (when compared to parameter spacing = 0), and the standard deviation associated with parameter estimation accuracy increased as parameter spacing increased. The measurement-noise induced change in parameter estimation accuracy with parameter spacing (the slope of each line) was linear for every respective double-layer and chamber parameter value, and the slope of each line was exactly two times larger in the 20% noisy measurement condition (dotted lines) than the 10% noisy measurement condition (solid lines). Interestingly, an increase in parameter spacing causes a respective increase and decrease in the estimation of the largest and smallest parameter values during double-layer estimation, although these trends reverse during chamber impedance estimation. These phenomena might be explained by examining the actual parameter impedance values and the nonlinear nature of the equations that describe Z_1-Z_6, although further investigation is needed to completely understand these results.

Fig. 2.6 shows the effects of introducing exactly +50% (solid lines) and - 50% (doted lines) error into the least-squares initial guess (no measurement error) on TCPE parameter estimation (Fig. 2.6A - double-layer impedance estimates and Fig. 2.6B - chamber impedance estimates). Again, when chamber and separately double-layer impedance values were equal (parameter spacing = 0), initial guess error contributed equally to each parameter estimate. However, when parameter spacing > 0, impedance estimation depended on the actual parameter value and larger parameter values resulted in more accurate estimates than smaller parameter values (for both chamber and double-layer impedances). Estimation accuracy linearly changed for each parameter as parameter spacing increased, and rate of change of impedance estimates (with parameter spacing) made with +50% initial guess error (solid lines) had the same scalar value but opposite sign of the -50% initial guess error condition (dotted lines). As such, it seems that error in the initial guess may produce impedance estimates that are symmetric across the normalized impedance value of 1 (where the impedance estimation is perfectly accurate), and this information might be incorporated into TCPE to enable more accurate parameter estimates.

2.4.3 Trial-averages of TCPE and Parameter Estimation Accuracy

Data indicate that in cases of high CoV, averaging parameter estimates from multiple applications of TCPE (trial-averaging) may be necessary for accurate parameter estimation. Fig. 2.7 shows the effects of trial-averaging on final parameter estimation (trial-averaged estimate, x-axis shows number of averaged simulations) for multiple ratios of average Z_{c_real}/Z_{d_real} (see Methods, panel A shows $Z_{c\_real}/Z_{d\_real}=8$, panel B shows $Z_{c\_real}/Z_{d\_real} = 4$ and panel C shows $Z_{c\_real}/Z_{d\_real}=1$). Measurement noise in these experiments was selected from a uniform distribution that spanned +/-10% of each actual equivalent impedance value, and error in the initial parameter guess was selected from a uniform distribution that spanned +/- 100% of each actual parameter value (see Methods). The trial-averaged estimate for each parameter is normalized to its actual value and is shown using solid lines and markers in Fig. 2.5 (left y-axis). The gray bar, centered at a normalized impedance of 1, included all estimates that were within +/-10%

of the actual parameter value. Normalized standard errors of the mean (SEM, right y-axis) for each parameter, denoted by dotted lines and outlined markers, were also shown on the same graph. SEM plateaus to near its minimum value at ~10 trials for both chamber and double-layer impedance values when $Z_{c\_real}/Z_{d\_real} \geq 4$. When average $Z_{c\_real}/Z_{d\_real}=1$, however, even while double-layer impedance estimates approach 10% of their original value within 10 trials, 70-trial averaged chamber impedance estimates were as high as ~30% inaccurate. This indicates that trial-averaging might be used to accurately determine impedance estimates, although final estimation accuracy depends on ratio of Z_{c_real}/Z_{d_real} and the parameters of interest.

To see if TCPE could discern significant differences in Z_{c1}, Z_{c2}, Z_{c3}, and separately Z_{d1}, Z_{d2} and Z_{d3} after trial-averaging, Z_{c1} and Z_{c3} were respectively assigned values -20% and +20% of a middle chamber impedance value (Z_{c2}), while Z_{d1} and Z_{d3} were respectively assigned values that were -20% and +20% of a middle double-layer impedance value (Z_{d2}, see Methods). Parameter values were selected such that Z_{c_real}/Z_{d_real} and $Z_{c\_imag}/Z_{d\_imag}= 4$, with initial guess errors of up to +/- 100% and measurement noise of up to +/- 10% (see Methods). The x-axis in Fig. 2.8 shows the number of averaged parameter values (applications of TCPE), while the y-axis shows raw (nonnormalized) impedance values. The straight nonmarkered lines indicate the actual impedance associated with each parameter (blue- Z_{c1}, Z_{d1} orange-Z_{d2}, Z_{c2} red- Z_{d3}, Z_{c3}). Statistical significance testing showed significant differences between all chamber and double-layer pairs (($Z_{c\_real1} - Z_{c\_real2}$, $Z_{c\_real2} - Z_{c\_real3}$, $Z_{c\_real1} - Z_{c\_real3}$, $Z_{d\_real1} - Z_{d\_real2}$ and $Z_{d\_real1} - Z_{d\_real3}$) except $Z_{d\_real2} - Z_{d\_real3}$ after 70 trial-averages (p = .05).

2.5 Discussion

The three current-passing electrodes method, introduced here, used a least-squares regression to estimate the value for each impedance element of the model shown in Fig. 2.1 (Z_{d1}, Z_{d2}, Z_{d3}, Z_{c1}, Z_{c2}, Z_{c3}). This was done without multiple calibration solutions or moveable electrode architectures, and chamber and double-layer impedance elements were solved simultaneously after recording. Data indicated that chamber impedances were most effectively estimated for larger average ratios of Z_{c_real}/Z_{d_real} and Z_{c_imag}/Z_{d_imag}, double-layer impedances were most effectively estimated for smaller average ratios of Z_{c_real}/Z_{d_real} and Z_{c_imag}/Z_{d_imag}, and both chamber and double-layer impedances were estimated with approximately equal accuracy at a ratio of Z_{c_real}/Z_{d_real} and $Z_{c\_imag}/Z_{d\_imag} = 4$. Parameter estimation is most accurate after minimizing measurement noise and error in the least-squares parameter guess, and also depends on the actual values of each parameter. If these noise/error limits are not confined and relative parameter values are unknown, multiple applications of TCPE may be needed to correctly estimate parameter values. Trial-averaging of TCPE parameter estimates achieved double-layer and chamber impedance accuracies within 10% of the original parameter values in as few as 10 trials (for some ratios of Z_{c_real}/Z_{d_real}) and indicate the potential utility of this technique to determine chamber and double-layer impedances. One caveat of the trial-averaged simulations described here is that initial guess error was randomly selected from a distribution centered around the actual parameter value; even while the parameter estimation error range was high (up to +/- 100% initial guess error), TCPE would more accurately be simulated using a mean distribution value for initial guess error different than the actual parameter value (this should be done in the future).

Methods to potentially heighten parameter estimation accuracy include lowering the tolerance used to determine least-squares convergence or applying a perturbation to a converged solution to ensure convergence to a global minima rather than a local minina. This could reduce the number of TCPE applications necessary for accurate parameter estimation. Incorporating a fourth current-passing electrode to TCPE might also increase solution accuracy. While adding an extra current-passing electrode to the measurement would increase the number of total parameters (4 more parameters – 1 more double-layer parameter and 3 additional chamber parameters), the number of potential recordings would increase by more than this amount, resulting in redundant data that could potentially be used to hone accuracy during least squares parameter estimation.

Implementation of TCPE will ideally incorporate remotely controllable, individually addressable electrodes to facilitate pair- and group-wise electrode recordings. Electrical switches can operate on submillisecond time scales, and fast recordings will minimize errors due to temporal changes in double-layer impedance. Average ratios of Z_{c_real}/Z_{d_real} and Z_{c_imag}/Z_{d_imag} can be controlled by changing electrode height or electroplating electrodes to increase surface area, and could enable more accurate estimation of chamber impedance (by lowering double-layer impedance) (Ilic *et al.*, 2000; Cui & Martin, 2003; Werdich *et al.*, 2004; Franks *et al.*, 2005; Dharia *et al.*, 2009). Preliminary data indicate that TCPE could also be used to simultaneously estimate both chamber and double-layer impedances for ratios of Z_{c_real}/Z_{d_real} and Z_{c_imag}/Z_{d_imag} ~=4. While additional simulations and experiments need to be conducted to ensure TCPE accuracy, preliminary data indicate that this system may simultaneously estimate chamber and double-layer impedances. This cannot be accomplished using current methodologies, and as such, TCPE promises to simplify design architectures or electrode calibration strategies in any electrode-in-electrolyte recording including those made during electric impedance tomography or electric impedance spectroscopy.

Fig. 2.1 – An Overview: The Three Current-Passing Electrode Model (TCPE) – TCPE simultaneously estimated the electrode double–layer (Z_{d1}, Z_{d2}, Z_{d3}) and localized chamber (Z_{c1}, Z_{c2}, Z_{c3}) impedances associated with three selected electrodes (A). Electrical lumped parameter models were used to represent measurements between 1) every pair of electrodes (B, 1-3 – with associated equivalent impedances of Z_1, Z_2, Z_3) and 2) a shorted pair of electrodes and the remaining electrode (B, 4-6 – with associated equivalent impedances Z_4, Z_5, Z_6). A least-squares method was used to estimate each parameter value (Z_{d1}, Z_{d2}, Z_{d3}, Z_{c1}, Z_{c2}, Z_{c3}) by minimizing error between the electrical lumped parameter models and an associated set of simulated noisy measurements.

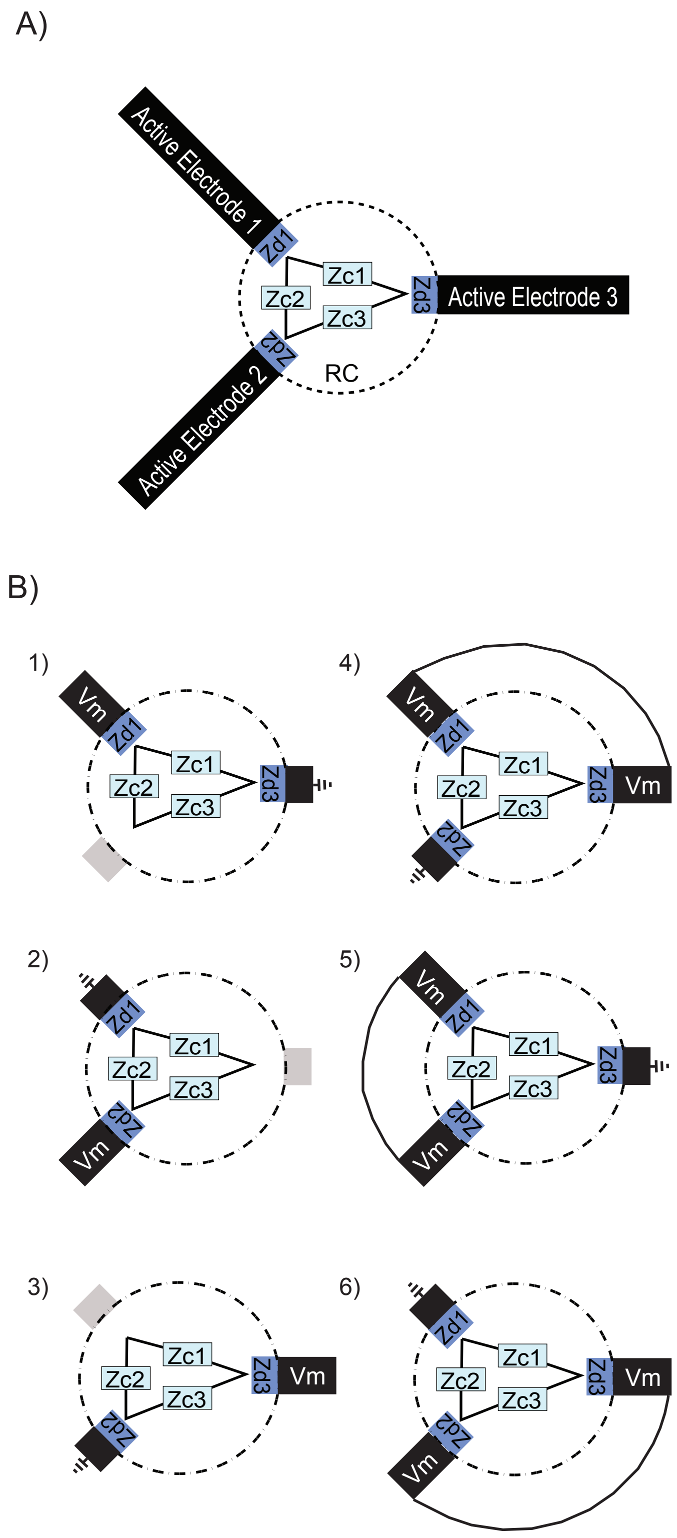
A)
Active Electrode 1
Active Electrode 2
Active Electrode 3
Zd1
Zd2
Zd3
Zc1
Zc2
Zc3
RC
B)
1)
2)
3)
4)
5)
6)
Vm

Fig. 2.2 – Noisy Measurements and Parameter Estimation – Noise, added to each set of six equivalent impedances (Z_1, Z_2, Z_3, Z_4, Z_5, Z_6), was randomly selected for each measurement from a uniform distribution that spanned +/- a given % of the specific measurement value (y-axis). Equivalent impedances were calculated using chamber impedance values (Z_{c1}, Z_{c2}, Z_{c3}) of (2000 Ω, -2000 Ω), and equal double-layer impedances whose values can be calculated using the stated ratio of the average Z_{c_real}/Z_{d_real} (x-axis). TCPE was run 50 times at every noise level and ratio of Z_{c_real}/Z_{d_real}, and the coefficient of variation (CoV) that corresponded to the average chamber and double-layer impedance parameter estimates for each of these points is shown here (double-layer impedance (A) and chamber impedance (B)). Contour lines indicate equivalent levels of CoV (darker line color indicates larger CoV), and results indicated double-layer impedances were more sensitive to measurement noise at large ratios of Z_{c_real}/Z_{d_real} (A) while chamber impedances were more sensitive to measurement noise at smaller ratios of Z_{c_real}/Z_{d_real} (B).

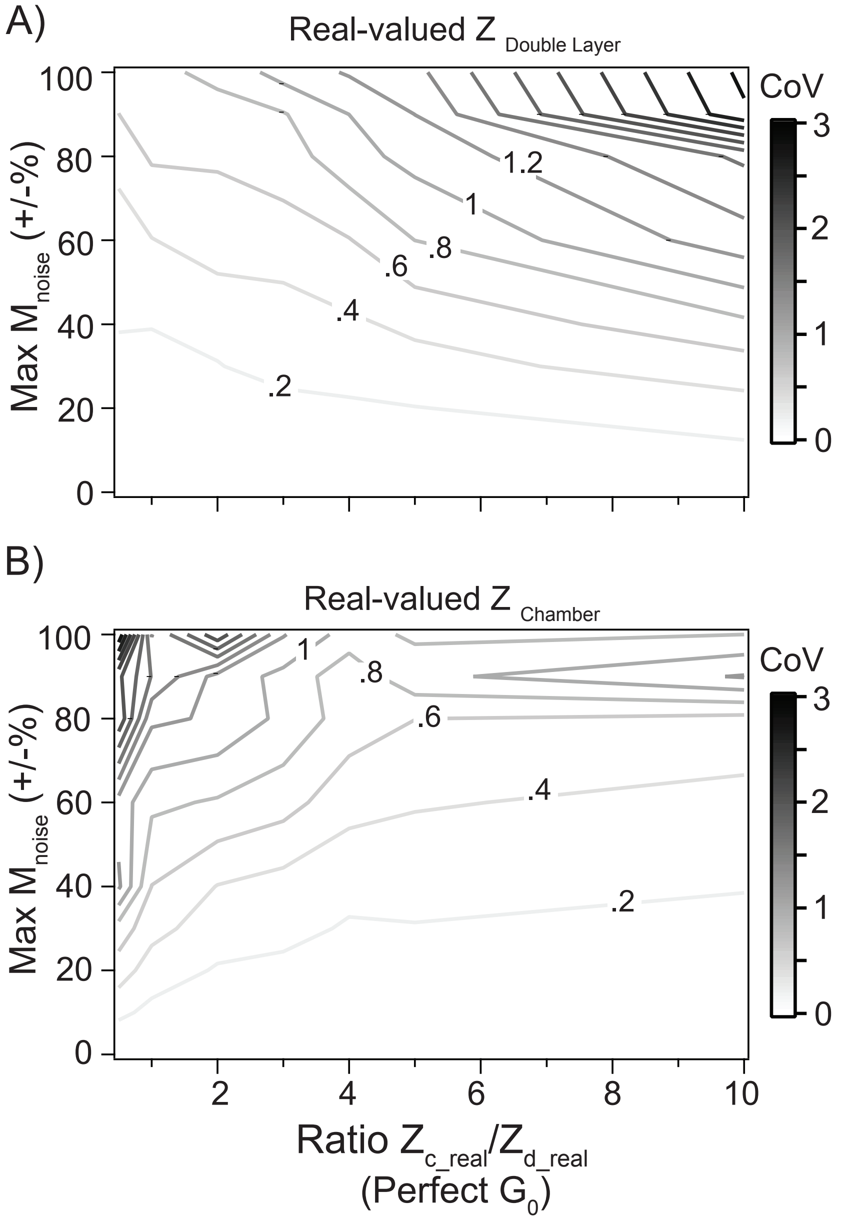
A)
Real-valued Z Double Layer
Max M_{noise} (+/-%)
100
80
60
40
20
0
1.2
1
.8
.6
.4
.2
CoV
3
2
1
0
B)
Real-valued Z Chamber
Max M_{noise} (+/-%)
100
80
60
40
20
0
1
.8
.6
.4
.2
CoV
3
2
1
0
2
4
6
8
10
Ratio Z_{c_real}/Z_{d_real}
(Perfect G_0)

Fig 2.3 – G_0 Error and Parameter Estimation – Equivalent impedances for each electrode recording configuration (Z_1, Z_2, Z_3, Z_4, Z_5, Z_6) were calculated using the same values of chamber and double-layer impedance detailed for Fig. 2.2. Error was added to each initial parameter guess value before TCPE simulation, and the amount of error was randomly selected from a uniform distribution that spanned a given percentage (+/- %, y-axis) of the actual parameter value. TCPE was applied 50 times for each 'error in the initial guess' level (+/- %, y-axis, see Methods) and for every average ratio of Z_{c_real}/Z_{d_real} (x-axis, see Methods), and the CoV (σ/μ) associated with the average double-layer impedance estimates (A) and chamber impedance estimates (B) at each point are depicted here. Contour lines indicate equivalent levels of CoV (darker line color indicates larger CoV), and nonzero values indicate that the average double-layer (A) and chamber (B) parameter estimates are, for at least some of the 50 trials, converging to localized minima other than the minima of interest.

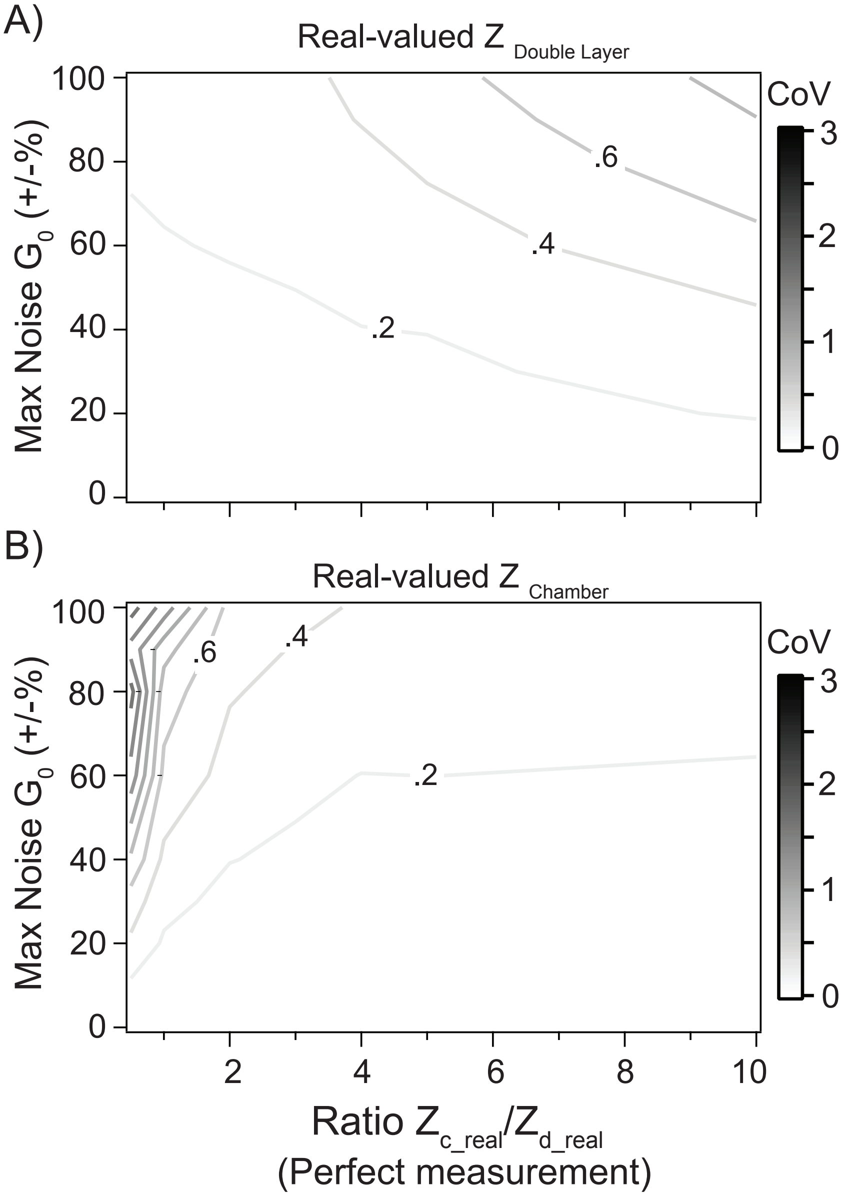
A)
Real-valued Z Double Layer
Max Noise G0 (+/-%)
100
80
60
40
20
0
.2
.4
.6
CoV
3
2
1
0
B)
Real-valued Z Chamber
Max Noise G0 (+/-%)
100
80
60
40
20
0
.2
.4
.6
CoV
3
2
1
0
2
4
6
8
10
Ratio Zc_real/Zd_real
(Perfect measurement)

Fig. 2.4 – Measurement Noise, Guess Error and Parameter Estimation – Noise, added to each set of six equivalent impedances (Z_1, Z_2, Z_3, Z_4, Z_5, Z_6), was randomly selected for each measurement from a uniform distribution that spanned +/- 10 % of the specific measurement value (actual chamber and double-layer impedance values are identical to those used for impedance estimation in Fig. 2.2). Error in the initial parameter guess was also added to each initial parameter guess value, and the amount of error added to every parameter value was randomly selected from a uniform distribution that spanned a given percentage (+/- %, y-axis) of the actual parameter value (like Fig. 2.3). TCPE was applied 50 times for each initial guess error level (+/- %, y-axis, see Methods) at specified ratios of Z_{c_real}/Z_{d_real} (x-axis, see Methods) after incorporating up to +/-10% noise in each simulated measurement. The coefficient of variation (CoV, σ/μ) associated with the average estimated double-layer (A) and chamber (B) impedance parameters for each ratio of Z_{c_real}/Z_{d_real} and at every 'error in the initial guess' level is shown here. Equivalent levels of CoV are indicated using contour lines (darker line color indicates larger CoV), and are slightly higher than those shown in the no measurement noise condition of Fig. 2.3.

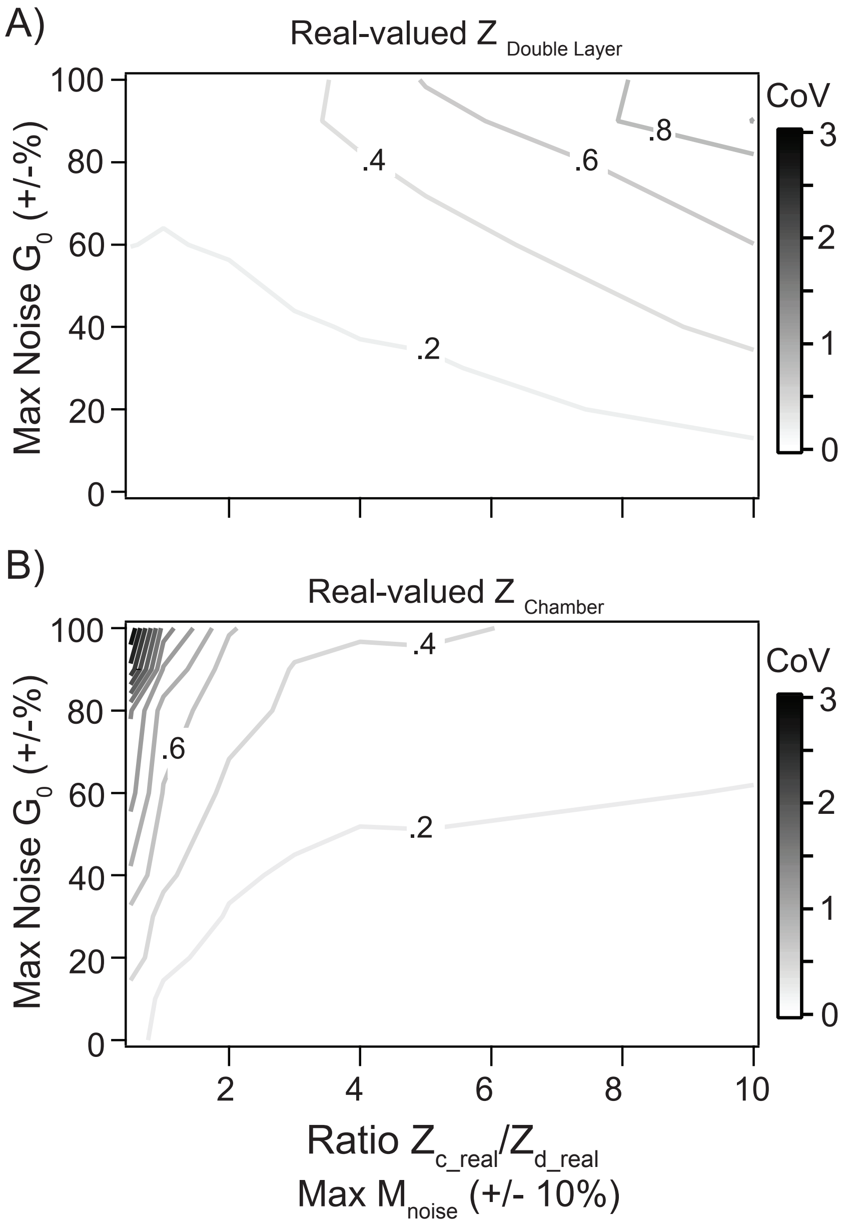
A)
Real-valued Z Double Layer
Max Noise G0 (+/-%)
100
80
60
40
20
0
.2
.4
.6
.8
CoV
3
2
1
0
B)
Real-valued Z Chamber
Max Noise G0 (+/-%)
100
80
60
40
20
0
.2
.4
.6
CoV
3
2
1
0
2
4
6
8
10
Ratio Zc_real/Zd_real
Max Mnoise (+/- 10%)

Fig. 2.5 – Measurement Noise and Individual Parameter Estimation – Exactly +10% (solid lines) or +20% (dotted lines) measurement noise was added to each of the six simulated equivalent impedances (Z_1, Z_2, Z_3, Z_4, Z_5, Z_6). Measurements were simulated using parameter values for Z_{d1_real} and Z_{c1_real} that were a given percentage less than (see x-axis, -% 'parameter spacing') Z_{d2_real} and $Z_{c2\_real,}$ while Z_{d3_real} and Z_{c3_real} were a given percentage more than (see x-axis, + % 'parameter spacing') Z_{d2_real} and Z_{c2_real} (Z_{d2_real} = 500 Ω and Z_{c2_real} = 2000 Ω). TCPE was used to estimate each parameter value at each parameter spacing level (x-axis) using noisy measurements, and parameter estimates were normalized to their assigned values (y-axis). Parameter value estimation accuracy was the same for each parameter when parameter values were equal, and differences in parameter values affected individual parameter estimation accuracy.

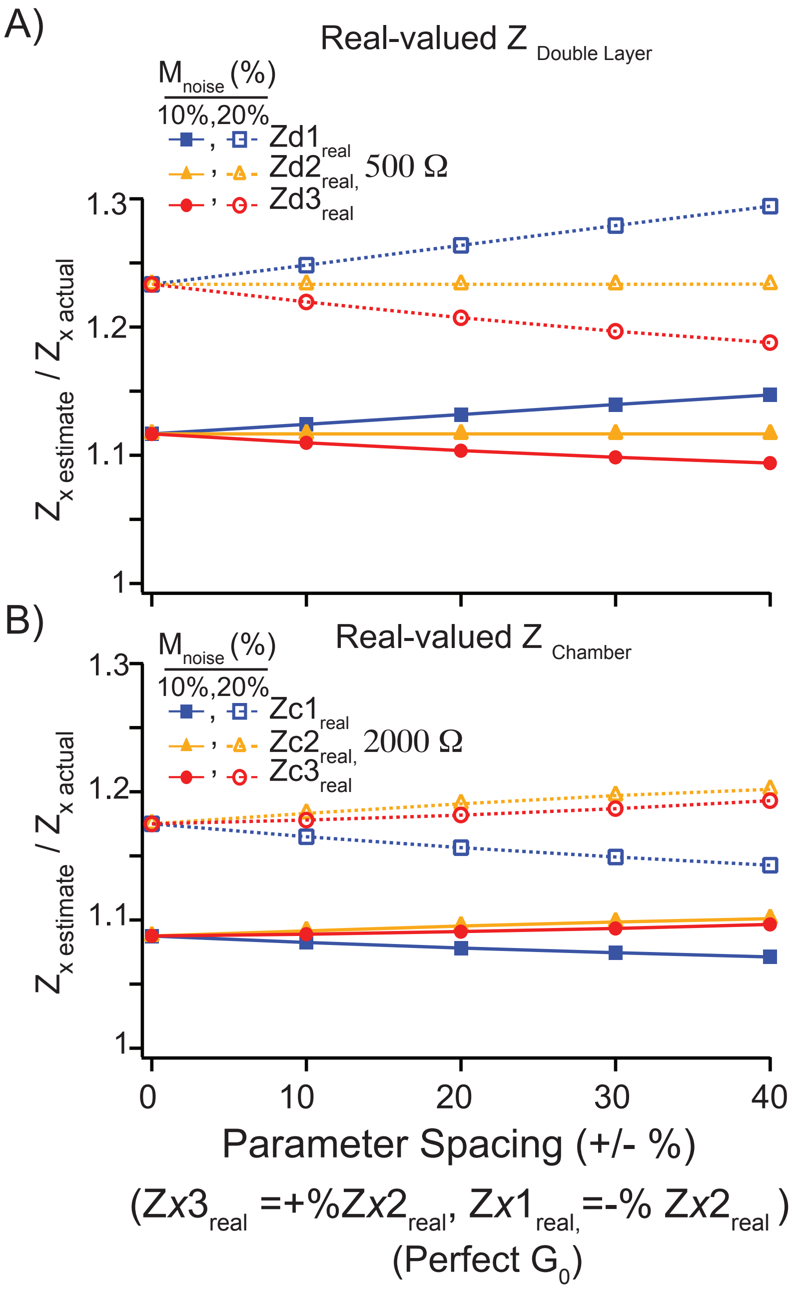
A)
Real-valued Z Double Layer
M noise (%)
10%,20%
Zd1 real
Zd2 real, 500 Ω
Zd3 real
1.3
1.2
1.1
1
Z x estimate / Z x actual
B)
Real-valued Z Chamber
M noise (%)
10%,20%
Zc1 real
Zc2 real, 2000 Ω
Zc3 real
1.3
1.2
1.1
1
Z x estimate / Z x actual
0
10
20
30
40
Parameter Spacing (+/- %)
(Zx3 real =+%Zx2 real, Zx1 real, =-% Zx2 real)
(Perfect G0)

Fig. 2.6 – Error in the Initial Guess and Individual Parameter Estimation –Noiseless simulated measurements (Z_1, Z_2, Z_3, Z_4, Z_5, Z_6) were calculated using values of Z_{d1_real} and Z_{c1_real} that were a given percentage less than (see x-axis, -% 'parameter spacing') Z_{d2_real} and Z_{c2_real}, and values of Z_{d3_real} and Z_{c3_real} were a given percentage greater than (see x-axis, +% 'parameter spacing') Z_{d2_real} and Z_{c2_real} ($Z_{d2\_real} = 500\ \Omega$ and $Z_{c2\_real} = 2000\ \Omega$). In these simulations, an exact percentage of error (+ 50% - solid lines, - 50% - dotted lines) was added to the initial guess of every parameter value before simulation. Individual parameter estimates were normalized to their assigned values (y-axis), and data for double layer impedances are shown in Fig. 2.6A while data for chamber impedances are shown in Fig. 2.6B. TCPE estimates every impedance value with equal accuracy when all of the parameter values are equal. However, parameter estimation accuracy is parameter value dependent, and parameter values linearly change with parameter spacing > 0 after the addition of a fixed initial guess error.

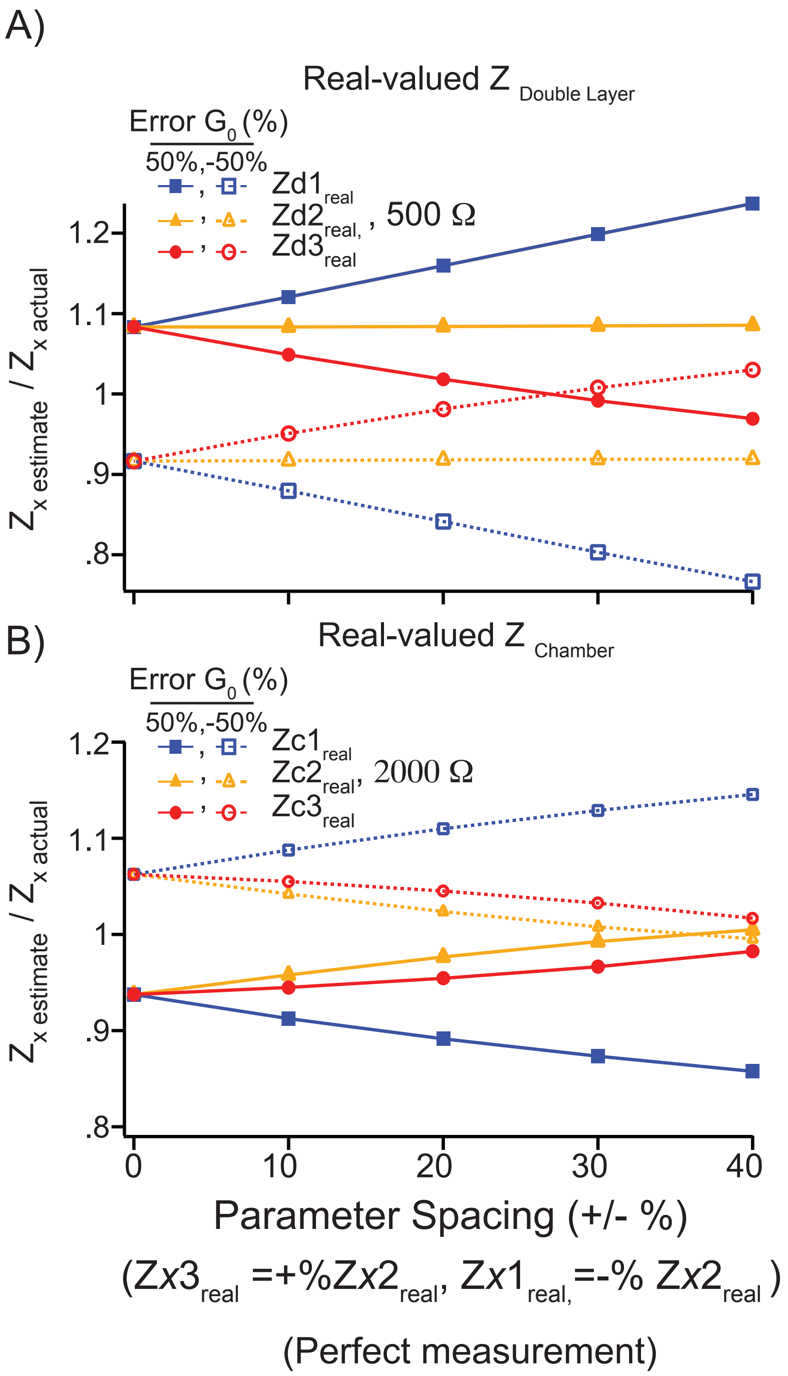
A)
Real-valued Z Double Layer
Error G0 (%)
50%,-50%
Zd1real
Zd2real, , 500 Ω
Zd3real
1.2
1.1
1
.9
.8
Zx estimate / Zx actual
B)
Real-valued Z Chamber
Error G0 (%)
50%,-50%
Zc1real
Zc2real, 2000 Ω
Zc3real
1.2
1.1
1
.9
.8
Zx estimate / Zx actual
0
10
20
30
40
Parameter Spacing (+/- %)
(Zx3real =+%Zx2real, Zx1real,=-% Zx2real)
(Perfect measurement)

Fig. 2.7 – Trial-averaged Parameter Estimation - Estimated predictions of the real components of Z_{c1}, Z_{c2}, Z_{c3}, Z_{d1}, Z_{d2} and Z_{d3} averaged together for multiple applications of TCPE. Noise, added to each set of six simulated measurements (Z_1, Z_2, Z_3, Z_4, Z_5, Z_6) in each application of TCPE, was randomly selected for each measurement from a uniform distribution that spanned +/- 10 % of each equivalent impedance value. Likewise, error in each initial parameter guess was randomly selected for every parameter from an interval that spanned +/- 100% of that parameter value. Actual chamber impedance values (Z_{c1} Z_{c2} Z_{c3}) were assigned values of (2000 Ω, -2000 Ω), while the values of Z_{d1}, Z_{d2} and Z_{d3} were determined by the ratios for Z_{c_real} /Z_{d_real} (Panel A - 8, Panel B - 4, Panel C -1, see Methods). Estimated values of Z_{c1_real}, $Z_{c2\text{-}real}$, $Z_{c3\text{-}real}$, $Z_{d1\text{-}real}$, $Z_{d2\text{-}real}$ and $Z_{d3\text{-}real}$, were normalized to the actual real-component of their respective impedance values (left y-axis, solid lines, solid markers). The gray bar indicates all parameter estimates that are within 10% of their actual impedance value. Standard errors of the mean (SEM) for the real component of every impedance value are also shown here (right y-axis , dotted lines and outlined markers).

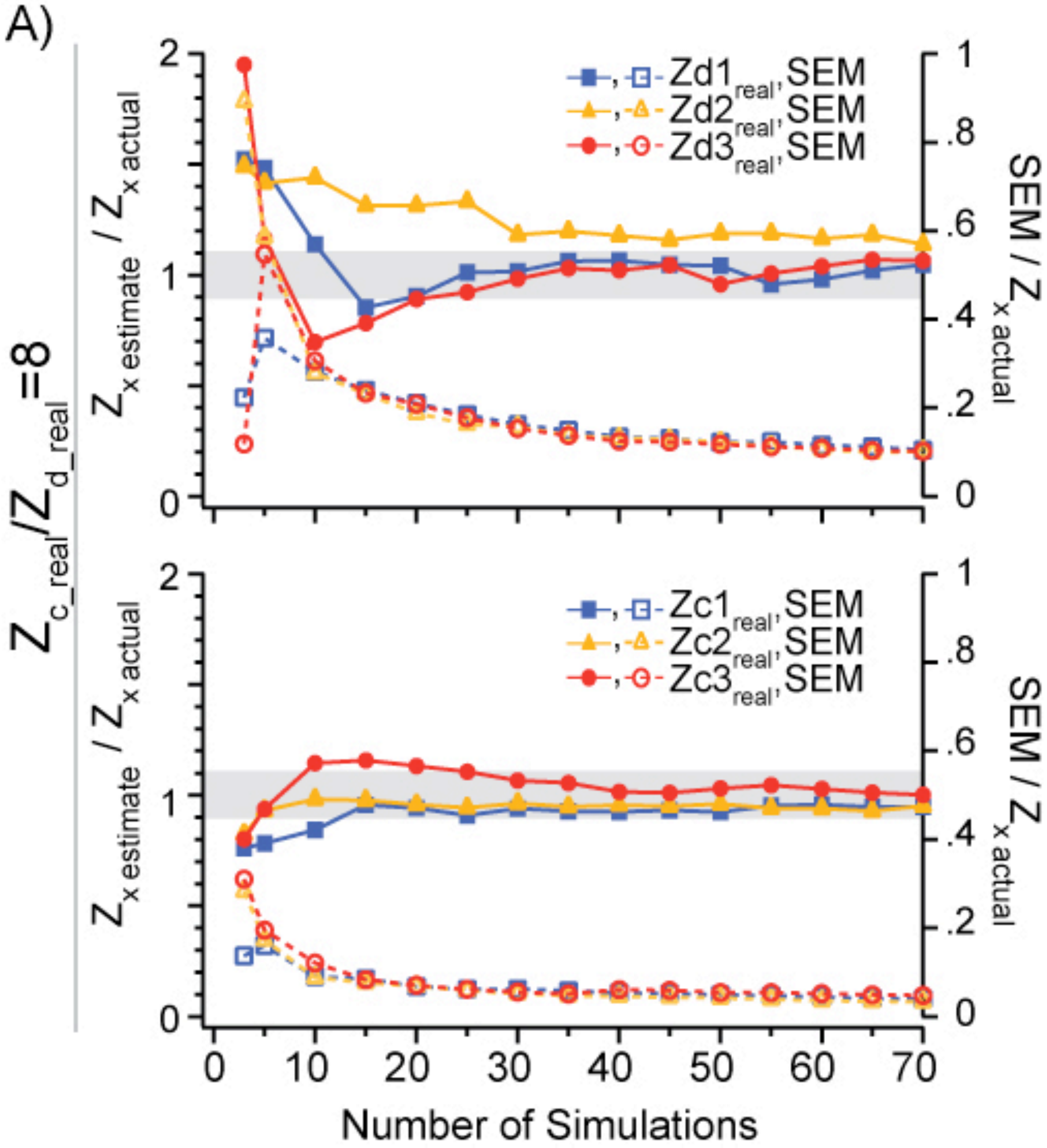
A)
Z_{c_real}/Z_{d_real}=8
$Z_{x\ estimate}$ / $Z_{x\ actual}$
SEM / $Z_{x\ actual}$
Zd1$_{real}$, SEM
Zd2$_{real}$, SEM
Zd3$_{real}$, SEM
Zc1$_{real}$, SEM
Zc2$_{real}$, SEM
Zc3$_{real}$, SEM
0
1
2
0
.2
.4
.6
.8
1
0
10
20
30
40
50
60
70
Number of Simulations

Fig. 2.7 – Part A.

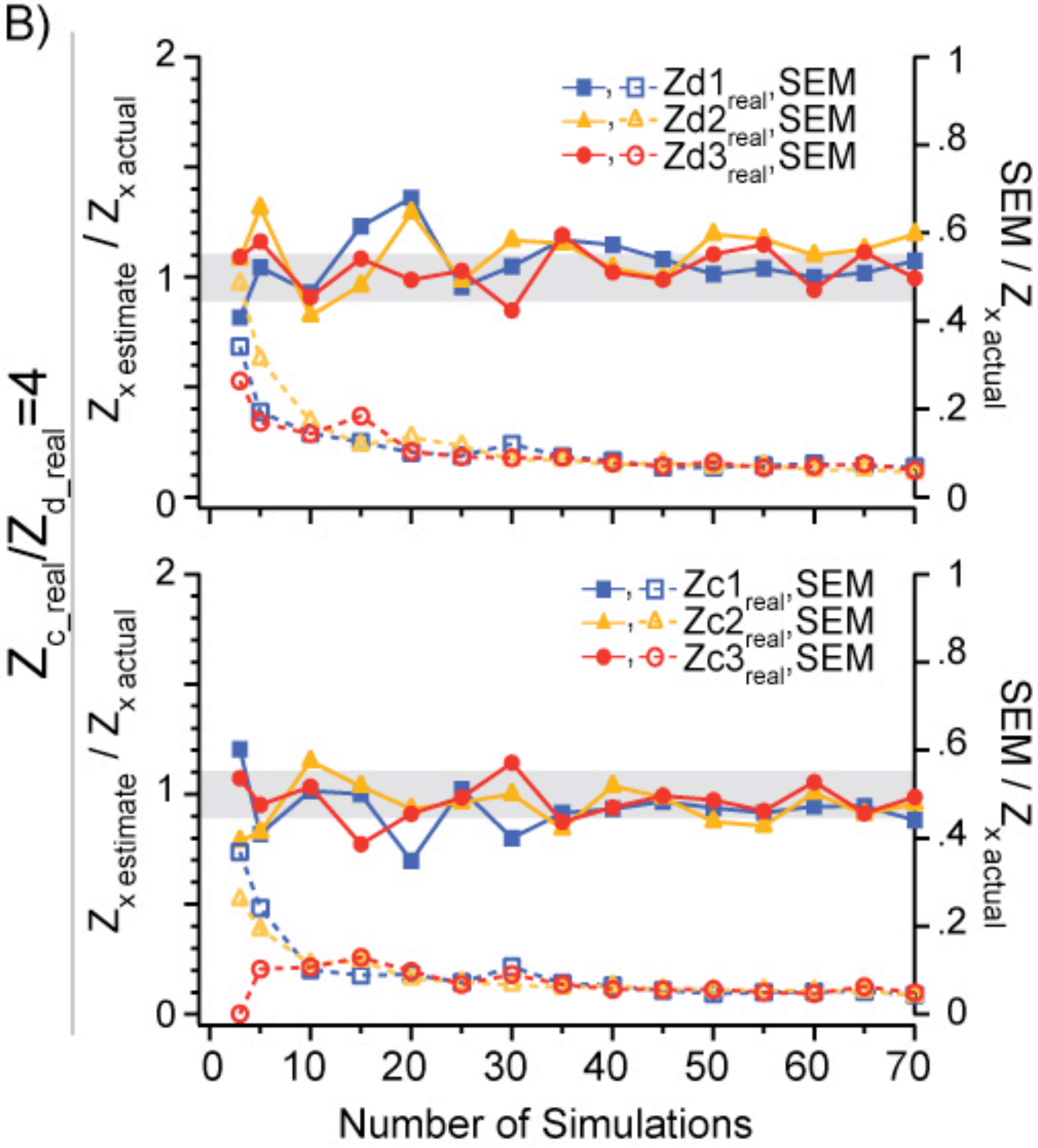
B)
$Z_{c\_real}/Z_{d\_real}=4$
Zd1real, SEM
Zd2real, SEM
Zd3real, SEM
Zc1real, SEM
Zc2real, SEM
Zc3real, SEM
Zx estimate / Zx actual
SEM / Zx actual
0
1
2
0
.2
.4
.6
.8
1
0
10
20
30
40
50
60
70
Number of Simulations

Fig. 2.7 – Part B.

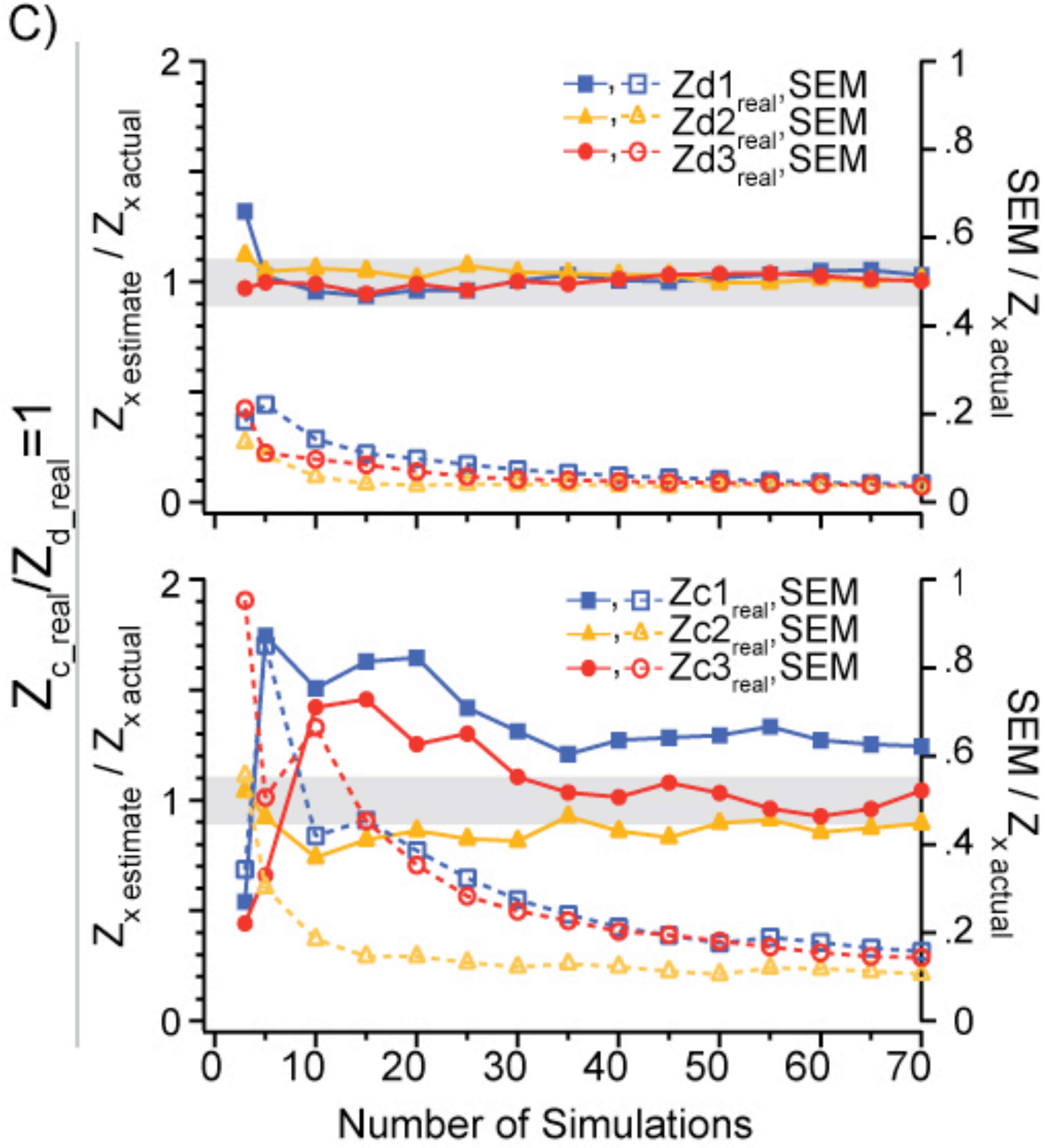
C)
$Z_{c\_real}/Z_{d\_real}=1$
Zd1real,SEM
Zd2real,SEM
Zd3real,SEM
Zc1real,SEM
Zc2real,SEM
Zc3real,SEM
$Z_{x\ estimate}/Z_{x\ actual}$
SEM / $Z_{x\ actual}$
0
1
2
0
.2
.4
.6
.8
1
0
10
20
30
40
50
60
70
Number of Simulations

Fig. 2.7 – Part C.

Fig. 2.8 – Parameter Estimation Sensitivity – Chamber and double-layer impedance components were assigned the following values (real and imaginary components are equal): Z_{c1}=.8*Z_{c2} (blue), Z_{c2}=2000 Ω (orange), Z_{c3} = 1.2*Z_{c2} (red), Z_{d1}=.8*Z_{d2} (blue), Z_{d2}=500 Ω (orange), Z_{d3} = 1.2*Z_{d2} (red). The ability of averaged TCPE parameter estimates to identify these parameter-value differences was examined. TCPE simulations assumed measurement noise values of up to +/- 10% and initial guess error values of up to +/- 100% (see Methods). The actual value of each parameter is denoted by the nonmarkered colored line (color corresponds to the appropriate double-layer (A) or chamber (B) impedance value). The lines with markers are indicative of the actual averaged impedance estimate, and error bars denote +/- 1 SEM. Statistical comparisons of the different pairs of real-valued impedance components ($Z_{c1\_real} – Z_{c2\_real}$, $Z_{c1\_real} – Z_{c3\_real}$, $Z_{c2\_real} – Z_{c3\_real}$, $Z_{d\_1real} – Z_{d\_2real}$, $Z_{d1\_real} – Z_{d3\_real}$, $Z_{d2\_real} – Z_{d3\_real}$) after 70 applications of TCPE indicate differences were significant between all impedance pairs except $Z_{d2\_real} – Z_{d3\_real}$ (p=.05).

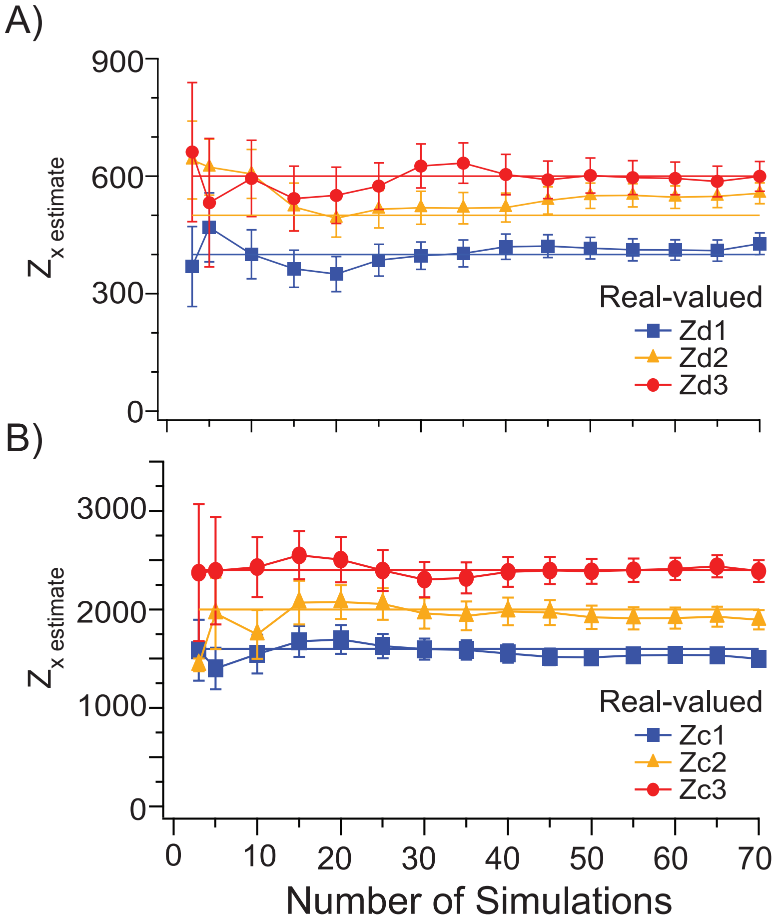
A)
900
600
300
0
Z_{x estimate}
Real-valued
Zd1
Zd2
Zd3
B)
3000
2000
1000
0
Z_{x estimate}
Real-valued
Zc1
Zc2
Zc3
0
10
20
30
40
50
60
70
Number of Simulations

CHAPTER 3

SINGLE-CELL ELECTRIC IMPEDANCE TOPOGRAPHY: MAPPING MEMBRANE CAPACITANCE [1]

Published: Sameera Dharia, Harold E. Ayliffe, Richard D. Rabbitt

LOC (2009), **9**: 3370-3377

3.1 Abstract

Single-cell electric impedance topography (sceTopo), a technique introduced here, maps the spatial distribution of capacitance (i.e. displacement current) associated with the membranes of isolated, living cells. Cells were positioned in the center of a circular recording chamber surrounded by eight electrodes. Electrodes were evenly distributed on the periphery of the recording chamber. Electric impedance measured between adjacent electrode pairs (10 kHz–5 MHz) was used to construct topographical maps of the spatial distribution of membrane capacitance. *Xenopus* oocytes were used as a model cell to develop sceTopo because these cells consist of two visually distinguishable hemispheres, each with distinct membrane composition and structure. Results showed significant differences in the imaginary component of the impedance between the two oocyte hemispheres. In addition, the same circumferential array was

---

[1] Reproduced by permission of The Royal Society of Chemistry, http://www.rsc.org. Article can be found at http://pubs.rsc.org/en/Content/ArticleLanding/2009/LC/b912881f.

used to map the size of the extracellular electrical shunt path around the cell, providing a means to estimate the location and shape of the cell in the recording chamber.

3.2 Introduction

Measurement of the electrical displacement current or capacitance of cell membranes provides a powerful means to examine key biological events such as synaptic transmission (Heidelberger *et al.*, 1994), ion-channel gating (Armstrong & Bezanilla, 1977b; Bezanilla, 2000b), cell division and growth (Huang *et al.*, 1999; Sohn *et al.*, 2000b; Wang *et al.*, 2002), protein-based electromotility (Santos-Sacchi, 1991) and membrane flexoelectricity (Petrov, 2002). Capacitance provides information about cell size and structure resulting from lipid bilayer surface area, ultrastructure and molecular composition (Pethig, 1979; Foster & Schwan, 1989; Lo *et al.*, 1995; Polk & Postow, 1996; Gritsch *et al.*, 1998). Techniques to measure membrane capacitance, therefore, have significant applications in basic science and can also be used to screen candidate pharmaceutical compounds (Ratanachoo *et al.*, 2002) and genetic manipulations for therapeutic efficacy.

Here we introduce a new technique, single-cell electric impedance topography (sceTopo), that measures the spatial distribution of membrane[2,3] capacitance around isolated living cells using radio frequency interrogation. The recording system resembles that used in electric impedance tomography (EIT), where current/voltage measurements made by an array of electrodes around the human body are used to generate two- or three-

---

[2] The term "membrane" used herein refers to the multiple layers of lipids, proteins and sugars on the periphery of the cell.

[3] Since the time of publication, the term "membrane" has been revised to mean multiple layers of lipids and proteins on the periphery of the cell.

dimensional (2D or 3D) electrical images of the bodies interior (Webster, 1990b; Brown, 2003a; Brayford, 2006). In the present study, electrode arrays were miniaturized to record electrical impedance values around an isolated, single cell. The method differs from EIT, however, in that it is used to probe the electrical properties of a material near the electrode's surface (in this case, the cell membrane and the extracellular solution) and is not well suited to image the interior of cells[4]. Hence, the present method is referred to as single-cell electric impedance topography (rather than tomography).

In sceTopo, isolated cells were positioned within a recording chamber that was surrounded by an array of conducting electrodes. The conducting tips of the electrodes were equally spaced around the periphery of a circular recording chamber with the insulated shanks of the electrodes directed radially. Local electrical properties of the membrane were examined by recording the impedance between adjacent pairs of extracellular electrodes at radiofrequencies, a method based in electric impedance spectroscopy (Hoffman & Britt, 1979; Pethig, 1979; Schwartz *et al.*, 1983; Coulter & Rodriguez, 1988; Ayliffe *et al.*, 1999; Gawad *et al.*, 2001; Gawad *et al.*, 2004; Werdich *et al.*, 2004; Rabbitt *et al.*, 2005; Han & Frazier, 2006). The recording chamber was sized to minimize the distance between the electrodes and the plasma membrane in order to maximize interaction between the electric field and the plasma membrane. Data were used to construct topographical maps showing the spatial distribution of membrane electrical properties. The system was designed/fabricated for use on a microscope stage and facilitated application of chemical solutions, microinjections or electrophysiological recordings during sceTopo.

---

[4] A clarification of the published manuscript: The algorithm used here is designed specifically to monitor changes near the electrode-electrolyte interface. An inverse algorithm could be applied (with a higher interrogation frequency) to monitor intracellular organelle distribution.

Xenopus oocytes (frog eggs) were used as the model cell to develop sceTopo because of their large size (~1 mm diameter), ease of manipulation, availability and polarized structure. These cells are a common model for electrophysiological studies because their size facilitates two-electrode voltage clamp and because they can express exogenous proteins (including ion channels) in their membrane (Dascal, 1987; Swanson & Folander, 1992; Stuhmer, 1998; Weber, 1999). Oocytes have two distinct hemispheres or poles, the animal pole characterized by its dark brown color and the vegetal pole characterized by its yellow color. The types of ion channels, organelles, melanin concentration and microvilli vary as a function of oocyte hemisphere. This endogenous polarization makes the oocyte a natural choice to test the ability of sceTopo to resolve spatial inhomogenity of membrane properties.

Results shown here specifically demonstrate the ability of sceTopo to resolve spatial differences in electrical impedance around native *Xenopus* oocyte membranes. Results also show, using phantoms (i.e. objects with known electrical properties), that the shape and location of the cell within the chamber can be estimated.

3.3 System Design and Fabrication

3.3.1 Electrode Array Fabrication

Electrode arrays were constructed using a combination of thick-film, microfabrication and xurographic techniques (Bartholomeusz *et al.*, 2005). A knife-plotter (Graphtec 7000 , Graphtec America, Santa Ana, CA) was used to pattern a circularly distributed set of 8 electrodes into the top layer of the double-layered Rubylith polymer (Rubylith RU3, Ulano Corp., New York City, NY). The top layer of the patterned Rubylith served as a mask during metal deposition. A 1.1–1.2 mm diameter hole was also cut in the center of the electrodes through both layers of the Rubylith polymer and acted as a recording chamber. Platinum and titanium (seed layer) were sputtered on the patterned Rubylith (TMV SS-40C-IV, T-M Vacuum Products, Cinnaminson, NJ) at the University of Utah's Microfabrication Laboratory. The mask layer of the Rubylith was lifted off to reveal the electrode array. Electrodes were plated using a current density of 10 mA/cm^2 in a platinum black plating solution (3.3% (by weight) chloroplatinic acid and .03% (by weight) lead acetate). Platinization increased electrode surface area, thereby decreasing electrode double-layer impedance. The electrodes were individually isolated using a Kapton polyimide adhesive (5314 Kapton, 3M, St. Paul, MN) (Fig. 3.1B). The volume above the triangular portion of each electrode was filled with either physiological saline (phantom experiments) or Superbarths oocyte media (88 mM NaCl, 1 mM KCl, 0.41 mM $CaCl_2$, 0.33 mM $Ca(NO_3)_2$, 1 mM $MgSO_4$, 2.4 mM $NaHCO_3$, 10 mM HEPES, 1 mM pyruvate and 50 μg/ml gentamicin, titrated using NaOH to a pH of 7.4). This geometry increased the electrode surface area contacting the media and further lowered the double-layer impedance of the Pt electrodes. Electrical bond pads, located near the periphery of each electrode array, connected the electrode array to a printed circuit board (PCB) (Fig. 3.1C). The PCB was interfaced with electronic instrumentation described below.

3.3.2 Platform

The electrode array was clamped in a polycarbonate interface that allowed for cell loading and positioning (via a vacuum port) into the recording chamber (Fig. 3.1C). The bond pads on the electrode array contacted the PCB through a series of spring-loaded gold pins (B1363-D4 Interface Contacts, Rika Denshi, Attlebro, MA) (Fig. 3.1C). The electrical source consisted of either the Tektronix AFG320 or AWG430 (Tektronix, Beaverton, OR). Each source was individually calibrated using a Thévenin equivalent model to compensate for load-dependent loss at frequencies greater than 100 kHz. A voltage-dividing on-board reference impedance was used to calculate recording-chamber impedance (Ayliffe *et al.*, 1999; Han & Frazier, 2006; Dittami *et al.*, 2008). High-impedance voltage-follower operational amplifiers (OPA356, Texas Instruments, Dallas, TX) located on the headstage PCB were used to sample the voltage drop across the reference impedance to determine current. All signals were recorded in quadrature by lock-in amplification (Stanford Research, SR830 SR844, Sunnyvale, CA). Electrodes on the array were individually addressable, and the interrogating signal was directed to the electrode of interest using digital switches (Max4521, Maxim Integrated Products, Sunnyvale, CA) located on the custom headstage PCB (Fig. 3.1D). Source output, signal recording and electrode pair selection were automatically controlled via a custom computer interface (IGOR Pro, WaveMetrics, Portland, OR). The program remotely controlled the waveform generator and lock-in amplifier recording (GPIB, National Instruments IEEE 488). Analog voltage sampling and digital switching were controlled via 16-bit analog–digital converters and digital outputs (ITC 1600, HEKA Inst., Bellmore, NY).

3.4 Theory

3.4.1 Simulations

A qualitative 2D finite-element model of the oocyte-loaded microchamber was developed to gain insight into the nature of electric fringe fields and to guide interpretation of results. We modeled the cell membrane as a highly resistive linear dielectric ($\sigma = 3.14*10^{-9}$ S/m, $\varepsilon = 90$ F/m, thickness = 20 nm),[5] the cytoplasm as a simple ionic conductor ($\sigma = 1.4$ S/m) and the extracellular space as a conductor ($\sigma = 1.4$ S/m, thickness = 2 μm) (Barnes, 2006). The 2D Maxwell equations were solved in the frequency domain (Comsol Multiphysics, Los Angeles, CA). Sinusoidal voltage stimuli were applied in the model across adjacent pairs of electrodes to simulate electric fringe-field interaction with the cell membrane in the recording chamber. The electrode–electrolyte interface impedance was not included in the model and finite-element simulations pertain only to the impedance associated with the cell and extracellular shunt pathway. A lumped-parameter model (Fig. 3.2) — including the electrode–electrolyte double layer, the conductive shunt extracellular pathway, the plasma membrane and the intracellular impedance — was also used to facilitate interpretation of results.

---

[5] A clarification of the published manuscript: The simulations performed here use parameters that are specific for a *Xenopus* oocyte. Double-layer and the fibrous vitelline membrane that surround the oocyte (highly conductive) were not included in these qualitative simulations, which were primarily intended to provide a better understanding of RF signal interaction with the oocyte lipid bilayer.

3.5 Experimental

3.5.1 Measurements from Passive Cells and Phantoms

Xenopus oocytes were chosen as the model cell to develop and test the sceTopo approach. Oocytes are visibly polarized into brown (animal) and white (vegetal) hemispheres, are large in size (1.2 mm in diameter) and have inhomogenous membrane-bound protein/channel expression between the animal vs. vegetal hemispheres (Robinson, 1979; Dascal, 1987; Gomez-Hernandez *et al.*, 1997; Chang *et al.*, 1999; Weber, 1999). Differences between the animal and vegetal hemispheres, thought to help in guiding oocyte development, also provide a polarized, easily visualizable, cellular structure ideal for testing the sceTopo platform (Robinson, 1979; Dascal, 1987; Gomez-Hernandez *et al.*, 1997; Chang *et al.*, 1999; Weber, 1999). It was hypothesized that the imaginary component of the impedance associated with a resting oocyte would differ between the two hemispheres and would be detectable using sceTopo. Oocytes (defolliculated) and phantoms were individually placed in the recording chamber using micropipettes, and impedance measurements between adjacent pairs of electrodes were made around the cell. Data were collected in quadrature with a lock-in filter of 18 dB/octave and a lock-in integration time of 3 ms (SR844, Stanford Research, CA). Results were corrected using a Thévenin source calibration and combined with an on-board reference impedance to obtain complex-valued impedance measurements between adjacent pairs of electrodes. Lock-in amplifier analog outputs were sampled in quadrature at 1 kHz (ITC 1600, InstruTECH, Bellmore, NY). To estimate the contribution of the electrode–electrolyte double-layer impedance, data were also collected under the same stimulus conditions when the chamber was only filled with extracellular media (media-only condition) during each experiment. Since the impedance in the media-only condition was low relative to the tight-fitting cell-loaded condition, subtracting the media-only data from the cell-loaded data removed major contributions of the double-layer impedance from the cell/phantom measurements (Ayliffe *et al.*, 1999). One caveat of this approach is that it also subtracts the electrical resistance of the media itself, and therefore, the real component of the impedance obtained is shifted by a real-valued constant.

After subtracting the double-layer, the impedance measured between adjacent electrode pairs was divided in half and assigned to chamber positions that corresponded to the center point directly in front of each interrogating electrode. This was done for every electrode-pair measurement, and the values associated with each electrode position were averaged together. The procedure resulted in impedance data for 8 locations around the circumference of the cell, corresponding to the 8 electrode positions in the circular array. Impedance data were interpolated between electrodes and smoothed using a five-term Fourier series in the form $Z(\vartheta)=\sum_{n=0}^{5}\left(A_n Cos(\vartheta-\vartheta_0)+B_n Sin(\vartheta-\vartheta_0)\right)$. A_n and B_n, calculated from the data using a least squares regression, are complex-valued Fourier coefficients. Z is the interpolated impedance as a function of polar angle ϑ.

Polar impedance plots were constructed for both toroidal glass washers (phantoms, 1 ± 0.1 mm diameter about its radially symmetric axis, 0.61 ± 0.06 mm thick, 0.44 ± 0.06 mm dia. hole; purchased as seed beads from the Garden of Beaden, Upland, CA) and for single cells (oocytes). The second moment of area and the centroid of $Z(\vartheta)$ were also computed as metrics of the shape and orientation of the phantom. Impedance plots for each phantom were first constructed using $\vartheta_0 = 0$, and subsequently rotated by angle ϑ_0 to align the phantom major axis with the horizontal. The major axis was identified using a photomicrograph of the phantom in the chamber. These rotated results were then averaged across phantoms. Means and standard errors were plotted as a function angle ϑ. Unpaired, Student's t-tests were used to compare the major and minor axis lengths of the toroidal glass phantoms. Unpaired, Student's t-tests were also used to compare difference in angular position (the angle between the major axes of the phantom to the 0°–180° axes) of the phantoms in their photomicrographs to the impedance-based phantom representations.

At high frequencies, the capacitive shunt impedance of the electronic head-stage board and cabling was significant. At the frequencies used (< 5 MHz), the glass phantoms can be considered nearly perfect insulators. This allowed us to find a correction factor to account for the additional capacitive shunt loss at 1 MHz by comparison to results obtained at 10 kHz. The correction factor was applied to subsequent oocyte data collected using the same array, since the capacitive shunt would be nearly the same in the two cases.

The procedure to measure $Z(\vartheta)$ described above for phantoms was also used for cells. Cells were positioned in the channel using very small amounts of negative pressure (applied through a vacuum port, see Fig. 3.1D), so as to minimize any membrane distortion during cell loading. Pressure release and application resulted in coarse manipulation of cell position in the recording chamber, and a constant negative pressure was used to hold the oocytes in place after the meridian of each oocyte was centrally aligned in the electrode array. For each oocyte, a photomicrograph taken during sceTopo interrogation was used to rotate the data by an angle ϑ_0 (see Fourier series above) so that the meridian separating the animal and vegetal hemispheres for a particular cell was aligned with the horizontal. This allowed for alignment of the gross morphology of different oocytes and comparisons across cells. Real and imaginary components of *Z* were plotted in polar form to map the impedance as a function of position around the circular electrode array. Means and standard errors were determined across multiple cells, thus providing confidence intervals as functions of angular position around the cell. Unpaired Student's t-tests were used to compare spatial differences between the two hemispheres of the oocyte.

3.6 Results and Discussion

3.6.1 Simulations

Figure 3 illustrates the results of a 2D finite-element model for pairwise fringe-field electrical interrogation at three frequencies: A) 50 kHz, B) 500 kHz and C) 5 MHz. Voltage magnitudes are shown as shades of gray ranging from maximum (white) to minimum (black). At low frequencies (A) where conduction current dominates, virtually all of the current is shunted in the extracellular space between the two interrogating electrodes. This occurs because the resistance of the plasma membrane is much greater than the surrounding media. While low-frequency fringe-field data is not useful in elucidating information about the membrane, intracellular organelles or proteins, it does provide information about extracellular shunt path size and therefore can be used to estimate the shape of a cell in the sceTopo recording chamber (see Phantom Data results). As interrogation frequency increases, current is divided between displacement current in the membrane and conduction current in the extracellular shunt path (B). The amount of current displaced across the membrane in this midfrequency range can be used to estimate the effective capacitance of the membrane. At high frequencies (C), displacement current across the membrane dominates; the membrane effectively becomes transparent to the applied radio-frequency signals and more current is transmitted to the intracellular space. These simulations are not intended to be quantitatively accurate since the electrode–electrolyte double-layer impedance was not included, thereby shifting the magnitude and phase of the electrode voltage relative to that shown. Furthermore, the simulations are two-dimensional and cannot accurately capture out-of-plane current paths. Nevertheless, the simulations do illustrate the concept of measuring electric impedance between adjacent electrodes to 1) estimate the shape of the cell, 2) measure the effective dielectric properties of the membrane and 3) possibly detect or measure effects of nearby intracellular organelle(s). As with the lumped parameter model illustrated in Fig. 3.2, finite-element simulations show that the size of the extracellular shunt path is the primary experimental parameter that must be minimized to enable measurement of displacement currents in the membrane at the low-to-mid radio frequency range of interrogation. If the extracellular shunt path is too large, the corner frequency can quickly exceed 5 MHz, thus limiting the practical utility of the approach for membrane interrogation. It is therefore advantageous to size the system so cells fit snugly within the chamber and are in close vicinity to the interrogating electrodes.

3.6.2 Phantom Data – Mapping Cell Shape via the Extracellular Conductance

Due to their low conductivity and permittivity, glass phantoms acted as nearly perfect insulators relative to the extracellular media. Therefore, virtually all of the current was conducted in the space around the phantom. This made the phantoms useful to demonstrate the utility of sceTopo in cell/object shape estimation.

Photomicrographs of the phantoms in the array are shown in the left column of Fig. 3.4 and impedance maps are shown for the same phantoms in the right column. The electrodes are outlined in solid white (numbered 1–8) , and the recording chamber is outlined in a dotted white line. The impedance magnitude at each electrode position (after subtraction of the double layer) is plotted in polar form to generate the maps in the right column (see Methods, section 3.5). Notice the correspondence between the physical shape of the phantom (left) and the electrical map of the shunt conductance (right). The centroid of the impedance data (right, square symbol at intersection of dotted lines) provides the electrical center of the phantom, and the principle directions of the second moment of area tensor provide the orientations of the major and minor axes of the phantom (dotted lines). The electrical center and orientation (right) showed good qualitative comparison to the photomicrographs of the phantoms (left), and no significant difference was measured when comparing the angular position (the angle between the major axes of the phantom to the 0°–180° axes) of the phantoms in the photomicrographs to the impedance-based phantom representations (p=.95, n=4). Data were not used in the statistical comparison if the inner annulus of the phantom was visible in the photomicrograph. Since the phantoms were highly resistive relative to saline and fit loosely within the chamber, the interrogating currents were shunted in the space around the phantoms and the electrical impedance data reflected the magnitude of this shunt. Phantoms positioned more closely to the electrodes resulted in qualitatively more accurate representations of phantom shape.

Data from individual phantoms were then compared to examine repeatability of impedance maps (*n* = 9). To avoid any systematic errors associated with the array, phantoms were placed with random angular orientation in the recording chamber and the Fourier series representations produced by the data were subsequently rotated to the configuration depicted in Fig. 3.5A (see Methods). Since the phantoms fit loosely in the chamber, impedance data were dominated by conduction current in the saline. The corner frequency where displacement currents in the phantom became significant was well beyond the 5 MHz limit of present experiments. Results mapping the magnitude of the impedance (normalized) as a function of angular position around the array are provided in Fig. 3.5B for data collected at 1 MHz (blue, long dashes, short error bar caps) and 10 kHz (red, short dashes, long error bar caps). Error bars and shaded bands show one standard error of the mean and are plotted around the averaged 10 kHz (longer error bar ends, pink color band) and 1 MHz (shorter error bar ends, blue color band) data. Differences in extracellular shunt path length along the major vs. minor axes were statistically significant (*p* = 0.00014 for the 10 kHz data set). The major conclusion from data shown in Fig. 3.4 and Fig. 3.5 is that sceTopo can map the gross shape of an insulating object by measuring spatial variations in the electrical shunt resistance around the outside of the object.

3.6.3 Mapping Membrane Charge Displacement

Xenopus oocytes were randomly placed in the recording chamber. Cells fit snugly in the array with the electrodes separated from the plasma membrane by only a thin layer of oocyte media (Superbarths). This tight fit reduced the extracellular shunt pathway and placed the electrical corner frequency of fringe-field interrogation near 100 kHz. Above this corner frequency, displacement currents in the membrane became clearly observable in the data. Below this corner frequency, the impedance was dominated by the extracellular shunt. Thus, comparison of measured impedance differences between high and low frequencies of interrogation allows for a description of cell electrical properties that accounts for cell location/morphology in the recording chamber. After interrogation, impedance maps ($n = 8$) were rotated using photomicrographs of each cell, such that oocyte meridians were aligned with the horizontal axis (see Fig. 3.6A, horizontal axis stretched from 0°–180°) to compare data across cells (see Methods). Impedance results at 10 kHz (pink, small dashes, long error bar caps) and 1 MHz (blue, long dashes, short error bar caps) are shown in the form of real (Fig. 3.6B: Re(Z)) and imaginary (Fig. 3.6C: Im(Z)) components after double-layer subtraction and unit circle normalization. The real-valued impedance map (Fig. 3.6B) showed no significant difference between the 10 kHz and 1 MHz interrogation as a function of oocyte hemisphere ($p = 0.33$). This was expected since the real component of the impedance is dominated by the extracellular shunt conductance at these interrogation frequencies and is not very sensitive to the properties of the oocyte membrane. In contrast, the imaginary component of the impedance showed a significant ($p = 0.0058$) difference between the 10 kHz and 1 MHz data when comparing the vegetal (0°–180°) and animal (180°–360°) hemispheres of an oocyte (the oocyte meridian is horizontal, the white vegetal pole is at 90° and the brown animal pole is at 270°). There was very little difference in the imaginary component between the two frequencies on the animal pole of the cell (270°), but a much larger difference on the vegetal pole of the cell (90°).

The imaginary component is dominated by the displacement current in the membrane and includes capacitance contributions from the passive permittivity of the lipid membrane, mobile charges associated with membrane-bound proteins and excitable contributions associated with voltage-gated ion channel kinetics. Known compositional differences between the animal and vegetal hemispheres of an oocyte include, but are not limited to, concentrations of calcium-activated chloride channels, microvilli ultrastructure, yolk platelets (cholesterol granules) and melanin granules (Dascal, 1987; Gomez-Hernandez *et al.*, 1997; Chang *et al.*, 1999; Weber, 1999). The effective dielectric properties associated with these differences presumably underlie the asymmetry in the imaginary-valued impedance observed between the two hemispheres reported here (Fig. 3.6C). We did not explore which of these potential factors was responsible for the difference, but it is hypothesized that differences in membrane(s) ultrastructure contributed significantly to differences in capacitance measured between the two hemispheres. Future studies could use pharmacological agents to disrupt microvilli ultrastructure or bind ion channels to explore hypothetical contributions of these components to the effective dielectric properties of an oocyte membrane.

3.7 Conclusion

Results show that sceTopo can effectively be applied to map 1) cell shape and position in the recording chamber and 2) the endogenous spatial distribution of membrane capacitance around a single cell. The two-dimensional maps reported here provide images around the meridian of a *Xenopus* oocyte. Spatial resolution is directly dependent on the number of electrodes around the cell in the recording chamber (currently, ~ 1/8 cellular circumference). This could be increased, however, by incorporating additional electrodes in the array. Incorporating a pressure control system to precisely position cells and a perfusion system to facilitate exchange of solutions and pharmacological agents would also improve the system.

Furthermore, it is feasible that the sceTopo approach could extend to three dimensions (3D) and that the array could be downsized for smaller cells. Both of these aims are within the scope of current technology. Known thick film laminate technologies, based on heat and pressure sensitive films, allow for the simple stacking of individual electrode array layers and should result in a straightforward 3D array structure (Paul & Peterson, 1999; Han *et al.*, 2003a; Han *et al.*, 2003b; Goettsche *et al.*, 2007; Moss *et al.*, 2007). The large size of *Xenopus* oocytes allowed the use of simple electrode fabrication techniques, but technology is already available to fabricate micron-sized metal electrodes that surround 10 μm diameter cells (Ayliffe *et al.*, 1999; Werdich *et al.*, 2004; Dittami *et al.*, 2008). Furthermore, electron-beam and ion-beam lithography have been used to construct nanometer-sized electrodes that can analyze DNA sequences and detect glucose containing analytes (Giordano *et al.*, 2001; Gierhart, 2008). Similar fabrication techniques could potentially be applied to the sceTopo platform to allow for micron-sized cell interrogation with nanometer scale resolution.

Lastly, it is also possible that this approach could offer an alternative means to study the fast kinetics of charged, excitable, membrane-bound proteins in oocytes themselves. Oocytes can express high concentrations of exogenous proteins in their membranes and are commonly used to study the kinetics associated with single proteins. As such, the sceTopo platform can be used to interrogate electrically excited oocytes expressing exogenous, voltage-sensitive, membrane-bound proteins. The high interrogation frequencies of the sceTopo system should time-resolve changes in charged protein conformation during cellular excitation, and these differences should manifest as measurable differences in effective capacitance. If true, sceTopo might offer a new window to observe excitable integral membrane protein dynamics.

3.8 Acknowledgements

Financial support was provided by the NIH (NIDCD R01-DC004928) and the NSF (IGERT DGE-9987616). Andras Pungor provided electronic design, Michael Sanguinetti provided *Xenopus* oocytes, Rebecca Airmet edited the manuscript and Curtis King assisted in the design and fabrication of the microfluidic devices and interface.

Fig 3.1 – Experimental Setup - A) Platinum was patterned onto a polyester substrate, and the electrodes near the recording chamber were plated with platinum black. B) Insulated, electrode array. C) A polycarbonate interface (C-i) allowed for positioning of the electrode array (C-ii) such that spring-loaded gold pins (C-iii) connected the bond pads on the electrode array to bond pads (C-iv) on a printed circuit board (PCB, C-v). Inset shows the multiple layers of the electrode array (a polyester base (ii_1), recessed platinum-black coated electrodes (ii_2) and insulating Kapton tape (ii_3)). D) PCB and fluidic interface positioned on the stage of an upright microscope showing the headstage amplifiers (D-i), computer controlled digital switches (D-ii) and vacuum-port (D-iii).

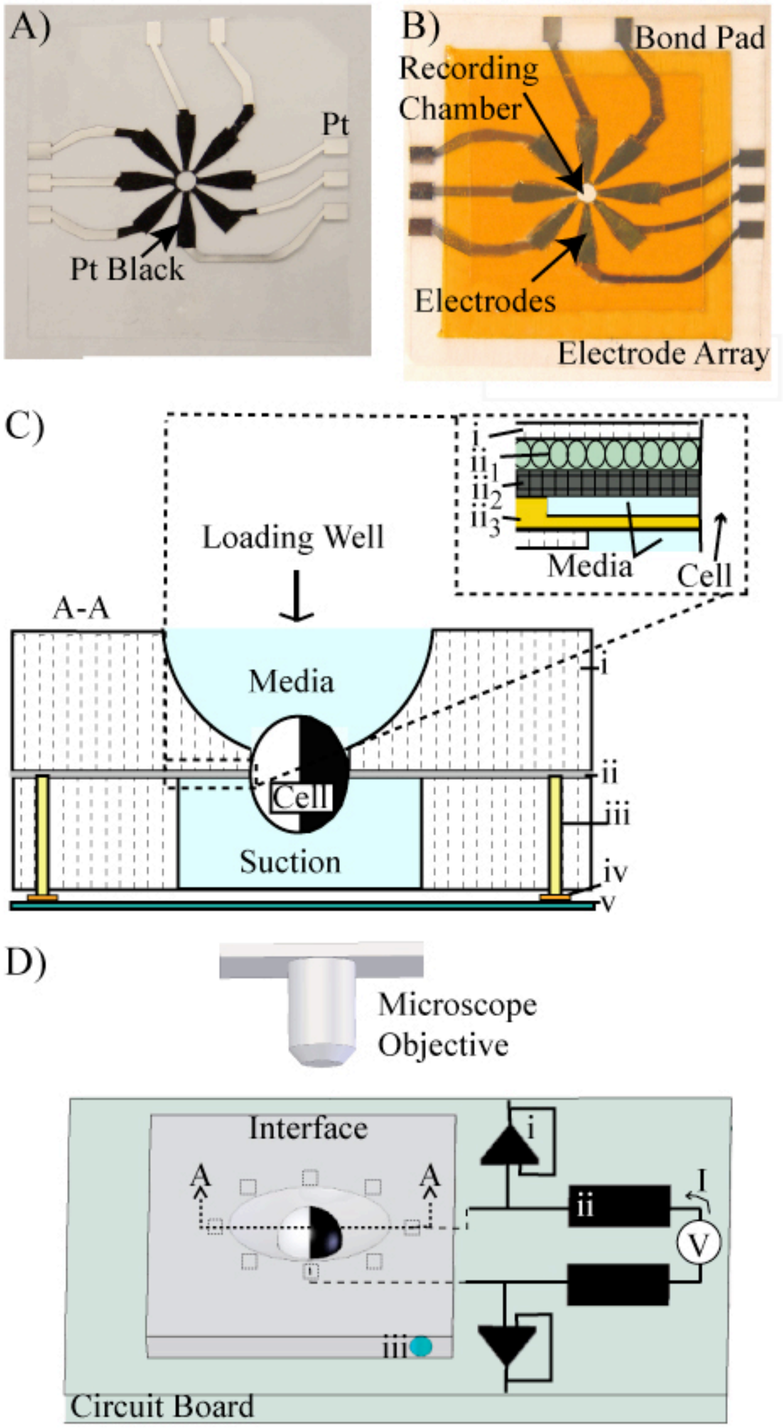
A)
Pt
Pt Black
B)
Bond Pad
Recording
Chamber
Electrodes
Electrode Array
C)
Loading Well
i
ii1
ii2
ii3
Media
Cell
A-A
Media
i
ii
Cell
iii
Suction
iv
v
D)
Microscope
Objective
Interface
A
A
i
ii
I
V
iii
Circuit Board

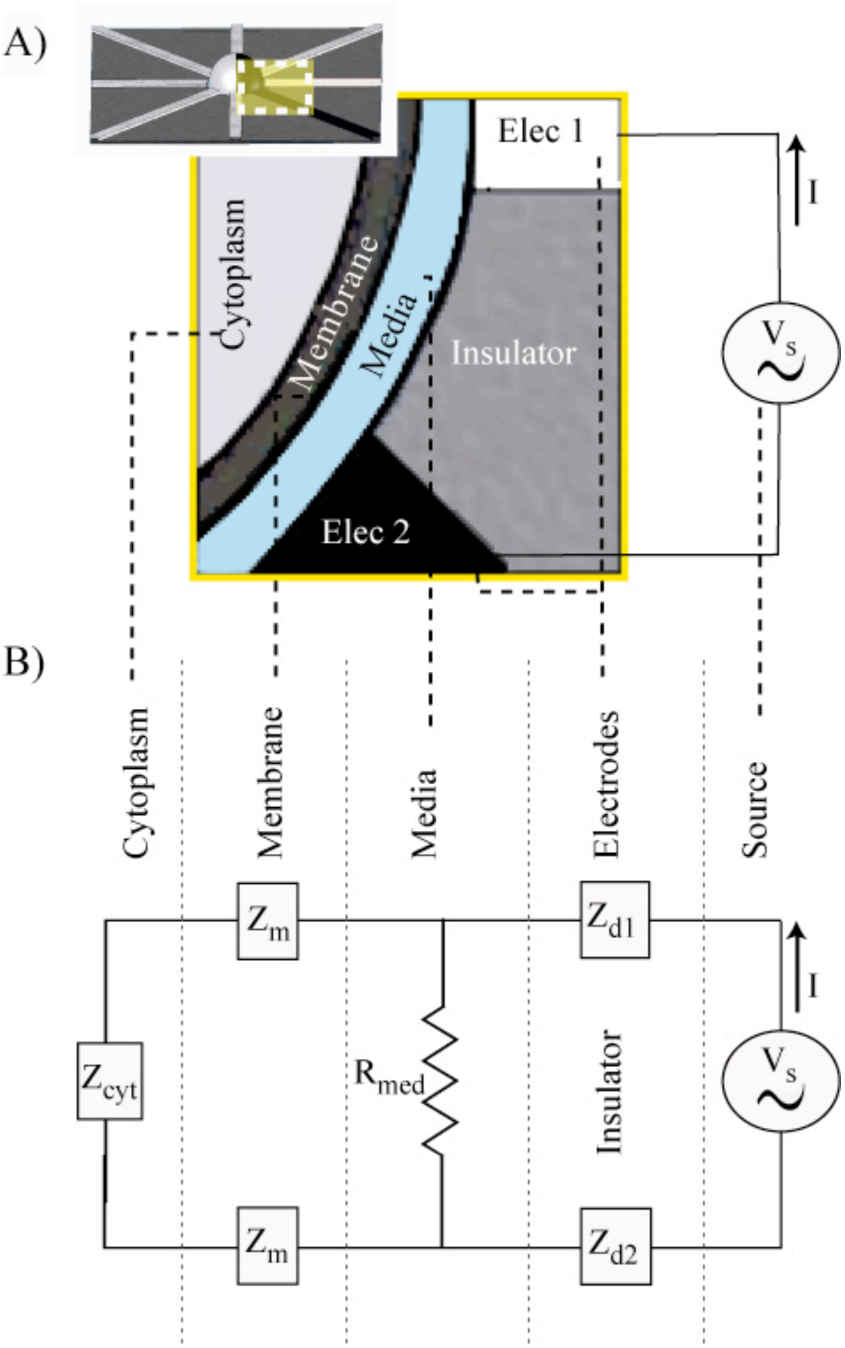

Fig 3.2 – Circuit Model - An electrical lumped parameter model of a cell in the recording chamber. Impedances shown are associated with the electrode–electrolyte interface (Z_{dl1}, Z_{dl2}), the shunt path around the cell (R_{med}) and the impedance of the cell including the membrane complex and intracellular space (Z_m, Z_{cyt}).

Fig. 3.3 – Quasi-Electrostatic 2D Model - A 2D frequency-domain (50 kHz–5 MHz) finite-element simulation of a cell in the recording chamber. Contours show lines of constant voltage. A) 50 kHz: Due to high resistance of the membrane, current flow is restricted to the extracellular space. B) 500 kHz: Current is divided between the cell membrane (displacement current) and the extracellular space (conductive current). C) 5 MHz: Almost all of the applied current is displaced across the highly capacitive cell membrane.

A) 50 kHz

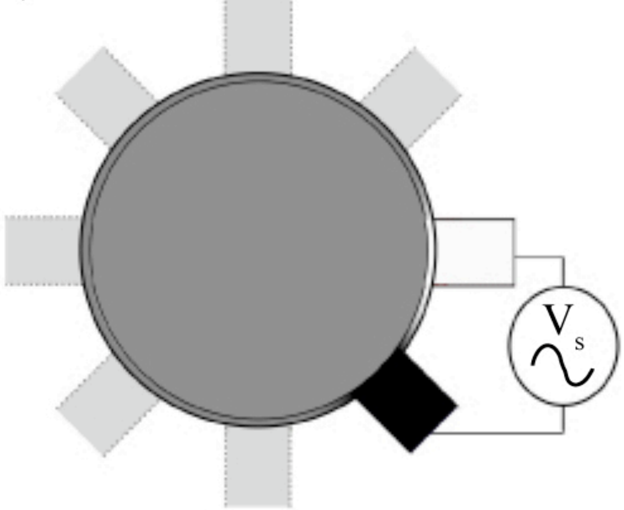

B) 500 kHz

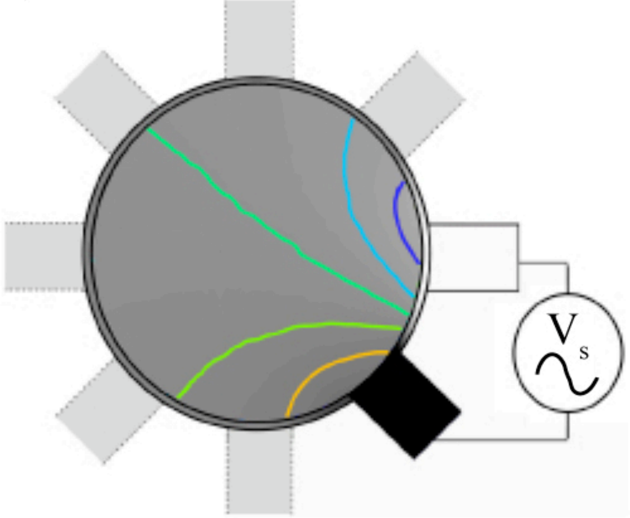

C) 5 MHz

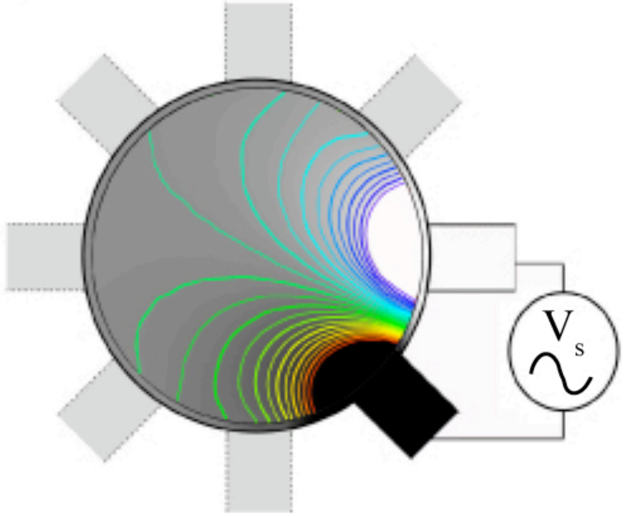

Fig. 3.4 – Glass Toroid Impedance Magnitude Image - Polar plots of impedance magnitude (right column) around glass toroidal phantoms reflect the orientation and shape of the phantom (left column: microphotographs of phantoms) in the recording chamber. Due to the highly resistive properties of glass, applied current (1 kHz– 1 MHz) shunted around the phantom and was not displaced across the phantom. Dotted lines in the polar plots (right column) show the second moments of area indicating maximal and minimal axes for each phantom. Solid lines show the second-order least-squared Fourier series representation of the phantom impedance data.

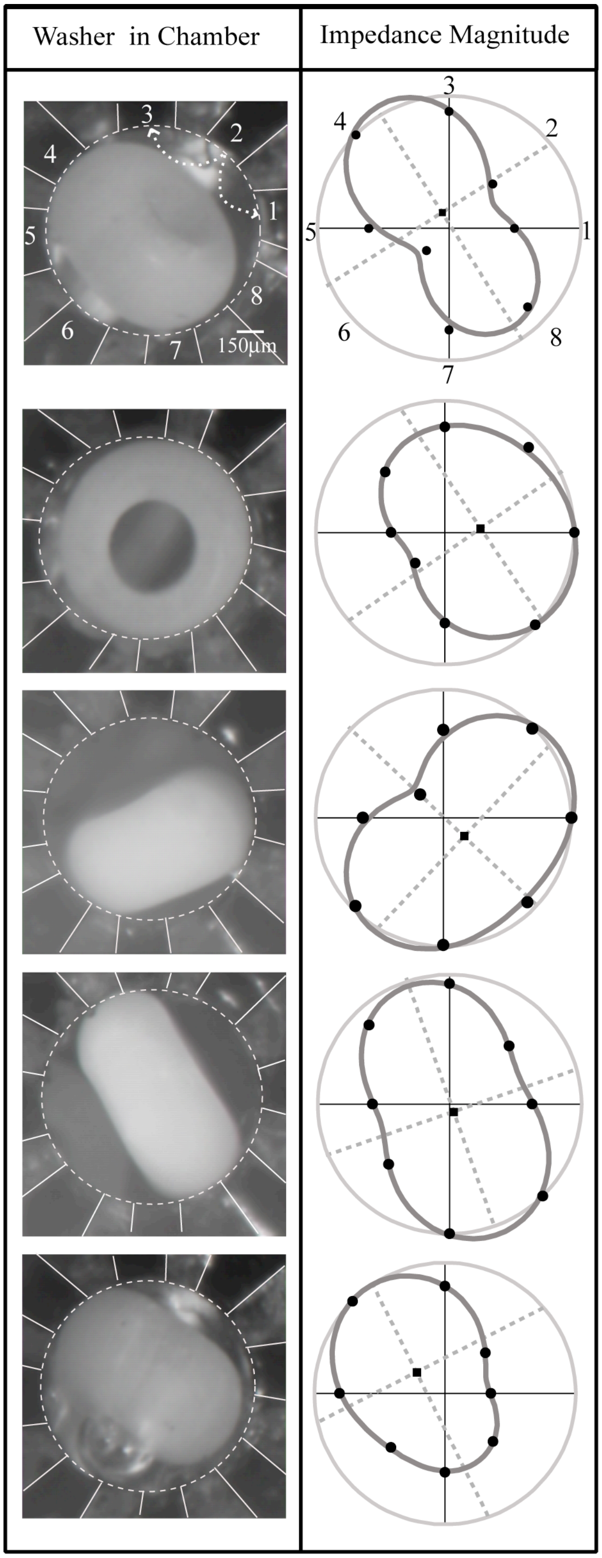
Washer in Chamber
Impedance Magnitude
3
2
4
1
5
8
6
7
150µm
3
4
2
5
1
6
8
7

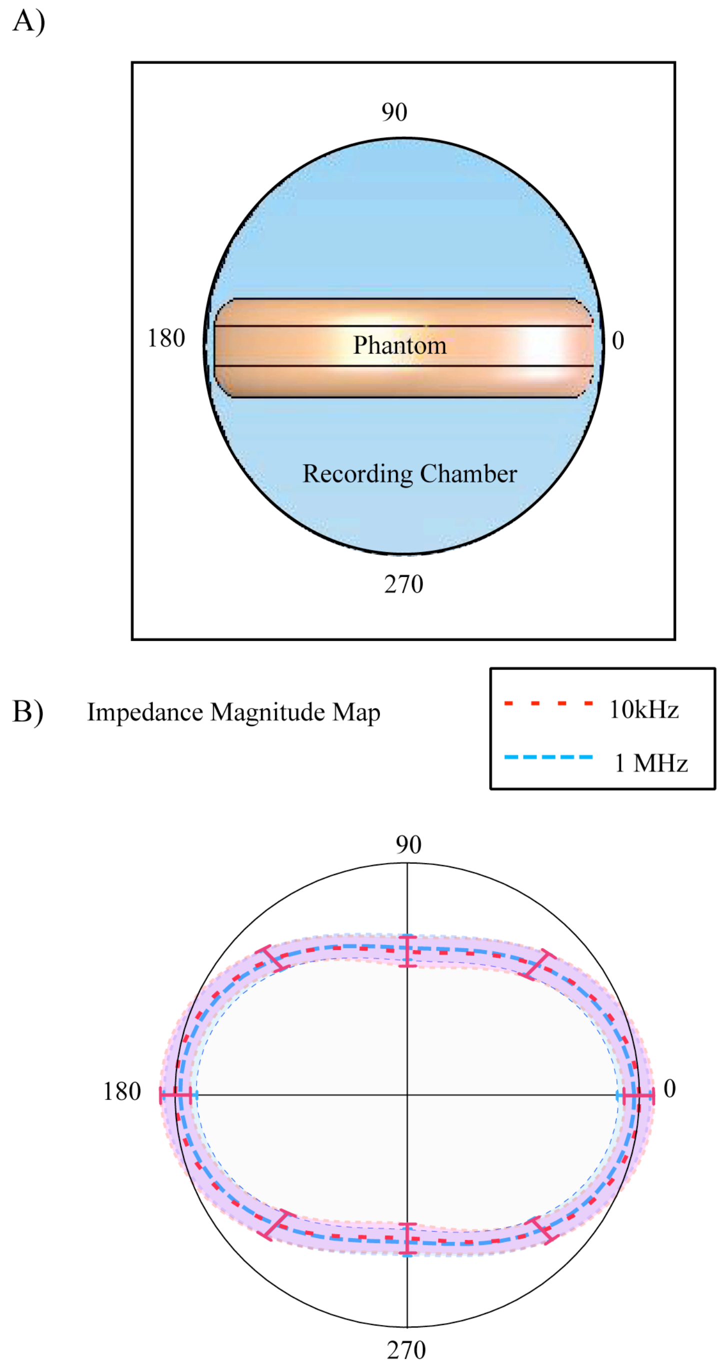

Fig. 3.5 – Phantom Summary - Data for each phantom (*n* = 9) were rotated based on photomicrographs to have the orientation shown in A (top-down view). Data were then averaged across phantoms, normalized and plotted in polar form (B: real, C: imaginary). Error bars denote 1 standard error of the mean. Data at 10 kHz and 1 MHz are nearly identical, as would be expected since the applied current at these frequencies should shunt around the highly resistive phantom.

Fig. 3.6 – Cell Summary - Data for *Xenopus* oocytes ($n = 8$) were rotated based on photomicrographs of each cell to have the orientation shown (A). B) Real component and C) imaginary component of the impedance. Results are shown at 10 kHz (pink, longer error bar ends) and at 1 MHz (blue, shorter error bar ends) with error bars denoting one standard error of the mean. Error bars denote 1 standard error of the mean. The difference between the high and low frequency measurement are significantly different when comparing the vegetal hemisphere of the oocyte to the animal hemisphere.

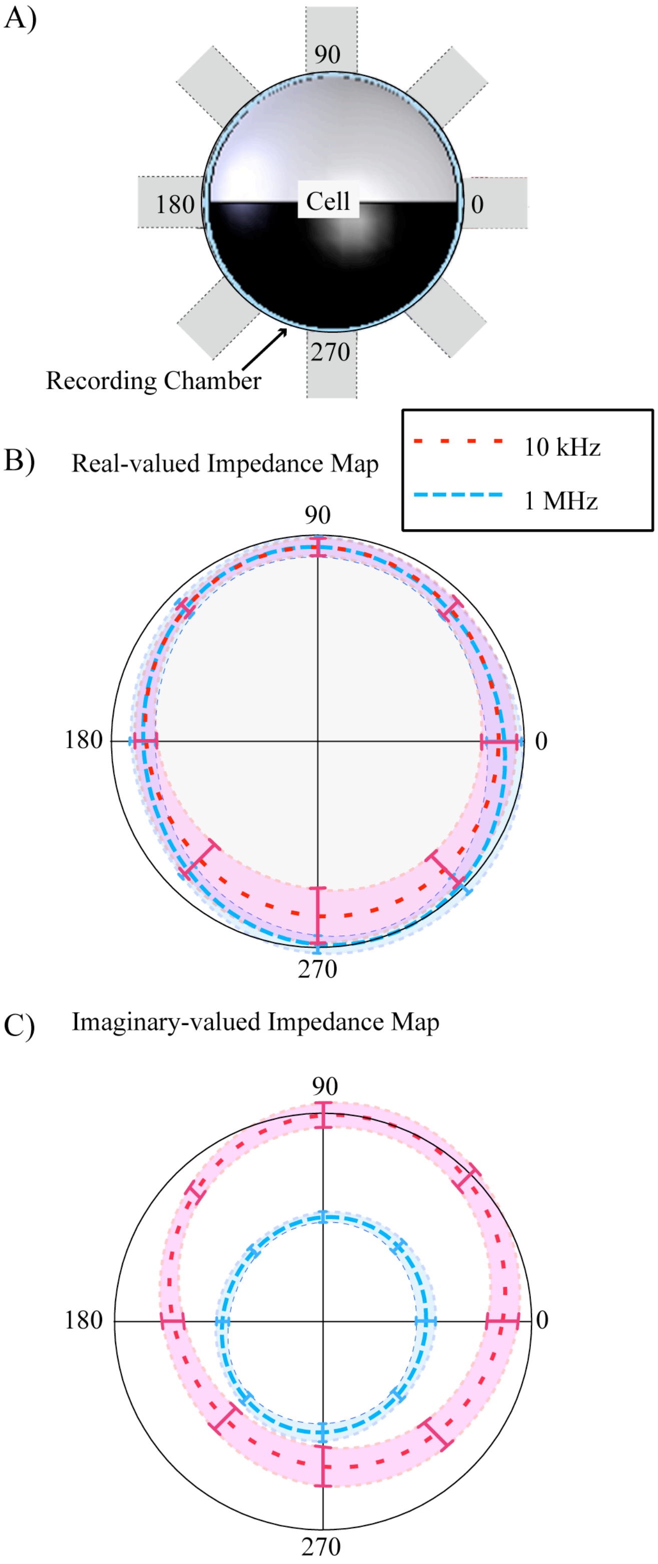
A)
90
180
Cell
0
270
Recording Chamber
B)
Real-valued Impedance Map
10 kHz
1 MHz
90
180
0
270
C)
Imaginary-valued Impedance Map
90
180
0
270

CHAPTER 4

MONITORING VOLTAGE-SENSITIVE MEMBRANE IMPEDANCE CHANGE USING RADIO FREQUENCY INTERROGATION[1]

Published: Sameera Dharia, Student Member, IEEE, and Richard D. Rabbitt.

Proceedings of the Annual International Conference of the IEEE-EMBS (2010).

This material is posted here with permission of the IEEE. Such permission of the IEEE does not in any way imply IEEE endorsement of any of the University of Utah's products or services. Internal or personal use of this material is permitted. However, permission to reprint/republish this material for advertising or promotional purposes or for creating new collective works for resale or redistribution must be obtained from the IEEE by writing to pubs-permissions@ieee.org. By choosing to view this material, you agree to all provisions of the copyright laws protecting it.

---

[1] © 2010 IEEE. Reprinted, with permission, from Proceedings of the Annual International Conference of the IEEE-EMBS 2010, Monitoring Voltage-Sensitive Membrane Impedance Change using Radio Frequency Interrogation, Dharia, S. and Rabbitt, R.

4.1 Abstract

Here we present a new technique to monitor dynamic conformational changes in voltage-sensitive membrane-bound proteins using radio frequency (RF) impedance measurements. *Xenopus* oocytes were transfected to express *Shaker*B-IR K+ ion channels, and step changes in membrane potential were applied using two-electrode voltage clamp (TEVC). Simultaneously, bipolar extracellular electrodes were used to measure the RF electrical impedance across the cell (300 kHz - 1 MHz). RF current will either pass through the media, around the cell or displace charge across the cell membrane. The change in displacement current in the cell membrane during voltage clamp resulted in measurable RF impedance change. RF impedance change during DC membrane depolarization was significantly greater in *Shaker*B-IR expressing oocytes than in endogenous controls at 300 kHz, 500 kHz and, to a lesser extent, 1 MHz. Since the RF were too high to modulate *Shaker*B-IR protein conformational state (e.g. open channel probability), impedance changes are interpreted as reflections of voltage-dependent protein conformation and associated biophysics such as ion-channel dipole interactions, fluctuations in bound water or charged lipid head-group rotations.

4.2 Introduction

Dynamic detection of charge displacement in electrically excitable cell membranes provides biophysical insight into voltage-sensitive membrane-bound protein physiology, such as mechanisms for protein stabilization, conformational change and ionic current (Alvarez & Latorre, 1978; Pethig, 1979; Conti & Stuhmer, 1989; Cha & Bezanilla, 1997; Bezanilla & Stefani, 1998; Glauner *et al.*, 1999;

Bezanilla, 2000a; Hille, 2001; Sigg *et al.*, 2003a; Branden *et al.*, 2006). As such, monitoring membrane dielectric is of great interest as a tool in basic science. Charge displacement measurements could also be used to track the kinetics of a charged drug binding to the membrane and has relevance in pharmaceutics.

Monitoring small changes in effective dielectric during membrane electrical excitation is difficult, in part due to challenges associated with conventional pipette-based electrophysiological techniques. Glass pipettes have sizeable stray capacitance that limits recordings to relatively low frequencies (Cahalan & Neher, 1992b; 1997). Increasing the interrogation frequency beyond the typical patch-pipette range lowers the capacitive component of membrane impedance and enables a more sensitive detection of membrane dielectric properties. The present report describes a new technique that uses RF interrogation between extracellular electrodes to dynamically monitor excitable membrane RF impedance changes evoked by step pulses in whole-cell voltage clamp.

In the present study, *Shaker* potassium ion channels with fast inactivation removed (*Shaker*B-IR) were expressed in *Xenopus* oocytes and RF impedance was compared to oocytes with endogenous protein expression only (control) (Hoshi *et al.*, 1990). Data indicate that *Shaker* RF-impedance is dependent on membrane voltage in a nonlinear way. Furthermore, *Shaker* RF-impedance measurements are significantly larger than control cell responses under the same conditions. Data are consistent with the hypothesis that RF-impedance reflects voltage-dependent changes in protein conformation and associated change in electrical dipole moments with ion channel opening (Pethig, 1979; Foster & Schwan, 1989).

4.3 Methods

4.3.1 Oocyte Protein Expression

Xenopus oocytes, known to express large amounts of specified exogenous membrane-bound proteins, were isolated and injected with *c*RNA using facilities at the University of Utah’s Cardiovascular Research and Training Institute. Complementary deoxyribonucleic acid (cDNA) for the Shaker ion-channel variant ShakerB-IR (inactivation removed) was transformed in *E.coli* and linearized using the restriction enzyme, Kpn-1. cRNA was transcribed from linearized DNA, and 32 nL/cell of the transcribed RNA was injected into oocytes. Recordings were done 24-48 hours after injection to allow time for protein expression. Currents were measured using two-microelectrode voltage clamp to verify ShakerB-IR ion channel expression. Oocytes were stored in Superbarths Oocyte media (88 mM NaCl, 1 mM KCl, 0.41 mM CaCl2, 0.33 mM Ca(NO3)2, 1 mM MgSO4, 2.4 mM NaHCO3, 10 mM HEPES, 1 mM pyruvate and 50 µg/ml gentamicin, titrated using NaOH to a pH of 7.4) at 17° Celsius (C). Oocytes were also bathed in this media during RF recording.

4.3.2 Recordings

Oocytes were positioned into a recording chamber consisting of a belt of RF excitation electrodes surrounding the meridian of the cell and a ground electrode located in the oocyte media above an axial pole of the cell (Fig. 4.1). The RF electrode array and oocyte positioning system have been described previously (Dharia *et al.*, 2009). In the present experiments, all of the excitation electrodes were wired together such that the RF electrical currents were applied in a ring around the oocyte meridian. Two glass micropipettes (1-3 MΩ access resistance) filled with 3M KCL were carefully guided into the oocyte using an upright microscope (Zeiss AxioTech). One micropipette was attached to a voltage-measuring headstage (HS-2Ax1LU, Molecular Devices, Sunnyvale, CA) and the second micropipette was attached to a current-injecting headstage (HS-2Ax10MGU, Molecular Devices, Sunnyvale, CA). These pipettes, in addition to a voltage-driving amplifier, were used to control low frequency (~DC steps) two-electrode voltage clamp in an oocyte (AxoClamp2B, Molecular Devices, Sunnyvale, CA). Each oocyte was held at a -90 mV (holding potential) and was remotely commanded to three potentials using voltage-clamp software: -120 mV, -30 mV and +40 mV (Patchmaster, HEKA Inst., Bellmore, NY). Voltage-command sequences were applied to cells between 50-200 times and responses were averaged to improve the signal/noise (S/N) ratio in the electrode current and, more importantly, the RF lock-in data. An on-board voltage divider circuit was used to measure the RF current and voltage (Dharia *et al.*, 2009). The RF source outputted a 300 mV (0-peak), randomized sinusoidal voltage (300 kHz, 500 kHz or 1 MHz; AFG320, Tektronix, Beaverton, OR). Voltage measurements were made relative to a Ag/AgCl ground wire placed ~5 mm above the cell in recording chamber media. This ground was common for both the RF and TEVC measurements (Fig. 4.1B).

RF voltage measurements were sampled through a head-stage voltage-follower operational amplifier (OPA356, Texas Instruments, Dallas, TX). The RF signal was high pass filtered (100 kHz, 48 db/oct Bessel HPF; SIM965, Stanford Research Systems, Sunnyvale, CA) and detected by a lock-in amplification (0 integration time, SR844, Stanford Research Systems, Sunnyvale, CA). The quadrature outputs on the lock-in amplifier detected changes on the order of 10 microvolts, and time delays caused by the lock-in amplifier and HPF were accounted for prior to data analysis. TEVC data (command voltage, sensed voltage, measured current) and RF data (quadrature outputs from the lock-in amplifier) were sampled every 20 μs using a 16 bit A-D converter (ITC-18, HEKA Inst. Bellmore, NY).

4.3.3 Electrical Model

A lumped parameter model of the chamber shown in Fig. 4.2A was used to estimate expected RF frequency responses. Parameters were R_s and R_i = ~ 1 kΩ (estimated using media-only chamber measurements), R_m = 1 MΩ and C_m = 2.3 pF and 1.8 pF (C_m values for lower and higher trace, respectively). C_m = 2.3 pF was estimated from the membrane-specific capacitance value, 4 $\mu F/cm^2$, for a *Xenopus* oocyte (Dascal, 1987). Electrical double-layers (Zdl1, Zdl2) were not modeled and were considered unknowns in the experiments. Partially because of this unknown, we report only changes in RF impedance relative to the holding potential (-90 mV).

4.3.4 Data Analysis

Both TEVC and RF data were postprocessed to 1) compensate for TEVC leak current and 2) calculate change in RF impedance of a cell stepped from holding potential to a command membrane potential (IgorPro, Wavemetrics, Lake Oswego, OR). Multiple acquisitions under identical conditions were averaged together for individual cells: TEVC and RF data were recorded for each voltage-command train (command voltage signal, sensed voltage (TEVC), injected current (TEVC) and x/y lock-in data). This averaging was done for each cell, for each frequency (300 kHz, 500 kHz or 1 MHz) and for each command potential (-120 mV, -30 mV or 40 mV). Membrane leak currents were compensated in individual cells. Membrane leak current varies linearly with voltage and is the predominant current measured at hyperpolarized potentials. Thus, TEVC cell currents measured here during hyperpolarization (-120 mV) were used to estimate leak currents.[2] For population results, TEVC and RF data were averaged across 1) *Shaker* injected cells and 2) control cells (endogenous oocyte protein expression only) for each interrogation frequency (300 kHz, 500 kHz and 1 MHz) and voltage-command step (-120 mV, -30 mV, 40 mV). All data were binned in 1 ms intervals for the 40 ms prior to the voltage command, the 40 ms during the voltage command and the 40 ms after the voltage command. Data reflect collective movement of a population of ion channels (not that of a single channel). Quadrature RF voltage was compared to the average quadrature RF voltage of the cell 5-40 ms prior to cellular excitation (holding potential = -90 mV). The magnitude of the change in impedance ($|\Delta \text{ Zc}|$) is reported here (e.g. Fig. 4.3A). Since the RF measurements include contributions from all membrane proteins and constituents, control cell RF impedance change was subtracted from *Shaker* impedance change to isolate *Shaker* component from endogenous response. The magnitude of impedance change 10-30 ms after depolarization was averaged to estimate a steady state change in impedance value (e.g. Fig. 4.4). *Shaker* data were normalized by TEVC current to account for protein expression (*n*=5). A two-tailed Student's t-test with a p-value of .05 was used for all tests of statistical significance.

---

[2] Calcium-activated chloride channels can also elicit currents at -120 mV, although the currents measured here predominately had leak-current characteristics.

4.4 Results

4.4.1 Modeling

Present experiments were designed to examine charge displacements associated with voltage-sensitive proteins in the cell membrane. We formulated the simple lumped parameter model shown in Fig. 4.2A to estimate the magnitude of RF impedance change expected to occur for a small change in effective capacitance of the oocyte membrane. At low frequencies, below the membrane RC corner frequency, the RF impedance is dominated by the conductive shunt path around the cell, thus impeding measurement of membrane conductance using extracellular electrodes. In contrast, based on this simple model, small changes in membrane impedance (ΔZc, plotted as a magnitude) caused by a change in membrane capacitance should be observable in the 100 kHz – 3 MHz frequency band (2b). The present study examined RF impedance within this band at 300 kHz, 500 kHz and 1 MHz (2b, dotted lines).

4.4.2 RF Data

*Shaker*B-IR expressing oocytes and those expressing endogenous channels only (control) were used to track millisecond changes associated with change in membrane impedance (|Δ Zc|) during TEVC electrical stimulation. Temporal resolution was limited by the maximum sampling rates of the data acquisition software; however, the system could eventually be used to track membrane changes on a microsecond time scale. Endogenous channel response was subtracted from the response of *Shaker*B-IR expressing oocytes (see Methods). Fig. 4.3A shows *Shaker*B-IR (*n*=5, control: *n*=6) change in RF impedance |Δ Zc| collected using 500 kHz interrogation for depolarized (black line, ~ 40 mV), slightly depolarized (dark gray line, -28 mV) and hyperpolarized (gray line, ~-120 mV) membrane potentials. Membrane current (leak subtracted, Fig. 4.3B) and voltage (Fig. 4.3C) were monitored using conventional TEVC for both *Shaker*B-IR and control oocytes. *Shaker*B-IR injected oocytes achieved a 3 µA current at the 40 mV depolarization (black line), as expected (Hoshi *et al.*, 1990). Control oocytes did not exhibit significant currents during depolarization. |Δ Zc| and ionic current increased nonlinearly in *Shaker* expressing oocytes.

The steady-state (60-80 ms in Fig. 4.3) change in RF impedance (|Δ Zc|) is summarized for 300 kHz, 500 kHz and 1 MHZ interrogation frequencies in Fig. 4.4. Impedance changes are relative to the RF impedance measured at the -90 mV holding potential, and are shown for voltage steps to -118 mV (control: *n*=7, *Shaker*B-IR: *n*=5), -28 mV (control: *n*=6, *Shaker*B-IR: *n*=5) and +41 mV (control: *n*=7, *Shaker*B-IR: *n*=5). At the -28 mV voltage step, when the *Shaker* channel was just beginning to open, a significant increase in steady-state |Δ Zc| was measured at 300 kHz between *Shaker*B-IR and the control oocytes. Results show statistically significant (*, $p<.05$) differences between RF impedance changes in *Shaker*B-IR vs. control cells at the 41 mV membrane depolarization as well. Hence, opening of *Shaker*B-IR channels causes an increase in membrane polarization that is detectable with RF interrogation frequencies.

4.5 Discussion and Conclusion

Membrane-voltage dependent changes in RF impedance (300 kHz, 500 kHz, 1 MHz) were analyzed for *Shaker*-expressing oocytes and control oocytes (endogenous protein expression only). Differences between these data sets reflect changes in effective membrane capacitance imparted by voltage-dependent changes in *Shaker* ion channels. Results show that the RF impedance change with TEVC depolarization was significantly larger in *Shaker* expressing cells than control cells. This held true for all three interrogation frequencies. Statistically significant differences in RF impedance change between *Shaker* cells and control cells were not present when cells were hyperpolarized. It is unlikely that ion-channel conformational state (e.g. from open-close) was modulated by the RF interrogation frequencies used in these experiments. Data suggest that the open vs. closed states of *Shaker* ion channels lead to distinctly different electric dipole charge/mobility, leading to distinctly different effective membrane capacitance; these differences can be measured using RF frequencies. Presumably, this dielectric behavior has origins in radio-frequency molecular dynamics of the protein-membrane-ion complex. While the RF-technique presented here used oocytes injected with well-characterized *Shaker* channels, oocytes could potentially be injected with cRNA that encodes for other protein types as well, and this method may prove to be a useful tool to examine dynamic movements in a multitude of excitable membrane-bound proteins.

Fig. 4.1 – The Method - Detecting Voltage-Sensitive Changes in RF Membrane Impedance. A cell, positioned in a recording chamber milled into a polycarbonate interface (PC, Fig. 4.1A), is electrically excited using two-electrode voltage clamp (TEVC, TEVC electrodes are shown in sketch as V-sense and I-inject, Fig. 4.1A and Fig. 4.1B). Changes in voltage-sensitive membrane impedance induced by TEVC excitation are simultaneously monitored using radio wave interrogation. A radially distributed electrode array (EA, all electrodes shorted together), clamped within the two plates of the polycarbonate interface, passes signals from a sinusoidal voltage source (Vs, Fig. 4.1A), through the cell/conductive media in the recording chamber, to electrical ground (located several millimeters above the cell, Fig. 4.1B). The source, reference impedance (Zref, Fig. 4.1A) and voltage-measuring site (Vm, Fig. 4.1A), are used to monitor changes in RF membrane impedance during membrane voltage-clamp. Signal integrity during measurement is preserved by headstage amplification (HA, Fig. 4.1A) and lock-in amplification. Fig. 4.1B shows a cross section of the cell as it sits in the recording chamber (segment 1-1’).

1a)

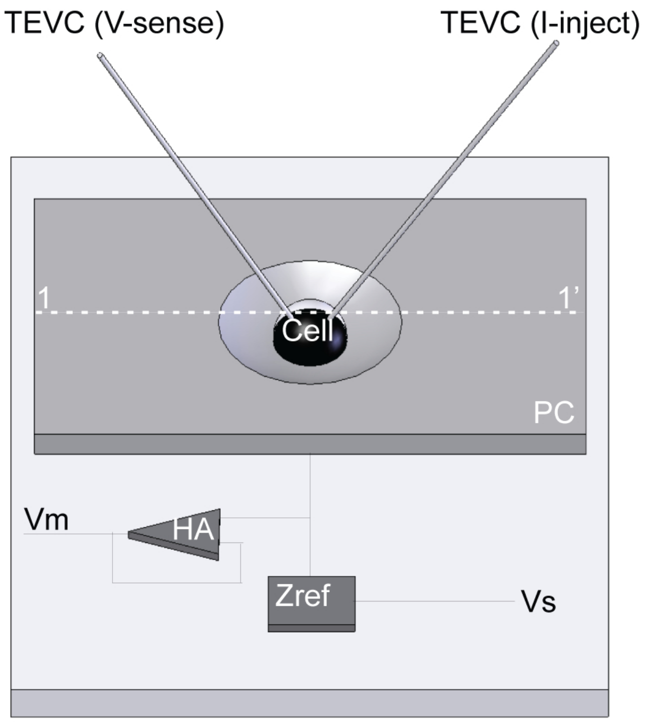
TEVC (V-sense)
TEVC (I-inject)
1
1'
Cell
PC
Vm
HA
Zref
Vs

1b)

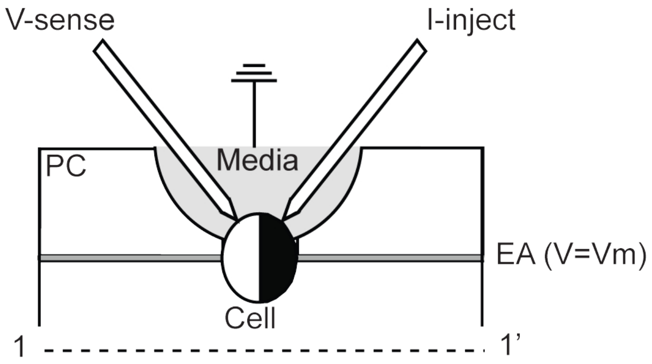
V-sense
I-inject
Media
PC
EA (V=Vm)
Cell
1
1'

Fig. 4.2 – Fig. 4.2A shows a lumped parameter model of the recording chamber (Zc). Zc consists of a double-layer interfacial impedance associated with the electrode that surrounds the cell (Zdl), the shunt path around the cell (Rs) and the impedances associated with the cell membrane (Rm – membrane resistance, Cm – membrane capacitance and Ri –intracellular solution resistance). The double-layer impedance associated with the Ag/AgCl ground wire is nearly 0, as the wire is (approximately) nonpolarizable. The lumped parameter model shown in Fig. 4.2A was solved, and results (shown in Fig. 4.2B) demonstrate the effect of frequency on measured impedance magnitude (the upper trace has a lower membrane capacitance than the lower trace). Results indicate that that frequencies in the 100 kHz – 3 MHz range will be most effective for detecting change in membrane dielectric during voltage-clamp. Three frequencies were chosen (300 kHz, 500 kHz and 1 MHz) for experimental validation.

2a)

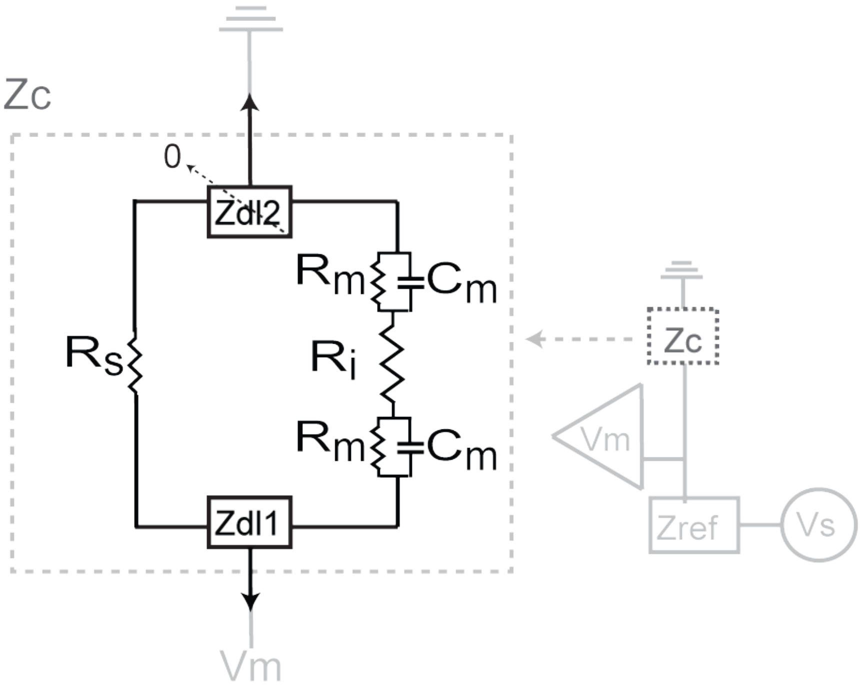
Zc
0
Zdl2
Rm
Cm
Rs
Ri
Rm
Cm
Zdl1
Vm
Zc
Vm
Zref
Vs

2b)

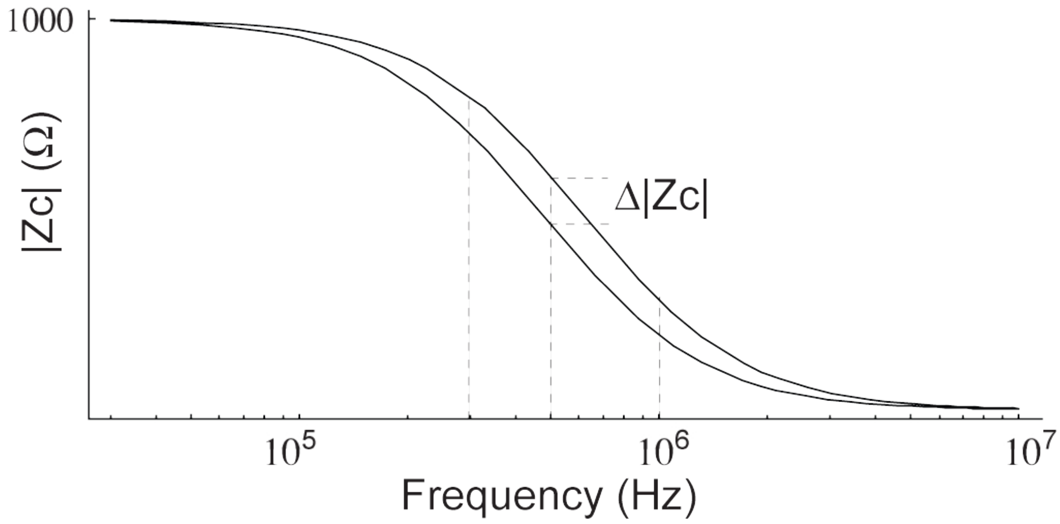
1000
|Zc| (Ω)
Δ|Zc|
10^5
10^6
10^7
Frequency (Hz)

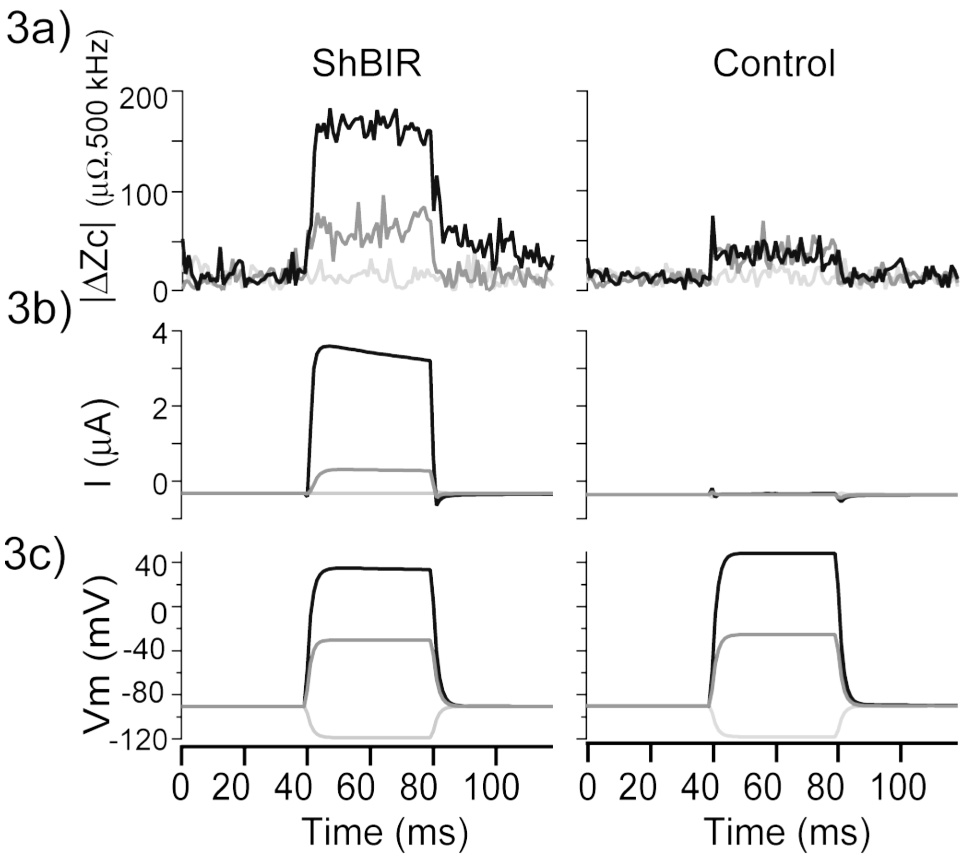

Fig 4.3 – Millisecond resolution of |Δ Zc| (3a, collected using a 500 kHz interrogation frequency) for *Shaker*B-IR expressing oocytes (endogenous protein expression (average control cell response) subtracted) and oocytes expressing endogenous protein only (control) in response to TEVC excitation. Membrane potential (TEVC) during experimentation for both *Shaker* and control cells is shown in 3c (-120 mV (gray trace), -30 mV (dark gray trace) and 40 mV(black trace)). Holding potential for the clamp was set at -90 mV, and the onset of cellular excitation occurred at 40 ms for a 40 ms duration. Ionic conduction current traces (after leak subtraction) (3b) measured using TEVC verify channel expression in the *Shaker*B-IR cell and lack of expression (after leak subtraction) in the control oocytes.

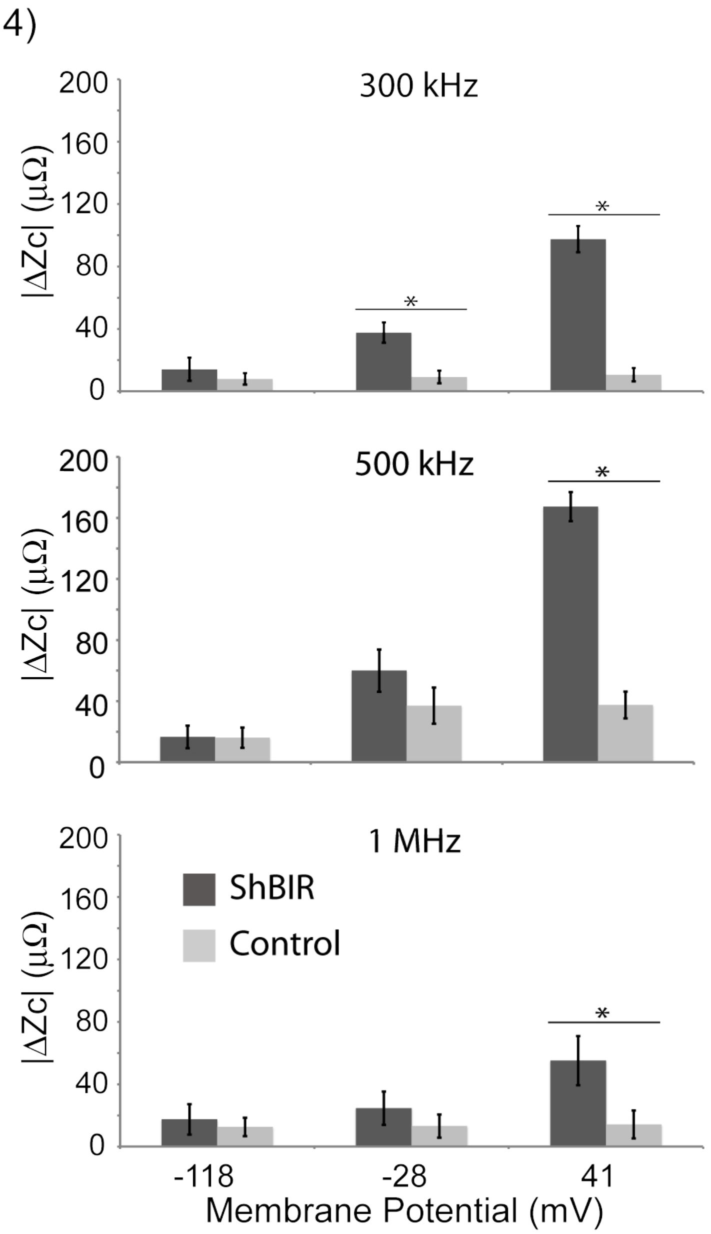

Fig. 4.4 – Steady state values of |Δ Zc| (measured at 300 kHz, 500 kHz and 1 MHz) were compared for both control and *Shaker* BIR data when the cell was stepped to three membrane potentials (-118 mV, -28 mV, 41 mV). The corresponding TEVC currents are shown in Fig. 4.3B. Significant differences ($p < .05$) in measured RF steady-state |Δ Zc| between *Shaker* and control cells are denoted by asterisks.

CHAPTER 5

MONITORING VOLTAGE-DEPENDENT CHARGE DISPLACEMENT OF *SHAKER* B-IR K^+ ION CHANNELS USING RADIO FREQUENCY INTERROGATION

Accepted (PLoS-ONE)[1]: Sameera Dharia and Richard Rabbitt

5.1 Abstract

Here we introduce a new technique that probes voltage-dependent charge displacements of excitable membrane-bound ion-channel proteins using extracellularly applied radio frequency (RF, 500 kHz) electric fields. *Xenopus* oocytes were used as a model cell for these experiments, and were transfected with cRNA encoding *Shaker* B-IR (*Sh*B-IR) K+ ion channels to express large densities of this protein in the oocyte membranes. Two-electrode voltage clamp (TEVC) was applied to command the whole-cell membrane potential and to measure channel-dependent membrane currents. Simultaneously, RF electric fields were applied to perturb the membrane potential about the TEVC level and to measure voltage-dependent RF displacement currents. *Sh*B-IR

---

[1] This manuscript will be published in PLoS-ONE, an open-access journal published by the Public Library of Science.

expressing oocytes showed significantly larger voltage-dependence of the net RF displacement current than control oocytes. Voltage-dependent changes in RF displacement currents further increased in *Sh*B-IR expressing oocytes after addition of 120 μM Cu^{2+} to the external bath. Cu^{2+} is known to bind to the *Sh*B-IR ion channel and block *Shaker* K^+ conductance, indicating that changes in the RF displacement current reported here were associated with RF vibration of the Cu^{2+}-linked mobile domain of the *Sh*B-IR protein. Results demonstrate the use of extracellular RF electrodes to interrogate voltage-dependent movement of charged mobile protein domains -- capabilities that might enable detection of small changes in charge distribution associated with integral membrane protein conformation and/or drug–protein interactions.

5.2 Introduction

Techniques to monitor displacement currents in the protein-rich cell membrane have been used extensively in previous studies to examine ion-channel voltage-sensor movement (Armstrong & Bezanilla, 1977a; Perozo *et al.*, 1993; Sigg *et al.*, 1994; Cha & Bezanilla, 1997; Sigg & Bezanilla, 1997; Glauner *et al.*, 1999) and the piezoelectric-like behavior of transmembrane proteins (Zheng *et al.*, 2000; Santos-Sacchi & Navarette, 2002; Rabbitt *et al.*, 2005). These and similar studies record the magnitude and timing of charge displacement in the membrane to reveal the nature of voltage-dependent protein function and excitability in living cells. One technical challenge has been the electrical capacitance of the membrane lipid bilayer itself, which is in parallel with integral membrane proteins and obscures observations of protein-dependent electrical charge movements. This is compounded by the passive capacitance of the patch-clamp glass/quartz pipette that often limits the bandwidth of displacement charge recording. In the present report, we introduce a new technique to monitor protein-dependent charge displacements by superimposing an extracellularly applied RF interrogation signal on top of a traditional voltage-clamp commanded membrane potential. This RF interrogation technique has its basis in electric impedance spectroscopy, which has been applied previously to probe membrane dielectric properties of isolated cells by measuring the electrical impedance between pairs or groups of extracellular electrodes (Gritsch *et al.*, 1998; Ayliffe *et al.*, 1999; Gawad *et al.*, 2001; Werdich *et al.*, 2004; Cheung *et al.*, 2005; Han & Frazier, 2006). Here, we extend such RF dielectric measurements to study electrical charge displacement arising from electrically excited voltage-sensitive membrane-bound proteins.

Xenopus oocytes were used as a model cell for these experiments because they express a large amount of exogenous protein in their membrane; in these experiments, oocytes were transfected with the *Shaker* gene encoding *Sh*B-IR (Dascal, 1987; Hoshi *et al.*, 1990; Iverson & Rudy, 1990; Hoshi *et al.*, 1991; Stuhmer, 1992; Werdich *et al.*, 2004), a well-characterized voltage-sensitive K^+ ion channel with fast inactivation removed. A custom recording chamber was devised to allow for simultaneous two-electrode voltage clamp (TEVC) and RF impedance interrogation (Fig. 5.1A). Oocytes were placed individually into the center of an annular electrode that formed a tight conducting extracellular belt around the meridian of an oocyte (Fig. 5.1A). RF signals were passed from the annular belt (black electrode in Fig. 5.1A) to a single ground-wire electrode located above the oocyte. Quadrature lock-in amplification was used to measure the frequency-domain RF component of the voltage drop (V_{RF}), current (I_{RF}) and impedance ($Z_{RF}=V_{RF}/I_{RF}$) across the recording chamber. In this configuration, the RF component of the total current I_{RF} was the sum of the conductive shunt current around the cell and the displacement current in the plasma membrane complex (Fig. 5.1B). Since the extracellular shunt conductance was much greater than the membrane conductance (Fig. 5.1B, $1/R_s >> Real(1/Z_m)$), RF impedance was not sensitive to voltage-dependent changes in membrane conductance (Dharia *et al.*, 2009). Fig. 5.1C illustrates that a change in membrane displacement current would be detectable only over a limited frequency range due to the fact that shunt resistance (R_s) would dominate at low frequencies and membrane capacitance would effectively short at high frequencies. In fact, previous work has shown extracellular shunt path estimation (frequencies < 100 kHz) can be used to map cell shape in a recording chamber, and that frequencies above 3 MHz may be used to interrogate intracellular organelle distribution (Dharia *et al.*, 2009). Examination of the impedance spectra for the specific system used in the present study revealed 500 kHz to be near the center of the sensitive range to maximize detection of membrane-related RF charge displacements (Dharia & Rabbitt, 2010).

Here we report changes in 500 kHz RF charge displacement evoked by step changes in membrane potential. TEVC was used to step the membrane potential (V_m^*) in the time domain, and to measure whole-cell currents (I_m^*, Fig. 5.1A). RF interrogating signals (V_{RF}, I_{RF}) were superimposed on top of the low-frequency TEVC commands. TEVC V_m^* commands were low-pass filtered at 30 kHz so the TEVC signal contributed negligible power at the 500 kHz RF interrogation frequency. Similarly, TEVC I_m^* signals were low-pass filtered to avoid the RF component. Lock-in amplification was used to extract electrical signals at the RF interrogation frequency. Data for *Sh*B-IR expressing oocytes were compared to control oocytes to examine the contributions of the expressed ion channel relative to endogenous proteins and lipids constituting the native oocyte membrane (control). In a subset of experiments, ~120 μM Cu^{2+} was applied to shift the voltage-dependence of *Sh*B-IR to more depolarized levels (Elinder & Arhem, 2004; Ma *et al.*, 2008) and to bind charge to the protein. Results show significant differences between voltage-dependent RF charge displacements in *Sh*B-IR expressing oocytes vs. controls. Differences are significant near the half-activation potential for the *Sh*B-IR channels, suggesting that RF data might correspond to ion-channel activity. Results further show that Cu^{2+} increased the magnitude of RF charge displacement while simultaneously shifting V_m^* sensitivity to more depolarized levels on *Sh*B-IR expressing oocytes. This response was not noticeable in control oocytes, indicating that the RF signal measured reflects RF vibration of the channel protein–Cu^{2+} interaction. These results suggest that the RF-based technique introduced here could potentially supplement conventional membrane-biophysics studies, by monitoring RF mobility associated with membrane-bound charge distribution and charged molecule (potentially a drug)–protein interactions during voltage-clamp.

5.3 Results

5.3.1 Time-resolved Changes in RF Impedance

Fig. 5.2A compares time-resolved changes in RF impedance $|\Delta Z_{RF}|$ in control ooyctes expressing endogenous channels (avg. *n*=10, left) to oocytes expressing *Sh*B-IR channels (avg. *n*=9, right). Voltage-dependent RF charge displacement occurred in both cell expression systems, but differed in magnitude and temporal waveform between the control and *Sh*B-IR expressing oocytes[2]. The left axis reports the magnitude of the change in impedance, $|\Delta Z_{RF}| = |Z_{RF} - Z_0|$, where the reference, Z_0, for each record was the average RF impedance 5-40 ms prior to the voltage step. Although signals were noisy in our apparatus, milliohm changes in $|\Delta Z_{RF}|$ during depolarization were readily discernable from noise. In all cases, $|\Delta Z_{RF}|$ consisted of an initial onset response when the rate of change of TEVC membrane potential was large (**o,** $|\Delta Z_{RF}|_o$, $dV_m^*/dt > 0$) and a steady-state response when TEVC membrane potential was approximately constant (**s**, $|\Delta Z_{RF}|_s$, $dV_m^*/dt \cong 0$). The RF onset response (**o**) occurred in the first millisecond after a voltage step was applied to the cell, and was similar in both the control and *Sh*B-IR expressing oocytes. Interestingly, the RF onset response was rectified and did not occur at the end of the voltage command step. Hence, the fast RF onset response was not causally related to the standard TEVC capacitive transient (current spikes in Fig. 5.2B). Steady state RF changes (**s**) 5-35 ms after the voltage step were also observed in both control and *Sh*B-IR oocytes, but were significantly larger in the *Sh*B-IR expressing oocytes at membrane potentials above -20 mV. This indicated a difference in RF response attributable to *Shaker* activation. Simultaneous TEVC recordings shown in the lower panels (Fig. 5.2B, current; Fig. 5.2C, voltage) were used to confirm expression and test whole-cell currents. Darker lines indicate increased levels of depolarization during the voltage step, commanded from a holding potential of -90 mV (Fig. 5.2C). TEVC whole-cell currents in the control condition (Fig. 5.2B, left) were small relative to the large currents in *Sh*B-

---

[2] The RF onset response here can also observed in the control data for Fig. 4.3. $|\Delta Z_{RF}|$ is not directly comparable between the data in this paper and the previous paper, due to differences in shunt path around oocytes as well as slight differences in data acquisition. The RF response associated with *Sh*B-IR expressing oocytes is much larger than the control in Fig. 4.3 due to the larger *Sh*B-IR expression, and is the likely reason that the onset response is not noticeable in Fig. 4.3 *Sh*B-IR expressing data set.

IR expressing cells (Fig. 5.2B, right). Voltage sensitivity and sustained ionic currents reported here are typical for *Sh*B-IR cells with fast inactivation removed, and indicate successful protein expression and activity.

5.3.2 Steady-state RF Response for *Sh*B-IR and Control Cells

To further examine differences between steady-state RF impedance in control (*n*=10, “Endo”, orange) vs. *Sh*B-IR expressing oocytes (*n*=9, “*Sh*B-IR + Endo”, brown), we averaged $|\Delta Z_{RF}|_S$ 5- 35 ms (see Methods) after the onset of voltage step (see Methods), and plotted the result against the average membrane potential V_m^* (Fig. 5.3A). *Sh*B-IR expressing oocytes include the exogenously expressed *Sh*B-IR proteins and endogenous membrane proteins and both contribute to the RF data. Averaged control data were subtracted from the *Sh*B-IR expressing oocyte data, to estimate the RF response associated with the *Sh*B-IR protein only (3A, blue line). Error bars denote standard errors of the mean (+/-, SEM), and are shown as a function of V_m^* for *Sh*B-IR expressing oocytes and control oocytes in Fig. 5.3B. To demonstrate successful transfection, steady-state ionic currents are shown in Fig. 5.3C, and *Sh*B-IR channel conductance is shown as in the inset. Like the averaged RF data, the SEM associated with the *Sh*B-IR proteins-only was estimated by subtracting the SEM associated with the *Sh*B-IR expressing oocyte at each membrane potential from the control oocyte SEM(s) (see Methods). Significant differences in $|\Delta Z_{RF}|_S$ were found between *Shaker*-expressing oocytes and control oocytes at and above -10 mV, and differences are easily observable above the half-activation voltage for *Sh*B-IR channels ($^x p<0.10$, $^* p<0.05$, Fig. 5.3A). Interestingly, the RF *Sh*B-IR only data and the corresponding *Sh*B-IR conductance data (shown in Fig. 5.3C) have a linear correlation coefficient of .94 (and a correlation coefficient of .99 in the voltage range of -45 mV to 2 mV, when the *Sh*B-IR data increase from 5-95% of their final value), indicating a positive association between channel activity and the measured RF response. Furthermore, unlike the control oocytes that showed increased SEM for large V_m^*, the *Sh*B-IR only SEM (blue line, Fig. 5.3B) showed the largest value near the half-activation voltage (Fig. 5.3B), and standard errors for the *Sh*B-IR expressing oocytes were comparable to baseline values when the ensemble of channels in the membrane were predominantly closed or open. These results are consistent with voltage-dependent SEM arising from probabilistic conformational state of the *Shaker* ion-channels expressed in the membrane.

5.3.3 Copper Treatment and Steady-State *Sh*B-IR RF Response

A subset of *Sh*B-IR expressing oocytes (n=4) were treated with Cu^{2+}, a K^+ ion channel inhibitor, and normalized $|\Delta Z_{RF}|_s$ was determined for these oocytes before and after Cu^{2+} treatment (exp2). Results are shown in Fig. 5.4A as a function of steady-state membrane potential (V_m^*). Data from each cell were normalized to its RF impedance at +30 mV for the nontreated *Sh*B-IR expressing oocytes, to permit comparisons between cells before/after copper treatment (see Methods). As expected, Cu^{2+} application greatly reduced the *Sh*B-IR current (I_m^*) in the voltage-range where *Sh*B-IR channels activate (Fig. 5.4B). *Sh*B-IR channel conductance before and after copper addition are shown in the inset (Fig. 5.4B). The change in RF impedance after copper treatment was larger than the untreated condition (Fig 5.4). To examine statistical significance for this relatively small population, data above -60 mV (see Methods) were pooled together. Pooled data showed a statistically significant difference between nontreated vs. Cu^{2+} treated *Sh*B-IR expressing oocytes (*p*=.04, U=1007, Total Points=80, normalized median-values of the nontreated/treated *Sh*B-IR expressing oocytes are .36 and .90, respectively (see Methods)). Results from control cells (*n*=2, Fig. 5.4A) are scaled by the ratio of the control cell to *Sh*B-IR cell data at +30 mV (shown in Fig. 5.3) to enable intercellular comparison, after normalizing the data from each control cell to its nontreated $|\Delta Z_{RF}|_s$ measured at +30 mV (see Methods). A change in the normalized $|\Delta Z_{RF}|_s$ is noticeable in the control cells after Cu^{2+} application (above -60 mV), indicating that Cu^{2+} might nonspecifically interact with the endogeneous oocyte membrane in addition to the known effect of binding the *Sh*B-IR channels. While Cu^{2+} likely contributed to the change in RF response before/after Cu^{2+} addition, the effect in *Sh*B-IR expressing oocytes was much larger, suggesting that the RF detected Cu^{2+} interaction specifically with the *Shaker* channels. As depolarization level increased, the effect of the bound Cu^{2+} increased. At 30 mV, the Cu^{2+}-treated oocytes exhibited a response approximately 1.5 times that of the nontreated *Sh*B-IR expressing oocytes, even though the ionic current (TEVC) was approximately one fifth of the nontreated cells.

5.3.4 RF Onset Response in *Sh*B-IR Expressing Oocytes

RF onset responses, occurring during the rise of V_m^* (when dV_m^*/dt was maximum), exhibited trends different than those seen in steady state. Fig. 5.5 plots the onset response $|\Delta Z_{RF}|_o$, averaged 0-1 ms after voltage command was applied (see Methods) vs. membrane potential and rate of change (dV_m^*/dt). The data have been normalized using the same values in Fig. 5.4A, to allow for comparisons between transient and steady-state RF results (see Methods). The fast onset recorded in *Sh*B-IR expressing oocytes and controls both increased with the magnitude of the membrane potential change, but there were no statistically significant differences due to expression of K^+ channels (p>.05, data not shown). Onset RF charge displacements in control oocytes treated with Cu^{2+} slightly decreased as voltage-step increased (Fig. 5.5, filled circles). In contrast to *Sh*B-IR expressing oocytes, the average onset response of controls treated with Cu^{2+} was smaller than the nontreated cells. Cu^{2+} treated *Sh*B-IR expressing oocytes pooled for all voltage commands > -60 mV exhibited significantly larger onset responses than nontreated *Sh*B-IR expressing oocytes (p=.005, U=1087, Total Points = 80, median values untreated/treated *Sh*B-IR expressing oocytes of 1.0/1.4, respectively). Interestingly, increases in the onset $|\Delta Z_{RF}|_o$ for Cu^{2+} treated *Sh*B-IR expressing oocytes were about 1.5 times greater than those for Cu^{2+} treated *Sh*B-IR oocytes in the steady state ($|\Delta Z_{RF}|_s$). One hypothesis that might explain the Cu^{2+}-dependent onset response is that Cu^{2+} might stabilize a transitional state in the ion channel during rapid membrane depolarization that momentarily exposes additional charges on the protein, thereby enhancing the momentary RF charge displacement. The onset response was not detectable for $-dV_m^* /dt$ at the end of the command pulse (see Fig. 5.2A), showing a rectification in $|\Delta Z_{RF}|$ quite distinct from dV_m^* /dt driven linear capacitive transients (present in Fig. 5.2B).

5.4 Discussion

Here we introduce a new technique to monitor voltage-dependent charge displacement associated with *Sh*B-IR K^+ ion channels using RF electric fields during

TEVC. The RF electric field provided a vibrational force that resulted in measurable RF charge displacement on a cell membrane complex caused by vibrating membrane-bound charges. The 500 kHz RF was superimposed on top of low-frequency TEVC (<30 kHz) allowing the RF to continuously interrogate changes in charge displacement mobility during whole-cell depolarization. Changes in RF impedance, $|\Delta Z_{RF}|$, were recorded every 20 μs, and provided a nearly instantaneous view of the effective dielectric behavior of the protein–membrane–ion complex. Voltage-dependent changes in $|\Delta Z_{RF}|$ were averaged into millisecond bins (Fig. 5.2) and showed time-resolved differences for *Sh*B-IR expressing oocytes relative to controls, demonstrating the sensitivity of this approach to detect RF vibrational motion associated with ion-channel-specific charge displacements.

Analysis of RF charge displacements revealed significant differences in $|\Delta Z_{RF}|_s$ between *Sh*B-IR expressing oocytes and controls at depolarized membrane potentials (Fig. 5.3A). Differences were largest above the half-activation potential for the *Shaker* channels used here. The *Sh*B-IR channels have fast inactivation removed, and as such, significant changes in steady-state RF vibration demonstrate that the open conformation of *Sh*B-IR channels have measurably different effective dielectric behavior than the closed conformation. It is important to note that this difference was present at steady-state and did not reflect the classical gating charge movement that typically occurs for these channels ~0-2 ms after voltage command(Perozo *et al.*, 1993; Hille, 2001). Instead, voltage-dependent changes in RF charge displacement $|\Delta Z_{RF}|_s$ appear to reflect changes in mobile charge displacement magnitude within the transmembrane RF electric field and/or stiffness associated with the open vs. closed state of the *Shaker* protein (measured during steady-state). Consistent with this, the steady-state RF impedance associated with the

*Sh*B-IR proteins had a positive correlation with channel conductance (c.f. blue curve in Fig. 5.1A and 5.1C inset). This hypothesis is further supported by the fact that the SEM for the *Sh*B-IR proteins (*Sh*B-IR expressing oocytes – control oocytes) was greatest at the channel's half-activation potential, and smaller when the protein was completely hyperpolarized (all channels closed) or depolarized (all channels open). This same trend in SEM was not observed in control oocytes, and can only be explained if the observed changes in effective dielectric were due to charge vibrations specific to the *Shaker* protein.

Cu^{2+} addition to the bath significantly changed steady-state RF impedance $|\Delta Z_{RF}|_s$ in *Sh*B-IR expressing oocytes relative to controls. In particular, data indicated that while a portion of the steady-state RF response may be caused by nonspecific binding of Cu^{2+} to the cell membrane, Cu^{2+} also binds specifically to the *Sh*B-IR protein and increases RF –evoked charge displacement during membrane depolarization. Analysis of the *Sh*B-IR expressing oocyte data showed that differences between Cu^{2+}-treated and nontreated cells were present at membrane potentials as low as -50 mV and increased with TEVC depolarization (Fig. 5.4A). The increase in RF response caused by Cu^{2+} - *Shaker* interaction occured even as ion-channel conduction current decreased (Fig. 5.4B). One possibility is that Cu^{2+} binding to the ion channel enhanced $|\Delta Z_{RF}|_s$ by increasing the effective charge moving within the transmembrane electric field and this thereby enhanced the signal arising from the RF-evoked protein vibration.

In addition to steady-state changes in RF charge displacement, rapid onset responses $|\Delta Z_{RF}|_o$ were detected during positive depolarizing steps ($dV_m/dt>0$) in both *Sh*B-IR expressing and control oocytes (see Fig. 5.2). Interestingly, the onset response was much larger and easily observable only for positive dV_m/dt. Hence, the onset RF data are not directly related to the traditional capacitive transient current evoked during voltage clamp. The present data were not adequate to analyze the decay time constant of the RF onset response in the *Sh*B-IR expressing cells due to the superimposition of the large RF response associated with the *Sh*B-IR channel activation. The magnitude of the transient response in both control and *Sh*B-IR expressing oocytes was comparable, showing the importance of endogenous mechanisms contributing to the RF onset response. This shows that the RF onset displacement currents measured here are not caused by the gating charge movement of *Shaker* channels. This was not surprising, due to the slow voltage clamp rise time in the present experiments. A faster voltage-clamp and RF recording system might allow future investigation of voltage-sensor displacement via RF interrogation. Even with the slow voltage-clamp used here, the onset response $|\Delta Z_{RF}|_o$ increased significantly in *Sh*B-IR expressing oocytes treated with Cu^{2+}. Data for *Shaker*-expressing cells in Fig. 5.5 were normalized to the same values as the steady-state figure, and show that $|\Delta Z_{RF}|_o$ in the Cu^{2+}-treated cells was 1.5 times as high as the values shown for the same copper-treated cells in the steady-state. One possible explanation for the large value of $|\Delta Z_{RF}|_o$ could be that the membrane-ion complex undergoes a nonequilibrium polarization when dV_m/dt is positive, compelling a brief period of enhanced dipole mobility. Previous studies on cation—protein interactions suggest that the cation applied to a protein may enter a transitional state during the onset of voltage-clamp (Abbruzzese *et al.*). A similar interaction between the Cu^{2+}—*Sh*B-IR channel could explain the amplified or augmented RF change measured during the onset period between Cu^{2+}–membrane–*Sh*B-IR interactions.

Although interpretation of the RF results can be challenging on the surface, this type of data cannot be obtained by traditional electrophysiological techniques and may prove useful in understanding membrane-bound protein dynamics. Present results show that the method can be used to track time- and voltage-dependent changes in RF charge displacement associated with membrane-bound ion-channel state/conformation and electrostatic binding of charged compounds. As such, the technique supplements conventional electrophysiological techniques and is suitable to examine voltage-dependent membrane-bound protein conformations and pharmacological interactions.

5.5 Methods

5.5.1 Oocyte Protein Expression

Xenopus oocytes were isolated at the University of Utah's Cardiovascular Research and Training Institute. cRNA encoding *Sh*B-IR was injected into oocytes 1-2 days before experimentation, to allow ample time for channel expression. Oocytes were stored in Superbarths oocyte media (88 mM NaCl, 1 mM KCl, 0.41 mM $CaCl_2$, 0.33 mM $Ca(NO_3)_2$, 1 mM $MgSO_4$, 2.4 mM $NaHCO_3$, 10 mM HEPES, 1 mM pyruvate and 50 μg/ml gentamicin, titrated using NaOH to a pH of 7.4) at 17° Celsius and ionic currents measured using two-electrode voltage clamp (TEVC) were used to verify channel expression.

5.5.2 Experimental Set-Up

An oocyte (~1.2 mm diameter) was positioned in a 1.2 mm recording chamber filled with Superbarths oocyte media surrounded by a 18 μm thick, gold-plated copper, effectively annular electrode (ORFLO, Woodinville, WA). Oocyte positioning and electrode stabilization were facilitated by a polycarbonate interface; the electrode was stabilized by two separate plates of the polycarbonate interface, and an oocyte was loaded into the recording chamber through a bowl-shaped well (Dharia & Rabbitt, 2010). Two glass micropipettes, used for two-electrode voltage clamp and filled with 3M KCl, were carefully placed in the oocyte using a 2X magnification lens on an upright microscope (AxioTech, Zeiss, Thornwood, NY). Each micropipette had a 0.5-2 MΩ access resistance, and were driven by a two-electrode amplifier (AxoClamp2B, Molecular Devices, Sunnyvale, CA) that controlled voltage-measuring (HS-2Ax1LU, Molecular Devices, Sunnyvale, CA) and current-injecting headstages (HS-2Ax10MGU, Molecular Devices, Sunnyvale, CA). An Ag/AgCl ground electrode was placed approximately 5 mm above the oocyte and immersed in media near the top of the recording chamber. This ground was common for both the RF recordings and TEVC. Photographs taken of the oocyte before and after experimentation were used to confirm minimal oocyte movement during recording (Q-Color3, Olympus, Center Valley, PA).

A ~ 120 μM Cu^{2+} solution (Copper ICP/DCP standard solution 10,000 μg/mL Cu^{2+}in 2% HNO_3, Sigma Aldrich, St. Louis, MO) was applied as an ion channel blocker to a small subset of the oocytes involved in experimentation. The Cu^{2+} solution was manually pipetted directly above the cell. The concentration of Cu^{2+} added was approximate, as it depended on the volume of Superbarths oocyte media in the recording chamber (~ 1.25 mL).

5.5.3 Recording

A 500 kHz radio frequency was passed from the gold-plated annular electrode to the ground electrode (Dharia & Rabbitt, 2010). Simultaneously, TEVC was used to control membrane potential (V_m^*, single-pole low pass filter, 30 kHz). Oocytes were held at -90 mV (holding potential) for 360 ms, and a voltage step was then applied for 40 ms. Nine different voltage steps were applied to the oocyte (-120 mV, -60 mV, -40 mV, -30 mV, -20 mV, -10 mV, 0 mV, 10 mV, 40 mV), and are collectively referred to as a voltage train. Voltage trains were applied to each cell 50 times. Voltage-clamp was automated using a software package designed for this purpose (Patchmaster, HEKA Inst., Bellmore, NY; Igor Pro, Wave Metrics, OR).

RF voltage drop across the recording chamber (V_{RF}) and RF current (I_{RF}) were monitored using an onboard reference impedance to track excitable membrane impedance changes ($Z_{RF}=V_{RF}/I_{RF}$). Head-stage amplification (OPA356, Texas Instruments, Dallas, TX), a 100 kHz high pass filter (48 dB/Oct Bessel HPF; SIM965, Stanford Research Systems, Sunnyvale, CA) and lock-in amplification (SR844, Stanford Research Systems, Sunnyvale, CA) were used to extract the RF component applied during TEVC. Voltage-clamp current and commands were low-pass filtered at <30 kHz to further ensure minimal cross-talk between the TEVC and RF recording systems. The quadrature lock-in signals, as well as TEVC ionic current, membrane potential and applied command potential were recorded through a 16-bit A/D converter (ITC-1600, HEKA Inst. Bellmore, NY). Patch-clamp software (Patchmaster, HEKA Inst., Bellmore, NY) sampled and saved data from each A/D channel at a rate of 20 µs. This voltage-clamp software in conjunction with the signal averaging time on the lock-in were the rate limiting factors for temporal resolution during RF interrogation. The technique, however, given the Nyquist frequency of the RF, has the potential to resolve events down to 4 µs.

5.5.4 Data Analysis

Data from individual oocytes were averaged over 50 command presentations (each consisting of 9 voltage levels, as described above). TEVC currents were leak compensated for each cell by assuming that currents measured during hyperpolarization were predominately caused by leak, and that these currents changed linearly with voltage. Leak-subtracted TEVC data for each oocyte were binned in 1 ms intervals in the time domain, and used to estimate *Sh*B-IR channel conductances (Ohm's law: $I_{TEVC}^* = G_{\mathit{SH}\text{B-IR}} (V_m^* - E_{rev})$). Capacitive transients were not subtracted. TEVC currents were plotted as a function of membrane potential, and current data (I^*) collected at $V_m^* > -10$ mV were linearly interpolated to 0 to estimate E_{rev}. Error between I and (V- E_{rev}) was then minimized by providing the best fits to a sigmoidal conductance ($I^* = G\left(V_m^* - E_{rev}\right)$, where $G = G_{\max} \Big/ \left(1 + e^{\left(V_{HA} - V_m^*\right)/\lambda}\right)$; $G_{\max}$ is the maximum whole-cell conductance of *Sh*B-IR expressing oocytes; V_{HA} is the half activation potential and λ is the rate of conductance rise). Channel conductance values were normalized to the maximum conductance value (G/G_{max}), and are shown as insets in Fig. 5.3 and 5.4.

Magnitude change in RF impedance ($|\Delta Z_{RF}|$, 500 kHz interrogation frequency) for each cell was calculated relative to the average RF impedance 5-35 ms before voltage command (holding potential ~=-90 mV). This was done in one millisecond bins. Temporally based comparisons of control *vs.* *Sh*B-IR cells and Cu^{2+} treated *vs.* nontreated oocytes (like in Fig. 5.2) were made by averaging data (TEVC current, TEVC voltage, $|\Delta Z_{RF}|$) across control oocytes (*n*=10), *Sh*B-IR expressing oocytes (consist of both endogenous and *Sh*B-IR protein, *n*=9), *Sh*B-IR expressing oocytes before/after Cu^{2+} treatment (*n*=4) and control oocytes before/after Cu^{2+} treatment (*n*=2). Voltage data were used to align voltage steps from individual cells in time to minimize jitter during averaging.

To facilitate comparisons across cells, the average value of $|\Delta Z_{RF}|$ was calculated for each cell at every voltage-step 1) 5-35 ms after the voltage step had been applied ($|\Delta Z_{RF}|_s$, dV_m^*/dt (voltage clamp) $\cong 0$, "steady state response") and 2) 0-1 ms after the voltage step had been applied ($|\Delta Z_{RF}|_o$, dV_m^*/dt (voltage clamp) $\neq 0$, "onset response"). To compensate for slight differences in TEVC membrane potential between individual cells, normalized RF data were linearly interpolated between voltages for each cell before averaging. Steady-state data were interpolated at the following membrane potential levels {-110 mV, -100 mV, -90 mV, -80 mV, -70 mV, -60 mV, -50 mV, -40 mV, -30 mV, -20 mV, -10 mV, 0 mV, 10 mV, 20 mV, 30 mV}. Onset response was plotted as a function of dV_m^*/dt, and results were interpolated to the following values {-12 mV/ms, -8 mV/ms, -4 mV/ms, 0 mV/ms, 4 mV/ms, 8 mV/ms, 12 mV/ms, 16 mV/ms, 20 mV/ms, 24 mV/ms, 28 mV/ms, 32 mV/ms, 36 mV/ms, 40 mV/ms, 44 mV/ms}.

The sample sizes used in the *Sh*B-IR cell (*n*=9) vs. control cell (*n*=10) experiment (exp1) allowed for direct (nonnormalized) comparison between both data sets, as it was assumed that the approximate shunt path associated with the *Sh*B-IR expressing oocytes was approximately equal across the populations (Fig. 5.3). Standard errors of the mean were calculated for both control and *Sh*B-IR expressing oocytes at specified membrane potentials (-110 mV, -100 mV, -90 mV, -80 mV, -70 mV, -60 mV, -50 mV, -40 mV, -30 mV, -20 mV, -10 mV, 0 mV, 10 mV, 20 mV, 30 mV). The *Sh*B-IR expressing oocytes consisted of RF responses from both endogenous proteins on the oocyte membrane and the exogenously expressed *Sh*B-IR protein (referred to as "*Sh*B-IR + Endo" in Fig. 5.3). The *Sh*B-IR and endogenous protein responses were assumed to be approximately independent, and the averaged control data (endogenous protein only, "Endo") was subtracted from the averaged *Sh*B-IR expressing oocyte data ("*Sh*B-IR + Endo", Fig. 5.3) to estimate the RF response associated with the *Sh*B-IR-protein-only (blue line, Fig. 5.3). Similarly, the standard error of the mean associated with the *Sh*B-IR protein-only was calculated by subtracting the SEM associated with control oocytes from the SEM associated with the *Sh*B-IR expressing oocytes (blue line, Fig. 5.3B).

The effects of Cu^{2+} application on both steady-state and transient RF impedance were compared for *Sh*B-IR expressing oocytes (*n*=4) and control oocytes (*n*=2, exp2). The small sample size prevented voltage-dependent population statistics for these controls, but we were able to make comparisons within cells. Data for each cell before/after copper treatment were normalized to the steady-state RF impedance value of that specific cell before Cu^{2+} treatment at +30 mV. After normalization, data for each group (Control-untreated/treated, *Sh*B-IR-untreated/treated) were averaged together, and the effects of Cu^{2+} before/after treatment were compared within each cell expression system. Control data (both before/after copper treatment) were scaled by the ratio between the control cells and *Sh*B-IR cells at +30 mV from the previous experiment (larger sample sizes, Fig. 5.3). This scaling enabled comparisons between the control cell data and the *Sh*B-IR cell data before/after copper treatment. Standard errors of the mean were calculated for *Sh*B-IR expressing oocytes at specified membrane potentials (-110 mV, -100 mV, -90 mV, -80 mV, -70 mV, -60 mV, -50 mV, -40 mV, -30 mV, -20 mV, -10 mV, 0 mV, 10 mV, 20 mV, 30 mV). SEM was not calculated for control cells, due to the small (< 2) sample size.

In exp1, data at each voltage for both the control and *Sh*B-IR expressing cells were not normally distributed, due to differences in shunt path between cells and differences in exogenous protein expression level on the *Sh*B-IR expressing oocytes. As such, a Mann-Whitney nonparametric statistical test was used to compare control vs. *Sh*B-IR expressing oocyte data (exp1) at each of the sampled voltage levels (the median of the sample values were slight lower than the averages shown in Fig. 5.3A, although the trends were similar). The null hypothesis (H_0) for this comparison was that the RF data for the *Sh*B-IR cells before copper treatment are the same as the RF data for the *Sh*B-IR expressing oocytes after copper treatment at a specified voltage level. The linear correlation coefficient between *Sh*B-IR conductance and the subtracted *Sh*B-IR-only response was calculated both between -110 mV and 30 mV and between -45 and 2 mV (the regime where the RF *Sh*B-IR-only response increased from 5-95% of its final value).

In exp2, the sample size of the *Sh*B-IR expressing oocytes (*n*=4) before/after Cu^{2+} treatment was too small to apply the Mann-Whitney test at every voltage level (requires a total sample size of 10). Instead, all the normalized data sampled from cells above -60 mV (where the channel begins to activate) were pooled, and these pooled samples were compared before/after copper treatment using the Mann-Whitney test (the pooled voltage levels for each group of cells was the same). This allowed for a significance test between the two treatment groups of cells, with the null hypothesis (H_0) that the RF data for the

*Sh*B-IR cells before copper treatment are the same as the RF data for the *Sh*B-IR expressing oocytes after copper treatment.

5.6 Acknowledgements

M. Sanguinetti (CVRTI, Univ. Utah) provided *Xenopus* oocytes. C. King and H.E. Ayliffe (ORFLO Technologies) assisted in the fabrication of the electrodes used in RF recording.

Fig. 5.1 – Set-up and Circuit Model **-** A) Changes in RF membrane impedance ($|\Delta Z_{RF}|$) during TEVC were measured by passing RF current from an electrode surrounding the meridian of the cell (black) to a ground electrode (media, above the cell). Contour lines and colors in the saggital cross-section of a cell in the recording chamber, shown here, illustrate the general spatial distribution of the RF electric potential expected based on the Maxwell equations for a passive cell under axisymmetric conditions ($\pi/4$ phase shown). B) A circuit model of the chamber including the shunt resistance ($R_{s,}$), membrane impedance (Z_m), intracellular resistance (R_i) and electrode double layer (Z_{dl}). C) Using the circuit model, the frequency-dependent RF impedance would change ($\Delta|Z_{RF}|$) with an increase or decrease in membrane capacitance -- a change that would be most easily detectable at frequency ω^* where the maxima of the $|\Delta Z_{RF}|$ occurs. The present study reports changes in RF impedance $|\Delta Z_{RF}|$ evoked by TEVC step changes in membrane potential.

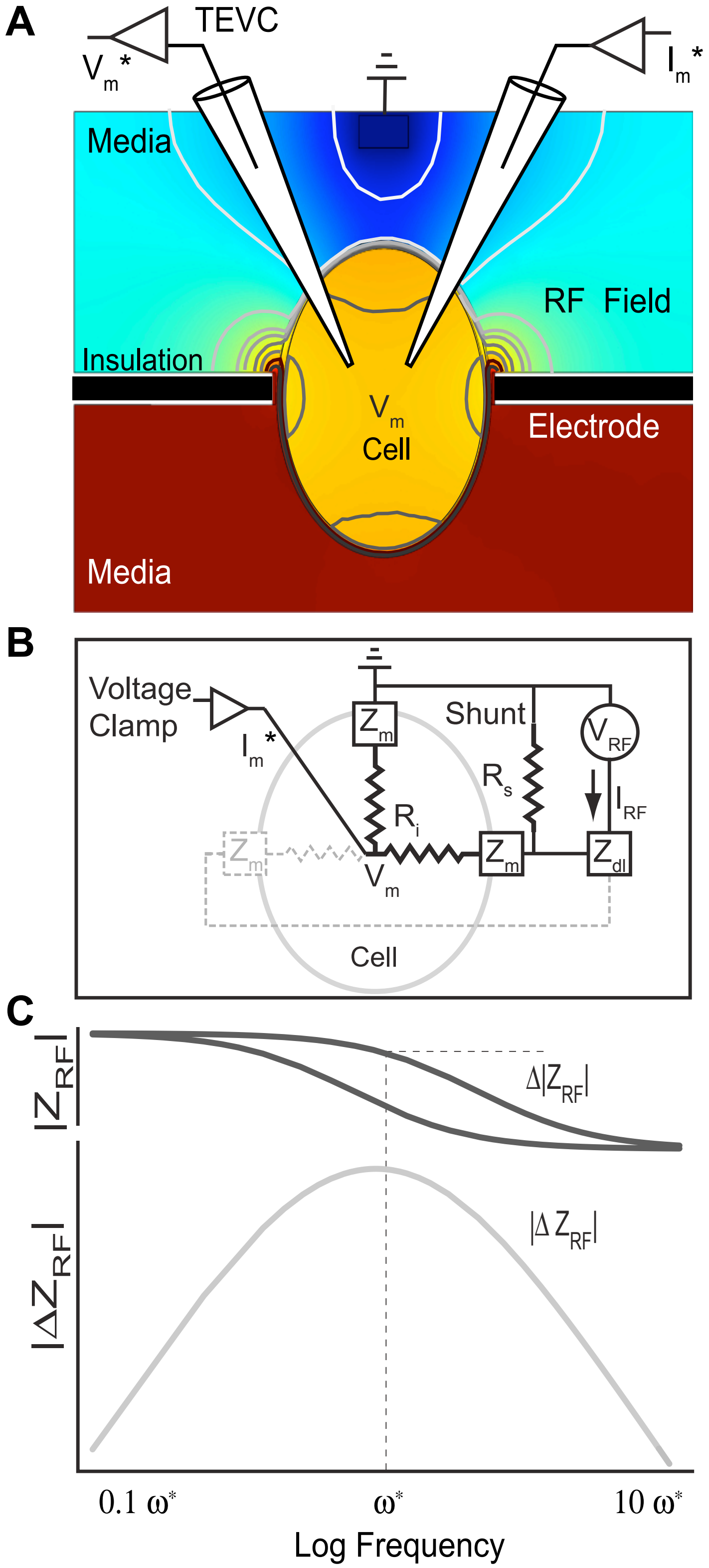
A
TEVC
V_m*
I_m*
Media
RF Field
Insulation
V_m
Cell
Electrode
Media
B
Voltage
Clamp
I_m*
Z_m
Shunt
V_{RF}
R_s
I_{RF}
R_i
Z_m
Z_m
Z_{dl}
V_m
Cell
C
$|Z_{RF}|$
$\Delta|Z_{RF}|$
$|\Delta Z_{RF}|$
$|\Delta Z_{RF}|$
0.1 ω*
ω*
10 ω*
Log Frequency

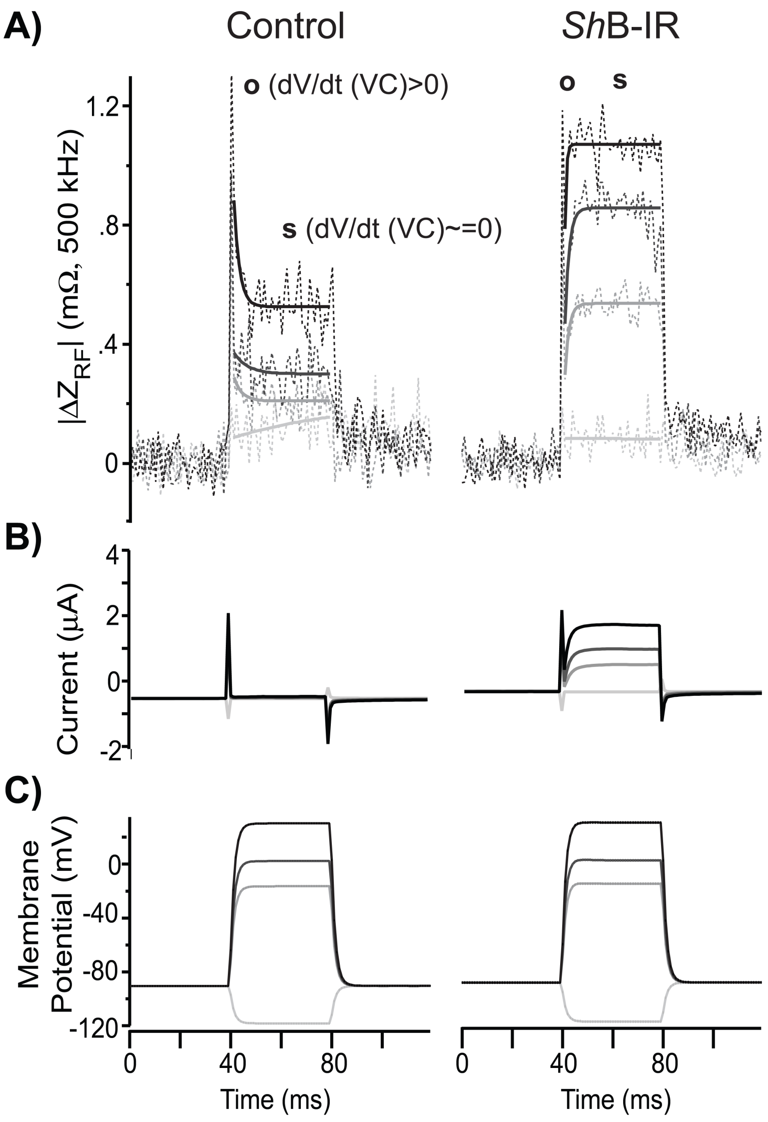

Fig. 5.2 – Temporally Resolved RF Measurements **-** A) RF impedance changes ($|\Delta Z_{RF}|$) measured during TEVC relative to the impedance at holding potential (-90 mV) in control oocytes, expressing endogenous proteins only ("Endo", *n*=10, left column) and *Sh*B-IR expressing oocytes (*n*=9, right column). *Sh*B-IR expressing oocytes (*n*=9, right column) elicited a membrane-potential-dependent (V_m^*) RF response different than control oocytes (*n*=10, left column, endogenous protein expression only). RF impedance changes were analyzed in two regions; the RF response during the onset of voltage-step (**o**, average $|\Delta Z_{RF}|_o$ 0-1 ms after voltage step, $dV_m^*/dt > 0$) and the RF response after membrane potential achieved its command (steady-state) level (**s**, average $|\Delta Z_{RF}|_s$ 5-35 ms after voltage step, $dV_m^*/dt \cong 0$). B) TEVC current measurements were used to verify ion channel expression and responses (leak current subtracted, capacitive transient unsubtracted) to C) whole-cell voltage-clamp.

Fig. 5.3 – Steady-state RF Response for *Sh*B-IR and Control Cells - A) Voltage-dependent differences in $|\Delta Z_{RF}|_s$ were observed between control oocytes, expressing endogenous proteins only ("Endo", orange), and *Sh*B-IR (brown) expressing oocytes (that express both endogenous and *Sh*B-IR proteins, "*Sh*B-IR + Endo", Fig. 5.3A, ^{x}p=.1, $^{*}p$=.05). The "Endo" response was subtracted from the "*Sh*B-IR + Endo" response to estimate the isolated RF response from the *Sh*B-IR channels (blue line). Error bars denote +/- standard errors of the mean (SEM). B) The SEM for the isolated *Sh*B-IR proteins (blue) was also estimated by subtracting the SEM from the Endo oocytes (orange line) from those associated with the *Sh*B-IR expressing oocytes ("*Sh*B-IR + Endo" response, brown line). The SEM for isolated *Sh*B-IR expressing oocytes was largest near the half-activation potential for these ion channels. C) *Sh*B-IR channel expression and voltage-dependent whole-cell current was verified using TEVC, and this data was used to estimate *Sh*B-IR conductance (G/G_{max}, inset).

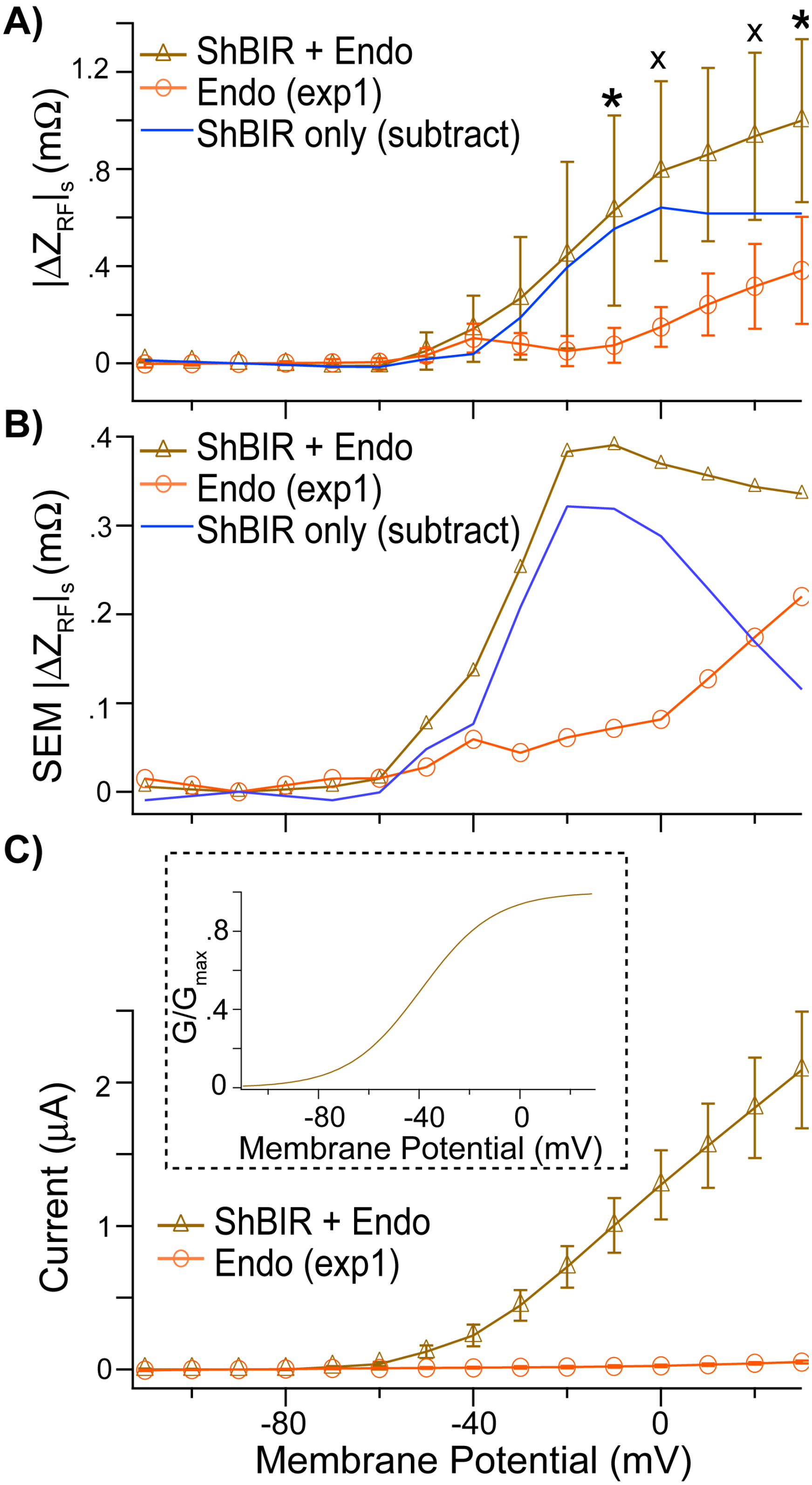
A)
B)
C)
ShBIR + Endo
Endo (exp1)
ShBIR only (subtract)
$|\Delta Z_{RF}|_s$ (mΩ)
SEM $|\Delta Z_{RF}|_s$ (mΩ)
Current (µA)
G/G$_{max}$
Membrane Potential (mV)
1.2
.8
.4
0
.3
.2
.1
2
1
-80
-40
0
*
x
x
*

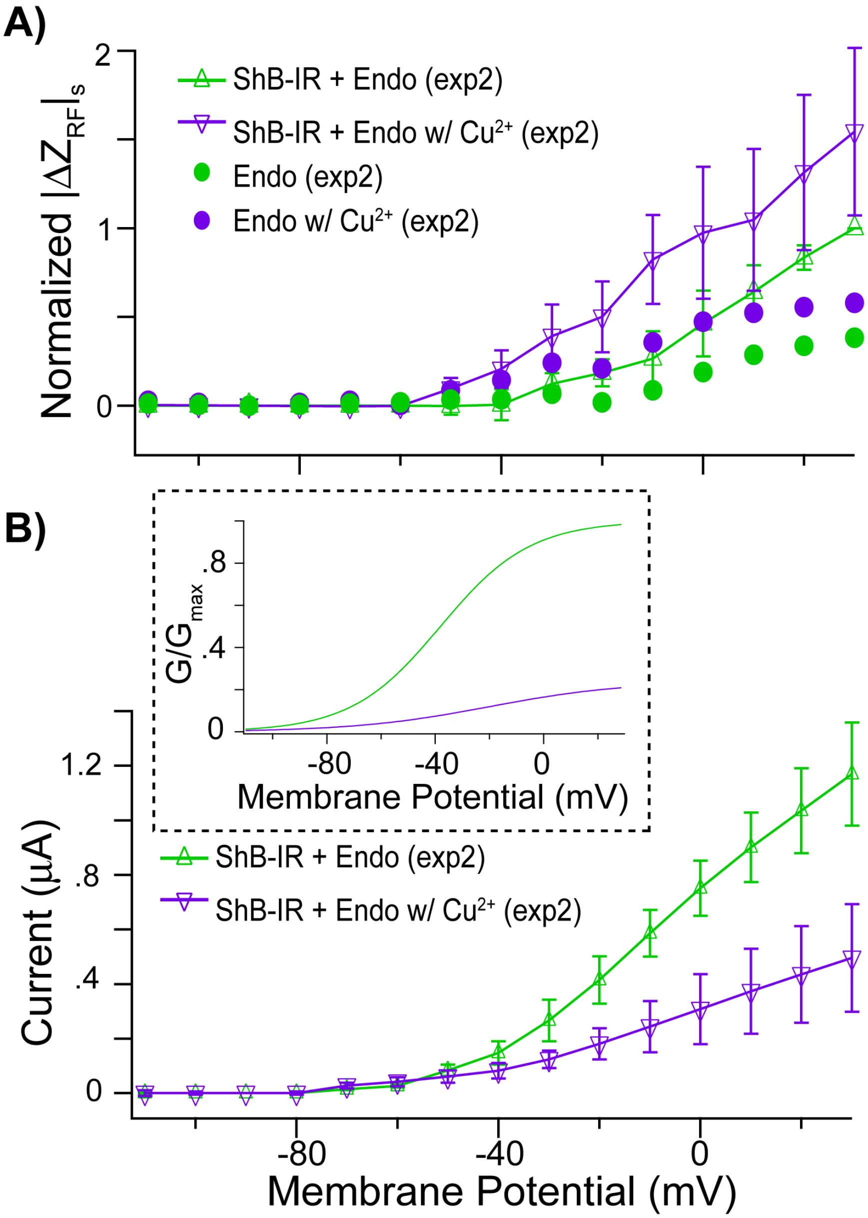

Fig. 5.4 – Copper Treatment and Steady-State *Sh*B-IR RF Response **-** A) *Shaker* expressing oocytes ("*Sh*B-IR + Endo", green line) and to a lesser extent, control cells ("Endo", green markers), showed voltage-dependent differences in $|\Delta Z_{RF}|_s$ when compared with the same cells exposed to ~120 µM Cu^{2+} in the bath (purple). Error bars denote +/- standard errors of the mean (SEM). B) Even though RF charge displacements increased in Cu^{2+}-exposed *Sh*B-IR expressing oocytes, TEVC whole-cell current decreased showing that Cu^{2+} successfully blocked the channels (channel conductance shown as inset).

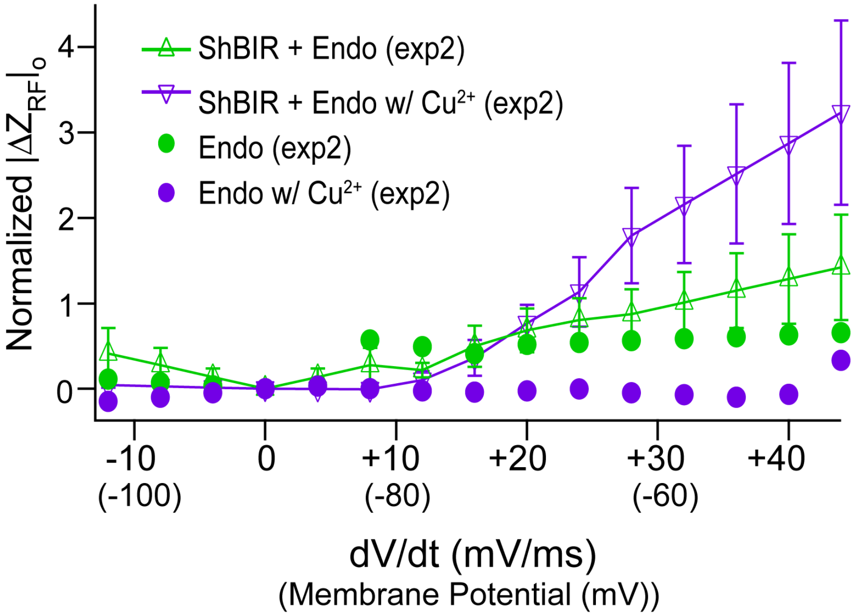

Fig. 5.5 – Onset RF Response in *Sh*B-IR Expressing Oocytes - Changes in RF impedance during the onset of voltage-clamp ($|\Delta Z_{RF}|_o$ 0-1 ms after whole-cell depolarization) were slightly depressed in control oocytes with the addition of Cu^{2+} (Cu^{2+}-free - green symbol, Cu^{2+} addition - purple symbols), but were significantly greater in *Sh*B-IR expressing oocytes (Cu^{2+}-free - green line, Cu^{2+} addition - purple line).

CHAPTER 6

CONCLUSION

6.1 Summary

Major contributions of this thesis include 1) a method to simultaneously estimate chamber and double-layer impedances in a linear regime of electrode voltage–current sensitivity, 2) a platform and algorithm to spatially resolve and visualize the dielectric properties around a single cell and 3) the design and implementation of a system to temporally resolve changes in RF impedance around a *Xenopus* oocyte during whole-cell voltage-clamp. The latter system has been used to track excitable changes in integral membrane protein activity as well as monitor membrane-potential-dependent externally applied molecule–protein interactions. These contributions will result in one patent, two peer-reviewed journal publications and one peer-reviewed conference proceeding. Furthermore, different facets of this work have been presented via poster- and podium-presentations at 18 conferences. A brief overview, list of specific contributions and future work associated with each major contribution are summarized here.

6.1.1 The Three Current-Passing Electrode Method (TCPE)

Chapter 2 introduced a new method, TCPE, which could be used to simultaneously estimate electrode–electrolyte interfacial impedances and interelectrode (chamber) impedances in a linear regime of electrode voltage–current sensitivity. Three current-passing electrodes were selected for TCPE recordings. Double-layer impedances were assigned to each individual electrode interface, while localized chamber impedances were assigned to the space between each pair of electrodes. Localized chamber and double-layer impedance parameters were estimated by minimizing error between six electrical lumped-parameter models, used to represent different electrode recording configurations using the three selected electrodes, and corresponding simulated noisy measurements. Parameter estimation accuracy was sensitive to measurement noise, error in the least-squares parameter guess, and the average ratio of chamber to double-layer impedance. However, preliminary data revealed averaged parameter estimates from multiple applications of TCPE converged to within a conventionally acceptable range (within ~10%) of actual parameter values, and indicate the potential utility of this technique.

While additional simulations and experiments are needed to ensure TCPE accuracy, this method might offer one of the only solutions to the double-layer estimation challenge that accounts for time and material dependencies associated with the electrode interface; other conventional double-layer estimation techniques, that utilize multiple calibration solutions or moveable electrode architectures, cannot do this. Furthermore, TCPE could potentially also be used to estimate chamber impedances in cases where the four-electrode method is not feasible; this may be true, for example, in a size-constrained system, a system with material-based fabrication limitations or a system where high-input impedance electrodes are difficult to achieve. As such, TCPE could significantly contribute to many electrode-in-electrolyte recording techniques, including those based in electric impedance tomography and electric impedance spectroscopy.

6.1.2 Monitoring Spatially Resolvable Differences in Membrane Dielectric

Chapter 3 introduced a technique that used localized RF impedance measurements between adjacent electrodes around a single cell to map 1) the position of the cell in the recording chamber (correlated with the real portion of the complex-valued impedance) and 2) the relative RF dielectric of the cell membrane (corresponded to the imaginary portion of the complex-valued impedance). The proof-of-concept of this technique was validated using *Xenopus* oocytes, and the current platform is best-suited to millimeter-diameter cellular recordings. As such, the current platform might be used to monitor RF impedance changes in the oocyte membrane during maturation or noninvasively identify success of oocyte protein transfection.

However sce-Topo recordings are not limited to millimeter-sized cells, as the technique and associated algorithms are scalable; as such, the sce-Topo platform could be miniaturized using MEMS-based fabrication processes to produce spatially resolved dielectric images around micron-sized cells. Spatial resolution increases with electrode number, and the use of electron-beam lithography for electrode fabrication on a miniaturized platform could enable effective dielectric feature-size detection of ~30 nm (Broers, 1995). This might allow for visualization of localized liquid-ordered lipid domains (‘lipid rafts’, 25 nm – 700 nm diameters), and sce-Topo could potentially elucidate lipid-raft distribution, movements and associated signal-transduction processes (McLaughlin & Aderem, 1995; Brown & London, 1998; Munro, 2003).

6.1.3 Monitoring RF-Impedance Changes of *Shaker*B-IR Proteins Expressed in *Xenopus* Oocytes

Chapter 4 and 5 introduced a new technique that enabled RF impedance measurement around *Xenopus* oocytes during two-microelectrode voltage-clamp. It was hypothesized that a RF signal will vibrate charges on the membrane, and a change in membrane-potential-dependent ion-channel configuration would manifest as a change in measured RF impedance. Simulations and preliminary recordings performed on the platform (Chapter 4) indicated that changes in oocyte membrane RF capacitance are detectable within a narrow 100 kHz – 1 MHz bandwidth. As such, a 500 kHz interrogation frequency was used to temporally resolve (20 µs resolution) RF impedance changes associated with both native *Xenopus* oocytes and those expressing *Shaker*B-IR ion-channels during whole-cell voltage-clamp (Chapter 5). Cu^{2+} was applied to a subset of the *Shaker*B-IR expressing oocytes, and data indicated that RF impedance measurement 1) correlated with ion-channel activity, 2) reflected more than ionic conduction, 3) were sensitive to Cu^{2+}–*Shaker*B-IR–complex interactions and 4) could be used to temporally resolve excitable changes in Cu^{2+}–*Shaker*B-IR vibration.

While additional experiments on other *Shaker* channel variants should be done to identify the exact source of the RF-response measured here, the data generally suggest that this technology could be used to 1) to identify charge-based transitions associated with ion-channel conformation, 2) monitor changes in molecule-protein charge:size:mobility ratio and 3) temporally resolve excitatory charge-based activity associated with a cell membrane. In this sense, the technology presented here could contribute to both basic membrane biophysics and the pharmaceutical industry.

6.2 Final Conclusions

Overall, the work presented in this dissertation uses RF impedance measurements, associated with membrane-bound charge vibration, to elucidate 1) charge movement associated with ion-channel conformational state transitions, 2) localized changes in membrane dielectric, 3) charged-cation–membrane binding processes and 4) size:charge:mobility ratio associated with specified proteins or molecules in the cell membrane. Furthermore, this technology could potentially also be used monitor other charge-changing processes associated with the cell membrane including 1) phospholipid head group rotations, 2) signal transduction processes associated with membrane–charged-biomolecule binding events (e.g. G-proteins, viruses etc.), 3) exo- or endo- cytotic activity around a cell and 4) charged-molecule (could be a cation, drug etc.)—membrane binding processes. A new method, TCPE, also presented as part of this dissertation, might not only facilitate these RF recordings, but also those performed during any other electric impedance spectroscopic or electric impedance tomographic recording; unlike any other conventional method, TCPE enables simultaneous estimation of both absolute chamber and double-layer impedance values in a linear regime of electrode voltage–current sensitivity. As such, each technology presented in this dissertation could greatly increase our understanding of cellular biophysics and might eventually help identify pharmacological or clinical membrane pathologies.

REFERENCES

Axon Instruments Inc. (1997). *Axoclamp 2B Manual: Microelectrode Clamp Theory and Operation.* Axon Instruments Inc.

Abbruzzese J, Sachse FB, Tristani-Firouzi M & Sanguinetti MC. Modification of hERG1 channel gating by Cd2+. *J Gen Physiol* **136,** 203-224.

Alvarez O & Latorre R. (1978). Voltage-dependent capacitance in lipid bilayers made from monolayers. *Biophys J* **21,** 1-17.

Armstrong C & Bezanilla F. (1974). Charge movement associated with the opening and closing of the activation gates of the Na channels. *The Journal of General Physiology* **63,** 533-552.

Armstrong C & Bezanilla F. (1977a). Inactivation of the Sodium Channel, II. Gating current Experiments. *The Journal of General Physiology* **70,** 567-590.

Armstrong CM & Bezanilla F. (1977b). Inactivation of the sodium channel. II. Gating current experiments. *J Gen Physiol* **70,** 567-590.

Ayliffe H, Frazier B & Rabbitt R. (1999). Electric impedance spectroscopy using microchannels with integrated metal electrodes. *IEEE Journal of Microelectromechanical Systems* **8,** 50-57.

Bard A & Faulkner L. (2001). *Electrochemical Methods: Fundamentals and Applications (Second Edition)*. John Wiley and Sons, Inc., New York.

Barnes F. (2006). Chapter 2. In *Handbook of Biological Effects of Electromagnetic Fields: Bioengineeing and Biophysical Aspects of Electromagnetic Fields*
, ed. Barnes F & Greenebaum B, pp. 119. CRC Press.

Bartholomeusz D, Boutte R & Andrade J. (2005). Xurography: rapid prototyping of microstructures using a cutting plotter. *Journal of Microelectromechanical Systems* **14,** 1364-1374.

Bayford RH. (2006). Bioimpedance tomography (electrical impedance tomography). *Annu Rev Biomed Eng* **8,** 63-91.

Bezanilla F. (2000a). The voltage sensor in voltage-dependent ion channels. *Physiological Reviews* **80,** 555-592.

Bezanilla F. (2000b). The voltage sensor in voltage-dependent ion channels. *Physiol Rev* **80,** 555-592.

Bezanilla F. (2005). Voltage-gated ion channels. *IEEE Transactions on NanoBioscience* **4,** 34-48.

Bezanilla F & Armstrong C. (1977). Inactivation of the Sodium Channel. *The Journal of General Physiology* **70,** 549-566.

Bezanilla F & Stefani E. (1998). Gating currents. *Methods Enzymol* **293,** 331-352.

Boer RW & Oosterom Av. (1978). Electrical properties of platinum electrodes: impedance measurements and time-domain analysis. *Med & Biol Eng & Comput* **16,** 1-10.

Branden M, Sanden T, Brzezinski P & Widengren J. (2006). Localized proton microcircuits at the biological membrane-water interface. *Proc Natl Acad Sci U S A* **103,** 19766-19770.

Brayford RH. (2006). Bioimpedance Tomography (Electrical Impedance Tomography). *Annu Rev Biomed Eng* **8,** 63-91.

Broers AN. (1995). Fabrication Limits of Electron Beam Lithography and of UV, X-Ray and Ion-Beam Lithographies. *Philosophical Transactions: Physical Sciences and Engineering* **353,** 291-311.

Brown BH. (2003a). Electrical impedance tomography (EIT): a review. *Journal of Medical Engineering and Technology* **27,** 97-108.

Brown BH. (2003b). Electrical impedance tomography (EIT): a review. *Journal of Medical Engineering & Technology* **27,** 97-108.

Brown D & London E. (1998). Structure and origin of ordered lipid domains in biological membranes. *J Membrane Biol* **164,** 103-114.

Cahalan M & Neher E. (1992a). Methods in Enzymology. pp. 3-14. Academic Press Inc.

Cahalan M & Neher E. (1992b). Patch clamp techniques: an overview. *Methods Enzymol* **207,** 3-14.

Cha A & Bezanilla F. (1997). Characterizing Voltage-Dependent Conformational Changes in the Shaker K+ Channel with Fluorescence. *Neuron* **19,** 1127-1140.

Chang P, Perez-Mongiovi D & Houliston E. (1999). Organization of Xenopus Oocyte and Egg Cortices. *Microscopy Research and Technique* **44,** 415-429.

Chapra SC & Canale RP. (2002). *Numerical Methods for Engineers (Fifth Edition)*. McGraw Hill, New York.

Cheung K, Gawad S & Renaud P. (2005). Impedance spectroscopy flow cytometry: On-chip label-free cell differentiation. *Cytometry Part A* **65A,** 124-132.

Cole. (1968). *Membranes, ions and impulses, a chapter of classical biophysics*. University of California Press.

Conti F & Stuhmer W. (1989). Quantal charge redistributions accompanying the structural transitions of sodium channels. *Eur Biophys J* **17,** 53-59.

Corless JM, McCaslin DR & Scott BL. (1982). Two-dimensional rhodopsin crystals from disk membranes of frog retinal rod outer segments. *Proc Natl Acad Sci U S A* **79,** 1116-1120.

Coulter W & Rodriguez C. (1988). Particle analyzer for measuring the resistance and reactance of a particle. Coulter Electronics Inc., United States.

Cui XY & Martin DC. (2003). Electrochemical deposition and characterization of poly(3,4-ethylenedioxythiophene) on neural microelectrode arrays. *Sensors and Actuators B-Chemical* **89,** 92-102.

Dascal N. (1987). The use of *Xenopus* Oocytes for the study of ion channels. *CRC Critical Reviews in Biochemistry* **22,** 317-387.

Dharia S, Ayliffe HE & Rabbitt RD. (2009). Single cell electric impedance topography: Mapping membrane capacitance. *Lab Chip* **9,** 3370-3377.

Dharia S & Rabbitt R. (2010). Monitoring Voltage-Sensitive Membrane Impedance Change Using Radio Frequency Interrogation. In *32nd Annual International IEEE EMBS Conference*, ed. Lovell N. Buenos Aires Sheraton Hotel, Buenos Aires, Argentina.

Dharia S & Rabbitt R. (Submitted). Monitoring Voltage-dependent Charge Displacement of Shaker B-IR K+ Ion Channels Using Radio Frequency Interrogation
. *Submitted, PLoS-ONE*.

Dittami G, Ayliffe H, King C & Rabbitt R. (2008). A mulitlayer MEMS platform for single-cell electric impedance spectroscopy and electrochemical analysis. *JMEMS* **17**.

Ehret R, Baumann W, Brischwein M, Schwinde A, Stegbauer K & Wolf B. (1997). Monitoring of cellular behaviour by impedance measurements on interdigitated electrode structures. *Biosensors and Bioelectronics* **12,** 29-41.

Elinder F & Arhem P. (2004). Metal ion effects on ion channel gating. *Quarterly Reviews of Biophysics* **36,** 373-427.

Epstein FH, Ackerman MJ & Clapham DE. (1997). Ion Channels - Basic Science and Clinical Disease. *New England Journal of Medicine* **336,** 1575-1586.

Foster K & Schwan H. (1989). Dielectric properties of tissues and biological materials: A critical review. *Critical Reviews in Biomedical Engineering* **17,** 25-103.

Franks W, Schenker I, Schmutz P & Hierlemann A. (2005). Impedance characterization and modeling of electrodes for biomedical applications. *IEEE Trans Biomed Eng* **52,** 1295-1302.

Gawad S, Cheung K, Seger U, Bertsch A & Renaud P. (2004). Dielectric spectroscopy in a micromachined flow cytometer: theoretical and practical considerations. *Lab on a Chip* **4,** 241-251.

Gawad S, Schild L & Renaud P. (2001). Micromachined impedance spectroscopy flow cytometer for cell analysis and particle sizing. *Lab on a Chip* **1,** 76-82.

Geddes L. (1972). *Electrodes and the measurement of bioelectric events*. Wiley-Interscience, New York, London, Sydney, Toronto.

Geddes L. (1997). Historical evolution of circuit models for the electrode-electrolyte interface. *Annals of Biomedical Engineering* **25,** 1-14.

Gierhart BC, Howitt, D., Chen, S., Zhu, Z., Kotecki, D., Smith, R., Collins, S. (2008). Nanopore with transverse nanoelectrodes for electrical characterization and sequencing of DNA. *Sensors and Actuators B* **132,** 593-600.

Giordano BC, Ferrance J, Swedberg S, Huhmer AF & Landers JP. (2001). Polymerase chain reaction in polymeric microchips: DNA amplification in less than 240 seconds. *Anal Biochem* **291,** 124-132.

Glauner K, Mannuzzu L, Gandhi C & Isacoff E. (1999). Spectroscopic mapping of voltage sensor movement in the Shaker potassium channel. *Nature* **402,** 813-817.

Goettsche T, Ruddy C, Heller U, Stehr M, Ashauer H, Lindemann T, Koltay P, Yu Y, Peters R, Soriani P & Bellone A. (2007). Comparison of bonding procedures for 3D-structured polyimide films on silicon subtrates applies to ink-jet cartridges. *Int J Adv Manuf Technol* **33,** 191-197.

Gomez-Hernandez J-M, Stuhmer W & Parekh A. (1997). Calcium dependence and distribution of calcium-activated chloride channels in *Xenopus* oocytes. *Journal of Physiology* **502,** 569-574.

Gritsch S, Nollert P, Jahnig F & Sackmann E. (1998). Impedance spectroscopy of porin and gramicidin pores reconstituted into supported lipid bilayers on indium-tin-oxide electrodes. *Langmuir* **14,** 3118-3125.

Han A & Frazier AB. (2006). Ion channel characterization using single cell impedance spectroscopy. *Lab on a Chip* **6,** 1412-1414.

Han A, Wang O, Graff M, Mohanty S, Edwards T, Han K-H & Frazier AB. (2003a). Multi-layer plastic/glass microfluidic systems containing electrical and mechanical functionality. *Lab on a Chip* **3,** 150-157.

Han AR, Wang O, Graff M, Mohanty SK, Edwards TL, Han KH & Frazier AB. (2003b). Multi-layer plastic/glass microfluidic systems containing electrical and mechanical functionality. *Lab on a Chip* **3,** 150-157.

Han K-H, Han A & Frazier AB. (2006). Microsystems for isolation and electrophysiological analysis of breast cancer cells from blood. *Biosensors and Bioelectronics* **21,** 1907-1914.

Heidelberger R, Heinemann C, Neher E & Matthews G. (1994). Calcium dependence of the rate of exocytosis in a synaptic terminal. *Nature* **371,** 513-515.

Hille B. (2001). *Ion Channels of Excitable Membranes, Third Edition*. Sinauer Associates, Inc., Sunderland, Massachusetts, USA.

Hoffman RA & Britt WB. (1979). Flow-system measurement of cell Iimpedance properties. *The Journal of Histochemistry and Cytochemistry* **27,** 234-240.

Holmes D & Morgan H. (2003). Impedance based single cell detection using resonance frequency interrogation. In *7th International Conference on Miniaturized Chemical and Biochemical Analysis Systems*, pp. 1239-1242. Squaw Valley, CA.

Hoshi T, Zagotta W & Aldrich R. (1990). Biophysical and molecular mechanisms of Shaker potassium channel inactivation. *Science* **250,** 533-538.

Hoshi T, Zagotta W & Aldrich R. (1991). Two types of inactivation in Shaker K+ channels: Effects of alterations in the carboxy-terminal region. *Neuron* **7,** 547-556.

Huang Y, Wang X-B, Gascoyne P & Becker F. (1999). Membrane dielectric responses of human T-lymphocytes following mitogenic stimulation. *Biochimica et Biophysica Acta* **1417,** 51-62.

Hubner C & Jentsch T. (2002). Ion channel diseases. *Human Molecular Genetics* **11,** 2435-2445.

Ilic B, Czaplewski D, Neuzil P, Stanczyk T, Blough J & Maclay G. (2000). Preparation and characterization of platinum black electrodes. *Journal of Materials Science* **35,** 3447-3457.

Islas LD & Sigworth FJ. (1999). Voltage sensitivity and gating charge in Shaker and Shab family potassium channels. *J Gen Physiol* **114,** 723-742.

Iverson L & Rudy B. (1990). The role of the divergent amino and carboxyl domains on the inactivation properties of potassium channels derived from the Shaker gene of *Drosophila*. *The Journal of Neuroscience* **10,** 2903-2916.

Jaffe L & Nuccitelli R. (1974). An ultrasensitive vibrating probe for measuring steady extracellular currents. *The Journal of Cell Biology* **63,** 614-628.

Kaczorowski G, McManus O, Priest B, Garcia M, Rhodes K, Trimmer J, Sack J, Shamotienko O, Dolly O, Lundbaed J, Tucker S & Baukrowitz T. (2008). Perspectives on How to Drug an Ion Channel. *J Gen Physiol* **131,** 395-397.

Kalinowski S & Figaszewski Z. (1995). A four-electrode potentiostat-galvanostat for studies of bilayer lipid membranes. *Measurement Science and Technology* **6,** 1050.

Keese C & Giaever I. (1994). A biosensor that monitors cell morphology with electric fields. *IEEE Engineering in Medicine and Biology*, 402-408.

Ladha S. (1998). Lipid Heterogeneity and Membrane Fluidity in a Highly Polarized Cell, the Mammalian Spermatozoon. *Journal of Membrane Biology* **165,** 1-10.

Lehmann-Horn F & Jurkat-Rott K. (1999). Voltage-gated ion channels and hereditary disease. *Physiol Rev* **79,** 1317-1372.

Li X-A, Everson WV & Smart EJ. (2005). Caveolae, Lipid Rafts, and Vascular Disease. *Trends in Cardiovascular Medicine* **15,** 92-96.

Liu Y, Jurman ME & Yellen G. (1996). Dynamic rearrangement of the outer mouth of a K+ channel during gating. *Neuron* **16,** 859-867.

Lo C-M, Keese C & Giaever I. (1995). Impedance analysis of MDCK cells measured by electric cell-subtstrate impedance sensing. *Biophysical Journal* **69,** 2800-2807.

Loots E & Isacoff E. (1998). Protein rearrangements underlying slow inactivation of the Shaker K+ channel. *J Gen Physiol* **112,** 377-389.

Ma Z, Wong KY & Horrigan FT. (2008). An extracellular Cu2+ binding site in the voltage sensor of BK and Shaker potassium channels. *J Gen Physiol* **131,** 483-502.

Malinska K, Malinsky J, Opekarova M & Tanner W. (2003). Visualization of Protein Compartmentation within the Plasma Membrane of Living Yeast Cells. *Mol Biol Cell* **14,** 4427-4436.

McLaughlin S & Aderem A. (1995). The myristoyl-electrostatic switch: a modulator of reversible protein-membrane interactions. *Trends in Biochemical Sciences* **20,** 272-276.

Mirtaheri P, Grimnes S & Martinsen O. (2005). Electrode polarization impedance in weak NaCl aqueous solutions. *IEEE Transactions on Biomedical Engineering* **52,** 2093-2099.

Moss ED, Han A & Frazier AB. (2007). A fabrication technology for multi-layer polymer-based microsystems with integrated fluidic and electrical functionality. *Sensors and Actuators B-Chemical* **121,** 689-697.

Munro S. (2003). Lipid rafts: elusive or illusive? *Cell* **115,** 377-388.

Onoral B & Schwan H. (1982). Linear and nonlinear properties of platinum electrode polarization. Part 1: frequency dependence at very low frequencies. *Med & Biol Eng & Comput* **20,** 299-306.

Paul B & Peterson R. (1999). Microlamination for microtechnology-based energy, chemical and biological systems. In *ASME International Mechanical Engineering Congress and Exposition*, pp. 45-52. AES, Nashville, TN.

Pearce T, Wilson JA, Oakes SG, Chiu S-Y & Williams J. (2005). Integrated microelectrode array and microfluidics for temperature clamp of sensory neurons in culture. *Lab on a Chip* **5,** 97-101.

Perozo E, MacKinnon R, Bezanilla F & Stefani E. (1993). Gating currents from a nonconducting mutant reveal open-closed conformations in Shaker K+ channels. *Neuron* **11,** 353-358.

Pethig R. (1979). *Dielectric and electronic properties of biological materials.* John Wiley and Sons, Chichester, New York, Brisbane, Toronto.

Petrov AG. (2002). Flexoelectricity of model and living membranes. *Biochim Biophys Acta* **1561,** 1-25.

Piepenhagen PA & Nelson WJ. (1998). Biogenesis of polarized epithelial cells during kidney development in situ: roles of E-cadherin-mediated cell-cell adhesion and membrane cytoskeleton organization. *Mol Biol Cell* **9,** 3161-3177.

Polk C & Postow E. (1996). *Handbook of biological effects of electromagnetic fields*. CRC Press, Boca Raton, New York, London, Tokyo.

Rabbitt R, Ayliffe H, Christensen D, Pamarthy K, Durney C, Clifford S & Brownell W. (2005). Evidence of piezoelectric resonance in isolated outer hair cells. *Biophysical Journal* **88,** 2257-2265.

Rahman A, Lo C-M & Bhansali S. (2006). A micro-electrode array biosensor for impedance spectroscopy of human umbilical vein endothelial cells. *Sensors and Actuators B* **118,** 115-120.

Rahman A, Register J, Vuppala G & Bhansali S. (2008). Cell culture monitoring by impedance mapping using a multielectrode scanning impedance spectroscopy system (CellMap). *Physiol Meas* **29,** S227-S239.

Ratanachoo K, Gascoyne P & Ruchirawat M. (2002). Detection of cellular responses to toxicants by dielectrophoresis. *Biochimica et Biophysica Acta* **1564,** 449-458.

Robinson KR. (1979). Electrical currents through full-grown and maturing *Xenopus Oocytes*. *PNAS* **76,** 837-841.

Santos-Sacchi J. (1991). Reversible inhibition of voltage-dependent outer hair cell motility and capacitance. *J Neurosci* **11,** 3096-3110.

Schwan HP. (1968). Electrode polarization impedance and measurements in biological materials. *Ann N Y Acad Sci* **148,** 191-209.

Schwartz A, Sugg H, Ritter T & Fernandez-Repollet E. (1983). Direct determination of cell diameter, surface area, and volume with an electronic volume sensing flow cytometer. *Cytometry* **3,** 456-458.

Shan X, Patel U, Wang S, Iglesias R & Tao N. Imaging local electrochemical current via surface plasmon resonance. *Science* **327,** 1363-1366.

Sigg D & Bezanilla F. (1997). Total charge movement per channel: the relation between gating charge displacement and the voltage sensitivity of activation. *J Gen Physiol* **109,** 27-39.

Sigg D, Bezanilla F & Stefani E. (2003a). Fast gating in the Shaker K+ channel and the energy landscape of activation. *PNAS* **100,** 7611-7615.

Sigg D, Bezanilla F & Stefani E. (2003b). Fast gating in the Shaker K+ channel and the energy landscape of activation. *Proc Natl Acad Sci U S A* **100,** 7611-7615.

Sigg D, Stefani E & Bezanilla F. (1994). Gating current noise produced by elementry transitions in Shaker potassium channels. *Science* **264,** 578-582.

Simpson R, Berberian J & Schwan H. (1980). Nonlinear AC and DC polarization of platinum electrodes. *IEEE Transactions on Biomedical Engineering* **27,** 166-171.

Singer SJ & Nicolson GL. (1972). The fluid mosaic model of the structure of cell membranes. *Science* **175,** 720-731.

Sohn LL, Saleh OA, Facer GR, Beavis AJ, Allan RS & Notterman DA. (2000a). Capacitance cytometry: measuring biological cells one by one. *Proc Natl Acad Sci U S A* **97,** 10687-10690.

Sohn LL, Saleh OA, Facer GR, Beavis AJ, Allan RS & Notterman DA. (2000b). Capicatance cytometry: Measuring biological cells one by one. *PNAS* **97,** 10687-10690.

Stefani E & Bezanilla F. (1998). Cut-open oocyte voltage-clamp technique. *Methods Enzymol* **293,** 300-318.

Stuhmer W. (1992). Electrophysiological recording from Xenopus oocytes. *Methods Enzymol* **207,** 319-339.

Stuhmer W. (1998). Methods in Enzymology. pp. 281-300. Academic Press.

Swanson R & Folander K. (1992). In vitro synthesis of RNA for expression of ion channels in Xenopus oocytes. *Methods Enzymol* **207,** 310-319.

Tombola F, Pathak M & Isacoff E. (2005). Minireview: How far will you go to sense voltage? *Neuron* **48,** 719-725.

Treo E, Felice C, Tirado M, Valentinuzzi M & Cervantes D. (2004). Hematocrit measurement by dielectric spectroscopy. *IEEE Transactions on Biomedical Engineering*, 1-3.

Wang X, Becker F & Gascoyne P. (2002). Membrane dielectric changes indicate induced apoptosis in HL-60 cells more sensitively than surface phophatidylserine expression or DNA fragmentation. *Biochimica et Biophysica Acta* **1564,** 412-420.

Weber W. (1999). Endogenous ion channels in oocytes of *Xenopus laevis*: Recent Developments. *J Membrane Biol* **170,** 1-12.

Webster J. (1990a). *Electrical Impedance Imaging* Taylor and Francis, Bristol and New York.

Webster JG. (1990b). *Electrical Impedance Tomography*. Adam Hilger, Bristol.

Weiss T. (1996). *Cellular Biophysics*. The MIT Press, Cambridge, Massachusetts London, England.

Werdich A, Lima E, Ivanov B, Ges I, Anderson M, Wikswo J & Baudenbacher F. (2004). A microfluidic device to confine a single cardiac myocyte in a sub-nanoliter volume on planar microelectrodes for extracellular potential recordings. *Lab on a Chip* **4,** 357-362.

Wightman R. (2006). Probing cellular chemistry in biological systems with microelectrodes. *Science* **311,** 1570-1574.

Yu W, So PT, French T & Gratton E. (1996). Fluorescence generalized polarization of cell membranes: a two-photon scanning microscopy approach. *Biophys J* **70,** 626-636.